Technical University of Vienna

Doctoral Thesis

Applied infrared spectroscopy by nanomechanical resonators

Author:
Niklas Luhmann, M.Sc.

Supervisor:
Univ.-Prof. Dr. Silvan Schmid

Co-Supervisor:
Robert G. West, Ph.D.

A thesis submitted in fulfillment of the requirements for the

Doctoral's Degree in Natural Science

in the

Faculty of Electrical Engineering and Information Technology

March, 2024

"If you want to find the secrets of the universe, think in terms of energy, frequency and vibration."

Nikola Tesla

Abstract

Modern analytical demands for expedient characterization and identification of nanomaterials, ranging from environmental contaminants to developing nanopharmaceutical drugs, call for innovative techniques. While state-of-the-art methods like mass spectrometry provide high sensitivity in the picogram range, they require intensive sample preparation, concentration, and separation of low-abundance analytes. These drawbacks make the analyte susceptible to cross-contamination and sample loss.

A commonly used alternative for characterizing chemical composition based on functional groups is infrared (IR) spectroscopy. However, the low energy of IR photons limits the sensitivity of conventional transmission spectroscopy to the lower milligram range. Recent advancements, such as photothermal induced resonance (PTIR), which combines atomic force microscopy and photothermal expansion, have enabled the analysis of single nanoparticles down to the classification of 10^3 molecules. Nevertheless, these sophisticated methods are time-consuming and lack high throughput capabilities.
A promising technique for low abundant sample analysis introduced over the past decade is nanomechanical IR spectroscopy (NAM-IR), which exploits thermal-induced frequency detuning of nanomechanical resonators in response to absorbed infrared light. Due to photothermal enhancement over conventional transmission spectroscopy, this technique has demonstrated exceptional sensitivity comparable to the level of mass spectrometry. Despite the potential of NAM-IR spectroscopy to analyze various compounds such as femtograms of explosives, nanoparticles, pharmaceuticals, and thin films down to a few nanometers, its application to complex samples remains challenging. Moreover, its practical implementation as a widely applicable analytical tool has remained unrealized.

This thesis presents the scientific journey and development of a setup for applied NAM-IR spectroscopy from a proof-of-concept stage to an advanced state-of-the-art system. The novel system facilitates fast spectral acquisition featuring thermal desorption capabilities. For the first time, the technique of NAM-IR spectroscopy was combined with thermogravimetric analysis, demonstrating sensitivities as low as 5 pg (~30 fmol for caffeine) for single compounds and mixtures. The thermal control of the resonator and analyte further enables the acquisition of desorption kinetics and *in situ* separation of mixed compounds. This suggests the potential of the developed techniques for applications across various scientific domains.

The sensitivity of NAM-IR spectroscopy was evaluated across various resonator geometries, analytes, and sampling methods, including impaction-based sampling of generated and environmental aerosols, drop-casted proteins, and spin-coated thin films. In addition to operation with a quantum cascade laser, the NAM-IR system was successfully integrated with Fourier-transform spectroscopy. This has significantly enlarged the accessible spectral range from the so-called fingerprint region to the entire MIR range.

Zusammenfassung

Die analytischen Herausforderungen bei der Identifizierung von Nanomaterialien, von Umweltschadstoffen bis hin zur Entwicklung von Nanoarzneimitteln, erfordern innovative Techniken. Während modernste Methoden wie Massenspektrometrie eine hohe Empfindlichkeit im Pikogramm-Bereich bieten, erfordern sie häufig eine intensive Probenvorbereitung, Konzentration und Trennung von Analyten. Dies macht die Analyte anfällig für Kontamination oder Probenverlust.

Eine häufig verwendete Alternative für die Charakterisierung der chemischen Zusammensetzung anhand ihrer funktionalen Gruppen ist die Infrarotspektroskopie. Aber die im Verhältnis zum sichtbaren Spektrum geringe Energie der Infrarotphotonen limitiert die Empfindlichkeit konventioneller Transmissionsspektroskopie auf den unteren Milligrambereich. Neueste Entwicklungen wie die photothermisch - induzierte Resonanz (PTIR), welche die photothermische Ausdehnung einer Substanz mit der Rasterkraftmikroskopie kombiniert, ermöglicht die Analyse einzelner Nanopartikel bis hin zur Klassifizierung von nur 10^3 Molekülen. Jedoch ist diese Methode zeitaufwendig und ermöglicht daher keinen hohen Durchsatz.

Eine vielversprechende Technik für die Analyse von kleinen Mengen, die in den letzten Jahren eingeführt wurde, ist nanomechanische Infrarotspektroskopie (NAM-IR). Diese Methode basiert auf der photothermisch induzierten Frequenzverschiebung von nanomechanischen Resonatoren durch absorbiertes Infrarotlicht. Aufgrund der direkten Messung der Absorption durch photothermische Ausdehnung gegenüber der konventionellen Transmissionsspektroskopie, hat diese Technik eine außergewöhnliche Empfindlichkeit, welche mit der Massenspektrometrie vergleichbar ist. Doch trotz des großen Potenzials der NAM-IR Spektroskopie zur Analyse verschiedener Stoffe wie beispielsweise wenige Femtogramm von Sprengstoffen, Nanopartikel, Arzneimitteln und Nanometer dünne Schichten, bleibt ihre Anwendung auf komplexe Proben eine Herausforderung. Und ihre praktische Umsetzung als weit verbreitetes analytisches Werkzeug wurde bisher nicht realisiert.

Diese Arbeit präsentiert die wissenschaftlichen Grundlagen und die Entwicklung eines Systems für angewandte NAM-IR-Spektroskopie vom 'proof-of-concept' - Stadium bis zum hoch entwickelten 'state-of-the-art' - System. Dies ermöglicht eine schnelle Erfassung des Spektrums durch thermische Desorption. Zum ersten mal wurde NAM-IR-Spektroskopie mit thermogravimetrischen Analyse kombiniert und damiteine Detektionsgrenze von nur 5 pg Koffein (~30 fmol) für einzelne und gemischte Analyte erreicht. Die Implementierung einer Temperatursteuerung des Resonators ermöglicht zudem die zusätzliche Analyse der Desorptionskinetik und *in situ* Separation gemischter Analyte. Dies zeigt das Potential für Einsatzmöglichkeiten in vaerschiedensten Forschungsbereichen.

Die Empfindlichkeit der NAM-IR Spektroskopie wurde für verschiedene Resonatorgeometrien, Analyten und Samplingmethoden evaluiert unter anderem für künstlich erzeugte Aerosole, Ultrafeinstaub, Proteine und dünne Polymerschichten. Neben dem Betrieb mit einem Quantenkaskadenlaser wurde das NAM-IR system erfolgreich mit einem Fourier-Transform Infrarotspektrometer kombiniert, was den spektralen Bereich von der sogenannten "Fingerprint Region" auf das gesamte MIR Spektrum erweitert hat.

Contribution to original knowledge

During this PhD project, the technique of nanomechanical-based infrared spectroscopy was fundamentally studied and improved. Thereby, several significant contributions to the field were made:

Tailored resonator design. Previous studies on nanomechanical-based IR spectroscopy were conducted on string resonators and fully perforated membranes. This work conceptually changed the resonator design with the aim of enhancing thermal responsivity and sampling efficiency. This was done by testing different pore sizes and limiting the perforated area to concentrate the analyte in the center. In addition, perforated trampolines of different central areas were tested. The addition of a round clamping design to the suspension of perforated trampolines significantly increased the fabrication yield.

Development of absorber suited for NEMS-IR spectroscopy. When deploying the NEMS resonator as a light detector, as in classical IR spectroscopy, a suited or tailored absorber, acting as the light-to-heat transducer, is needed. In commercial detectors, this is commonly done by matching the sheet resistance of a thin metallic layer to half the free space impedance, thereby providing an independent absorptivity of 50 %. However, such films typically require a thickness of several tens of nanometers, which have a significant thermal mass, especially when compared to the implementation on 50 nm thin resonators. In the course of this project an ultrathin 2 nm impedance-matched absorber with a persistently stable absorptivity of 47(3) % was developed and successfully tested on NEMS resonators.

Combining NEMS-IR spectroscopy with thermal desorption and *in situ* separation. Similar to other detection methods, the analysis of complex samples remains challenging with NEMS-IR spectroscopy. In classical spectroscopy, a complex sample is separated before analysis using established techniques such as liquid or gas chromatography; otherwise, a deconvolution of the mixed spectral result must be performed. With the implementation of a thermo-electric element in direct contact with the nanomechanical resonator, complex mixtures can now be separated *in situ* by thermal desorption, exploiting the distinct vapor pressures of the individual compounds. When operating below room temperature, the system further allows the analysis of condensates such as residual hydrocarbons. This novel technique of NEMS-IR-TD allows the simultaneous monitoring of the desorption & adsorption processes and corresponding spectral response. The resulting spectro-temporal maps enable a selective identification

of the compounds in a mixture with simple mathematical deconvolution. Furthermore, the thermo-gravimetric data allow for the analysis of desorption dynamics of individual compounds and in mixture. With this feature, NEMS-IR-based spectroscopy moved from a proof-of-concept to a versatile analytical tool.

Coupling of NEMS-IR to an incoherent broad spectral light source. One of the major drawbacks in the prior state-of-the-art NEMS IR spectroscopy is the accessible spectral range limited by the implemented IR laser. Other studies showed that incoherent light can be coupled to a nanomechanical system such as, e.g., a cantilever. In this configuration, the modulated change of static deflection of the cantilever can be Fourier-transformed into an IR spectrum. This project successfully merged the developed NEMS-IR system with a commercial Fourier transform IR spectrometer. Compared to the static deflection of a cantilever, the spectrum results from a Fourier transformation applied to the recorded frequency detuning of the nanomechanical resonator. Thereby, the sensitivity and the spectral range were significantly increased from the fingerprint region 1779 cm^{-1} to 1122 cm^{-1} to the full range of a classical FTIR spectrometer 6000 cm^{-1} to 500 cm^{-1}. The combined setup enabled the detection of a few nanograms of polyvinylalcohol. Upon the commercialization of this technique, the latest NEMS-FTIR prototype enabled a limit of detection for theobromine of 130 pg. Due to the working principle of this technique, independent of the wavelength, one can expect an equally high performance in the far-IR (terahertz) range.

Analysis of ultrafine airborne particles by NEMS-FTIR spectroscopy. Due to their low mass, the chemical identification of ultrafine airborne particles with a diameter below 500 nm remains an analytical challenge. As a result, it is common practice to accumulate particles over several hours up to days on filters to accumulate sufficient material for state-of-the-art techniques such as mass spectrometry. Moreover, the sample preparation from a filter to the device often causes contamination and sample loss. In the course of a supervised bachelor thesis during this project, a mobile sampler for the collection/impaction of ultrafine particles on the perforated membrane resonators was developed. Thereby, particles collected for only 15 min resulted in well-defined NEMS-FTIR spectra with a high signal-to-noise ratio of functional organic groups comparable to the literature. In addition to the benefit of no sample transfer or preparation, this technique allows for time-resolved identification of the environmental airborne particles.

List of publications

[1] M. Piller, **N. Luhmann**, M.H. Chien, S. Schmid, "Nanoelectromechanical infrared detector", Optical Sensing, Imaging, and Photon Counting: From X-Rays to THz 2019 11088 (2019)

[2] **N. Luhmann**, D. Høj, M. Piller, H. Kähler, M.H. Chien, R.G. West, UL Andersen, S. Schmid, "Ultrathin 2 nm gold as impedance matched absorber for infrared light", Nature Communications 11 (1), 2161 (2019)

[3] M. Piller, P. Sadeghi, R.G. West, **N. Luhmann**, P. Martini, O. Hansen, S.Schmid, "Thermal radiation dominated heat transfer in nanomechanical silicon nitride drum resonators", Applied Physics Letters, 034101 (2020)

[4] P. Sadeghi, M Tanzer, **N. Luhmann**, M Piller, MH Chien, S Schmid, "Thermal transport and frequency response of localized modes on low-stress nanomechanical silicon nitride drums featuring a phononic-band-gap structure", Physical Review Applied 14 (2), 024068 (2020)

[5] M.G. Bartmann, M. Sistani, **N. Luhmann**, S. Schmid, E. Bertagnolli, A. Lugstein, J. Smoliner, "Germanium nanowire microbolometer", Nanotechnology 33 (24), 245201 (2022)

[6] M. Piller, J. Hiesberger, E. Wistrela, P. Martini, **N. Luhmann**, S. Schmid, "Thermal IR detection with nanoelectromechanical silicon nitride trampoline resonators", IEEE Sensors Journal 23(2), 1066-1071 (2023)

[7] **N. Luhmann**, R.G. West, J.P. Lafleur, S. Schmid, "Nanoelectromechanical infrared spectroscopy with *in situ* separation by thermal desorption: NEMS-IR-TD", ACS Sensors 8, 4, 1462–1470 (2023)

[8] H. Besic, A. Demir, J. Steurer, **N. Luhmann**, S. Schmid, "Schemes for tracking resonance frequency for micro-and nanomechanical resonators", Phys. Rev. Applied 20, 024023 (2023)

Acknowledgements

Looking back on five years of pursuing this doctoral thesis, it was a quest. A journey that I certainly could not have mastered by myself but through the endless support and challenges of my mentors, colleagues, family, and friends. It feels impossible to mention and thank every individual who contributed to my success, but I will try my very best.

First and foremost, I want to start with Professor **Silvan Schmid** and **Josiane Lafleur**. You are my biggest source of scientific inspiration and certainly the toughest opponents in discussing ideas I could have possibly imagined. I am deeply grateful to have chosen you as my mentor who continuously challenged but also supported me at any time to succeed - whether in theory, the laboratory, the application for funding, or even in private matters. During my first contact with Silvan on the proactive search for a master's thesis in nanomechanical sensors, I immediately realized that this was exactly the mentor and research I was looking for. Not surprisingly, I decided to continue and do my PhD and join you both on the greater journey with Invisible-Light Labs. It gave me the opportunity, even as a master's student, to help build up a laboratory and now be part of an endeavor to make this technology available to everyone. Thank you so much for everything!

In the same way, I want to express my warmest gratitude to **Robert West**. You are truly a fantastic post-doc and supervisor with a relentless drive to provide support at any time. At many stages of my career, this made a huge difference, and your always sunny mood is a blessing for me and the entire group. Thank you so much for that!

Moving on with my colleagues at the MNS group, there are many people to thank for. Among them, I want to start with **Paolo Martini**, who really became a very close friend and roommate. Research can be frustrating sometimes, but with your lovely personality and good music in the lab (and amazing pasta at home!), it was always fun! I wish you the best to succeed in your own projects at work and in private! The same way I want to thank **Kostas Kanellopulos** and **Hajrudin Besic**, our theory and electronics master minds of the group. Your passion and expertise helped me a lot to stay on track and bounce of some ideas and end up with fruitful discussions.

Looking back to the early stages of my PhD, I would like to thank a bunch of colleagues that supported me on many levels. Among them in particular **Markus Piller**, **Pedram Sadeghi**, **Johannes Hiesberger**. It was fantastic to work with all of you, and the shared publication list underlines our outstanding team work during these years! The same way I want to thank **Hendrik Kähler**, who besides being my longest office mate became a good friend. Despite the divergence of our research topics we had amazing discussion

ranging from experimental designs up to inconclusive data. I barely know anyone so precise and would not miss a single detail. Great that we can finish our PhD journey back to back!

What would this work be without the amazing support by the incredible team of *Invisible-Light Labs*! I often can't believe what you have achieved over the course of the past two years. And without the deep support by **Tatjana Penn**, **Veljko Vukićević** and **Jelena Timarac Popović**, I would not have accomplished those amazing results.

Moving on to the MST group, I want to highlight **Jonas Hafner & Georg Pfusterschmid**. It was always a pleasure to discuss any topic while having a good cup of coffee or beer. I would also thank Professor **Ulrich Schmid** for his support and the ongoing challenge to be the head of our institute. Further, my thanks go out to our technicians' team, in particular, **Johannes Schalko**, **Michael Buchholz**, **Patrick Meyer**, who supported me in the clean room.
Finishing a Ph.D. at the Institute of Sensor and Actuator Systems would not be possible without an amazing administration team. I wouldn't know what this institute would do without **Martina Nuhsbaumer**, **Martina Bittner** & **Andreas Astleitner**. You are literally the foundation of ISAS and always there to support us by finding individual solutions through the administrational maze of TU Wien and Austria. Thank you so much!

Aside from university, there are a lot of people who have shaped my life and have been a great support. It is impossible to quote everyone personally, so I start by expressing my deepest gratitude to everyone who lived or still lives in my house community 'Chilla Bunterhund'. May it be cheering up after a hard day or providing culinary masterpieces when coming home after a long day in the lab. You all contributed to my personal growth, and I could not have managed to get this done without you!

I want to dedicate this last round of acknowledgments to my family and friends. Foremost to my parents **Heike & Ralf Luhmann**, my sister **Isabelle Luhmann**, brother-in-law **Sven Sobotta**, and aunt & uncle **Inge & Hans Stahlberg** for their endless supported in every aspect of my life. You always believed in my abilities and gave me the trust to reach my personal goals. It is essence you that made me sit here and finalize the last words of a doctoral thesis. I can't express enough how proud I am to have you as my family.

Likewise, I'd like to thank my best friend **Claudio Michaelis**, who gave me guidance and support in every aspect starting from the first semester in Konstanz till today; and also **Katharina Schauer** for your strong support throughout the time of this thesis.

It would not feel complete without mentioning **Mario Mosbacher** & **Ulrich Wachter** who mentored me during the scientific competitions at 'Jugend Forscht'. You awoke my passion for nature science and paved the foundation of my career.

At last, I would like to thank the **Austrian Academy of Science** for the immense financial support by the DOC scholarship that, after all, enabled me to do this work!

Abbreviations

NEP	Noise-equivalent power
IR	Infrared
FTIR	Fourier-transform infrared spectroscopy
QCL	Quantum cascade laser
NAM-IR	Nanomechanical based infrared spectroscopy
NEMS-IR	Nano-electromechanical sensor for infrared spectroscopy
NEMS-IR-TD	NEMS for combined infrared and thermal desorption spectroscopy
MIR	Mid infrared
FIR	Far infrared
THz	Terahertz
PSD	Power spectral density
SNR	Signal-to-noise ratio

Contents

1 Introduction

The prediction of infrared light (IR) by Emilie du Chatelet in 1737 and proof of its existence by William Herschel in 1800 laid the foundation for the deployment of light far beyond the visible spectrum. The development of a prism-based spectroscope and the following implementation of gratings in the early 20th century facilitated the detailed study of the infrared spectrum and utilization for the spectroscopy of materials. Infrared spectroscopy, which is the analysis of infrared radiation being absorbed or transmitted from a compound, became a valuable and non-destructive analytical tool. The invention of the Fourier transform infrared spectroscopy (FTIR) in 1949 by Peter Fellgett [9] and computational breakthrough by Cooley & Tukey in 1965 [10] revolutionized the field by allowing for more precise and significantly faster measurements. Nowadays, FTIR spectroscopy is widely used in various applications, such as analytical chemistry, physics, biochemistry, and material science. However, due to the low energy of IR photons compared to the ultraviolet and visible spectrum, analysis by FTIR spectroscopy has a lower sensitivity. This drawback is accompanied by complex sample preparation (e.g. need for purification or up-concentration), strong interference with the absorption band of water, limited structural information and, depending on the complexity of the sample, the need of intensive data analysis. The introduction of internal reflection-based FTIR spectroscopy in 1960 [11], commonly referred to as attenuated total reflectance (ATR), paved the way for the fast and convenient IR analysis of chemical compounds and has become today's standard technique.

More recent approaches to spectroscopy exploit photothermal effects of the substance, for instance, by probing the photothermal expansion of the analyte by atomic force microscopy (AFM-IR / PTIR) [12] or the change of refractive index by a probing beam [13]. This enabled spectral analysis combined with a lateral resolution below the diffraction limit, for instance, of self-assembled monolayers with 25 nm resolution [14]. Recently, the analysis by advanced AFM-IR spectroscopy of single nanoparticles demonstrated detection limits in the zeptomole range [15]. However, despite these exceptional sensitivities, imaging-based techniques are limited to the scanning area and are not made for fast chemical analysis.

One of the most proliferated techniques for the chemical composition analysis is mass spectrometry (MS). This method relies on the ionisation and fragmentation of the analyte and subsequent measurement of the mass-to-charge ratio. For the application of complex samples, typically MS is combined with a separation step upstream. Therefore, so-called *hyphenated* techniques, such as gas (GC) or liquid chromatography (LC) coupled to a mass spectrometer (MS), became the analytical standard to provide a

separation of complex mixtures, detection with high sensitivity, and structural information. A challenge for LC/GC-MS are samples that exhibit non-specific fragmentation patterns or have similar isomers and, therefore, can poorly be identified [16]. A solution is the hyphenation of GC/LC with the known Fourier-transform infrared spectroscopy (FTIR), which, in contrast, can identify isomers. This has led to numerous developments, dating back to 1967 [17, 18], by interfacing IR transparent gas-cells (light pipes) with GC or LC [19] reaching low nanogram sensitivity using cryogenically cooled MCT detectors [20, 21, 22, 23]. Compared to MS, light pipe-based GC/LC-FTIR suffers from a significantly reduced sensitivity. Therefore, more advanced methods such as cryogenic trapping (matrix isolation) [24] or direct-deposition [25] GC-FTIR have been developed to capture and concentrate the analyte. This allows for long spectra acquisition times, which increases the signal-to-noise ratio, pushing the detection limit to the sub-nanogram range [26, 27]. However, such techniques are complex and do not enable the real-time collection of IR spectra.

An alternative approach for separating and identifying complex mixtures is combining temperature programmed desorption (TPD) or thermogravimetry (TG) with FTIR or MS. TPD has become a valuable tool to study the physiochemical properties of chemical compounds, decomposition- and catalytic processes [28, 29]. Whereby, the mixed compound is continuously heated and desorbed into a gas phase, which subsequently can be analyzed by FTIR spectroscopy with a flow cell via a heated transfer line or interfaced with MS [30, 31, 32, 29]. However, compared to the aforementioned trapping methods, such TPD-FTIR systems demonstrated sensitivities only in the microgram range [33]. Despite this drawback, highly hyphenated systems such as TPD-FTIR-GC-MS are on the rise, enabling the challenging analyses of complex environmental samples like microplastics in marine organisms [34]. As one can readily conclude, such systems are highly complex and expensive and do not allow fast or on-field analysis. However, the rising environmental threats call for innovative analytical methods to rapidly identify and quantify contaminants for rapid action and remediation.

Over the past decades, the development of nanoelectromechanical systems (NEMS) has shown an immense potential to provide solutions for a wide range of applications [35, 36, 37]. Typically, such sensor systems inherit a nano-scaled structure, such as a beam or string, which responds by a change in static deflection or resonance frequency. Tailored to diverse geometries and applications, NEMS offers unparalleled sensitivity for detecting parameters like mass [38, 39, 40, 41], temperature/heat [42], and magnetic or electrical fields [43] down to single-molecule or picotesla levels. This positions them as optimal candidates to tackle the limitations and shortcomings of current analytical methods. In recent years, this has led to novel sensor techniques for detecting infrared

light [44, 45, 46]. The principle of such techniques is a thermally-induced frequency detuning of a nanomechanical resonator due to absorbed light. When used as a light detector, as in classical IR spectroscopy, a tailored absorber on the surface of the resonator acts as a light-to-heat transducer. The concept of detecting light by thermal expansion of a material ranges back to 1969 with macroscopic elements such as a tensioned aluminum foil [47]. With the development of micromechanical systems, photothermal detectors, such as those based on static deflection of bi-material cantilevers, significantly pushed IR detection sensitivity to a few tens of picowatts [42, 48, 49].

In addition to detecting IR light by the absorbed heat, a cantilever can be utilized as a highly sensitive platform for detecting the absorbed heat of a chemical compound. In this approach, the chemical compound is in physical contact with the cantilever, acting as the primary absorbing substance. Thus, only the molecular-specific vibrational modes lead to a photothermal softening and, thus, the bending of the cantilever. With this approach, the spectral detection of e.g. dimethyl-methylphosphonate adsorbed on a microcantilever down to 25 ng could be achieved [50]. More recently, the development of nanomechanical systems and powerful IR light sources pushed the detection by this so-called *nanomechanical IR spectroscopy* (NAM-IR) to the picogram range [51]. However, due to the slow detection frequency, such techniques working on the principle of photothermal softening are affected by electronic 1/f noise [48].

In contrast to the photothermal softening observed in a cantilever, one can utilize the resonance frequency change resulting from the expansion of a tensile-stressed element, such as a string or membrane. Unlike the deflection-based approach, where temperature responsivity scales solely with the softening of Young's modulus ($\mathscr{R}_T \propto \alpha_E$), the responsivity of tensile-stressed resonators benefits from an enhancement scaling inversely with stress ($\mathscr{R}_T \propto \alpha_{th} E/\sigma_0$), where α_{th} is the coefficient of thermal expansion, E is Young's modulus, and σ_0 is tensile stress). Moreover, this dynamic technique enables operation at higher frequencies, reducing $1/f$ noise and tuning responsivity by reducing tensile stress [52]. Transitioning from a static-deflection-based approach to dynamical detection via frequency change has significantly increased sensitivity by an order of magnitude [53, 54]. In fact, implementing a tailored nanomechanical geometry and absorber has enhanced sensitivity for IR light detection to 7 pW/Hz$^{1/2}$ [6].

Likewise, the change from static to dynamical-based NAM-IR spectroscopy has demonstrated exceptional sensitivities for the analysis of a variety of compounds such as polymer nanoparticles [55], micelles [56], explosives [53], pharmaceuticals [57, 58], and polymer thin films [59] with detection limits down to the femtogram range.

Recent studies probing with visible light on stress-optimized resonators demonstrated a sensitivity on the single-molecular level [60]. However, throughout all studies, this technique has only been demonstrated as a proof of concept. Similar to the drawbacks of the aforementioned FTIR techniques, the analysis of complex samples with NAM-IR remains a challenge without the capability of separating absorption spectra of mixtures. Further, tunable IR light sources such as quantum cascade lasers are typically limited to a narrow spectral range.

The presented work aims to advance NAM-IR spectroscopy from a proof-of-concept to a widely applicable analytical technique. The focus is set on facilitating the transduction, improving the sensitivity, enlarging the spectral range and exploring different sampling methods. These objectives were addressed by designing a novel setup, testing a variety of resonator geometries to optimize the sensitivity and sampling efficiency, and combining NAM-IR with FTIR spectroscopy. Additionally, incorporating thermal control of the resonator enhances sensitivity by minimizing thermal drifts and fractional frequency noise [1]. Moreover, thermal control enables the combination of NAM-IR spectroscopy with thermogravimetric analyses of the deposited analytes. This allows the study of desorption kinetics, *in situ* separation, and spectroscopy with the same device.

1.1 Thesis outline

The presented work shows the fabrication and analysis of an absorber, tailored for NAM-IR light detection and the development of a versatile analytical tool with *in situ* sample separation reaching single picogram sensitivity. After a brief introduction, the second chapter introduces the general technique and limitations of nanomechanical-based IR spectroscopy.
The main objective of this chapter is to provide a concise theoretical overview of the nanomechanical response to power and limitations concerning their application in infrared spectroscopy. This chapter further describes the impact of the transduction scheme on the sensitivity and comprises a selection of possible sampling methods and their efficiencies.
The third chapter gives a condensed overview of the general fabrication steps of the resonators used throughout the thesis. Further, the methods for resonance frequency tracking and the general technique of Fourier transform infrared spectroscopy are introduced.

The fourth chapter focuses on potential absorption techniques for infrared light and developing an absorber suitable for a nanomechanical resonator as an infrared detector. This chapter also presents the fabrication and performance of ultrathin metal films as impedance absorbers.
The fifth chapter displays the development steps and scientific pathway of the NEMS-IR setup from a proof-of-concept to a state-of-the-art tool. As part of this development, the chapter covers the design optimization of the resonator, the implementation of an aerosol sampling setup for liquid analytes, and the coupling of the system to an incoherent light source.
Following the development of the final setup, chapter six presents the application of the system to single compounds and mixtures with a demonstration of desorption and *in situ* separation. In addition to the analysis of the detection limit, the application for thermo-gravimetric analysis, such as thermal desorption spectroscopy, is demonstrated.
In the subsequent chapter, the advanced NEMS-IR spectroscopy setup is tested for different applications, such as ultrafine airborne particles, and different sampling methods, such as spin-coated polymer thin films or drop-casted proteins. Further, the chapter highlights the impact of the light source modulation on the response when used in conjunction with an FTIR and the evaluation of the detection limit.
In the last chapter, this thesis's findings are summarized as guidelines for applying NAM-IR spectroscopy. These comprise several aspects of tailoring the resonator design and the choice of tensile stress, absorber, and sampling method. Finally, the developed setup is compared to state-of-the-art photothermal spectroscopy.

2 Principles and considerations for nanomechanical based IR spectroscopy

This chapter introduces a simplified approach to theoretically describe the fundamental principles of nanomechanical-based IR spectroscopy and discuss the general limitations. The theory presented comprises assumptions and conclusions based on the recent work of R. West and S. Schmid et al. [61, 62]. From this point, we further distinguish between 'indirect' and 'direct' spectroscopy, as schematically depicted in Figure 2.1. In the direct case, the nanomechanical resonator is utilized as a sensitive platform for the heat from absorbed light by a substance deposited on the resonator; for indirect spectroscopy, the resonator is used as an IR light detector, similar to classical transmission spectroscopy. Independent of the approach, both techniques are based on the resonator's photothermal induced expansion and resulting frequency change due to absorbed heat.

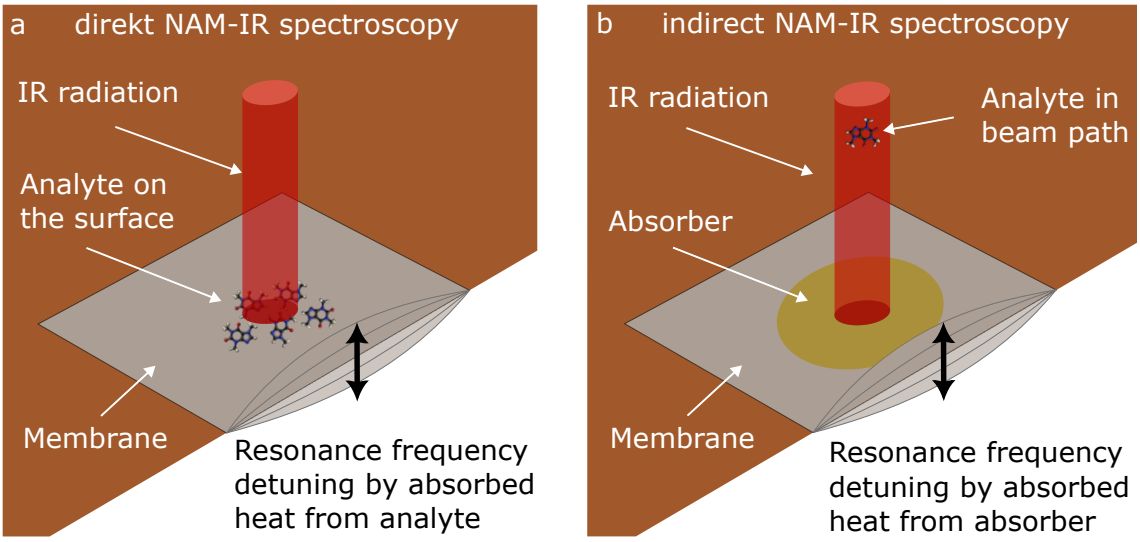

Fig. 2.1: Schematic model of a nanomechanical membrane used for (a) direct and (b) indirect IR spectroscopy. Inspired by [1].

A common way to characterize and compare the performance of a light detector is the noise-equivalent power (NEP), expressed in the unit of $W/\sqrt{Hz}$. This figure of merit quantifies the lowest measurable power of a detector, independent of the bandwidth. For a mechanical detection scheme based on the change of a frequency, it is defined as the ratio of the power spectral density (PSD) of the fractional frequency noise $\sqrt{S_y(\omega)}$ and power responsivity $\mathscr{R}_p(\omega)$:

$$NEP = \frac{\sqrt{S_y(\omega)}}{\mathscr{R}_P(\omega)}. \tag{2.1}$$

2.1 Nanomechanical response to power

For a nanomechanical resonator, the power responsivity is based on the frequency response, which is defined by the fractional frequency shift $y = (f_{light} - f_{inital})/f_{inital}$ to an impinging power P_0 [62, 61]:

$$\mathscr{R}_{P_0} = \frac{\delta y}{\delta P_0}, \tag{2.2}$$

where $\mathscr{R}_{P_0} = \alpha_{abs}(\lambda)\mathscr{R}_P$ accounts for the wavelength-dependent absorptance $\alpha_{abs}(\lambda)$ of the resonators' material or analyte deposited. The fractional frequency response of the resonator depends on the intrinsic responsivity to a change in temperature $\mathscr{R}_T$ and thermal conductance G of the resonator. Thus, the power responsivity can be further defined as shown by Schmid et al. [62]:

$$\mathscr{R}_{P_0}(\omega) = \frac{\alpha_{abs}(\lambda)\mathscr{R}_T}{G} \underbrace{\frac{1}{\sqrt{1+\omega^2\tau_{th}^2}}}_{H_{th}(\omega)}, \tag{2.3}$$

Here, $H_{th}(\omega)$ accounts for the low-pass characteristic of the responsivity concerning a possible modulation (ω) of the incident light, limited by the thermal time constant τ_{th} of the resonator. Depending on the absorptance $\alpha_{abs}(\lambda)$, a fraction of the incident radiation is absorbed, leading to photothermal-induced expansion and softening of the material. For unstressed mechanical objects such as plates or beams, the temperature responsivity depends solely on the softening of Young's modulus E, with $\mathscr{R}_T = \alpha_E/2$, where α_E represents the softening coefficient.

In contrast, pre-stressed resonators, such as strings or the membrane depicted in Figure 2.1, exhibit temperature responsivity dominated by thermal expansion and resulting changes in tensile stress. Assuming a linear elastic material, the thermal expansion of a membrane can be expressed as a temperature-dependent linear change of the tensile stress by [62, p.191]:

$$\sigma(T) = \sigma_0 - \frac{E\alpha_{th}(T - T_0)}{1 - \nu}, \tag{2.4}$$

where σ_0 is the initial tensile stress of the membrane and α_{th} the coefficient of thermal expansion. Here, the Poisson's ratio ν further accounts for the bi-axial stress in a membrane. For a small temperature change and small change in tensile stress, respectively, one can insert the temperature-dependent stress to the eigenfrequency of a membrane $\omega_{n,m}(T) = (\pi\sqrt{n^2+m^2}/L)(\sqrt{\sigma(T)/\rho})$ and apply a first-order Taylor expan-

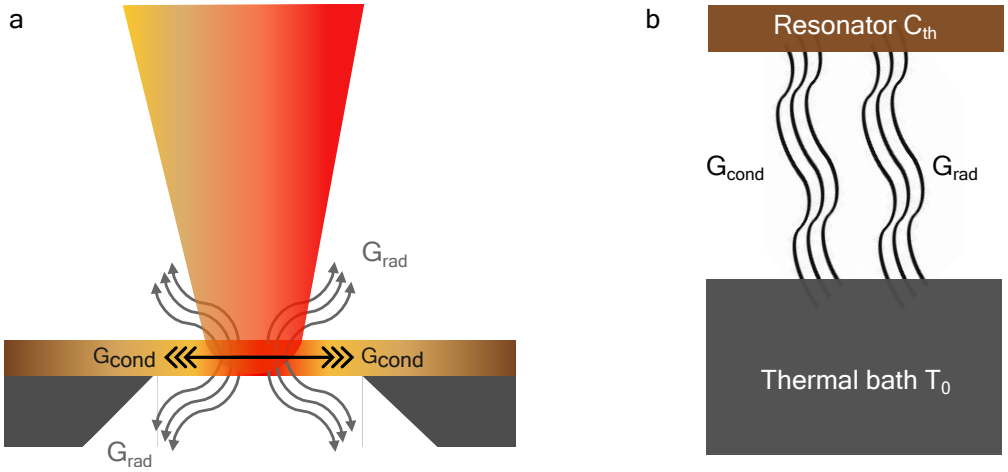

Fig. 2.2: (a) Cross-section of a membrane resonator illustrating the dissipation channels from locally absorbed heat and, (b) equivalent lumped element model of a membrane as the central thermal mass with heat capacity C_{th}, connected to an infinite thermal bath with room-temperature T_0 via the thermal conductance $G = G_{cond} + G_{rad}$ [62]. Inspired by [3]

sion [62, p.191]:

$$\omega_{n,m}(T) \approx \omega_{n,m}(T_0)\left(1 - \frac{1}{2}\frac{E\alpha_{th}(T - T_0)}{\sigma_0(1-\nu)}\right). \tag{2.5}$$

For simplification, we assume no contribution by the photothermal-induced change of the density or softening of Young's modulus ($\alpha_E \approx \alpha_{th}$). Compared to the temperature dependence of the tensile stress, those contributions only add a minor change to the resonance frequency and are therefore neglected [62]. Ultimately, the fractional frequency response of the membrane to a temperature change can be expressed by [62, p.192]:

$$\mathscr{R}_T = \frac{\delta\omega_{n,m}(T)}{\delta T}\frac{1}{\omega_{n,m}(T)} = -\frac{\alpha_{th}E}{2\sigma_0(1-\nu)}. \tag{2.6}$$

Notably, $\mathscr{R}_T$ scales linearly with E/σ_0 but remains independent of the resonator's size. As a result, the influence of the lateral dimension of the resonator on the power responsivity $\mathscr{R}_{P_0}(\omega)$ is solely manifested in the heat transfer of the absorbed heat, described by G. To streamline the theoretical estimation of thermalization, we simplify the scenario of a heated membrane using a lumped element model.

As depicted in Figure 2.2, the resonator can be conceptualized as a thermal mass with a heat capacity C_{th}, thermally connected to an infinite thermal bath at room temperature T_0. The thermal time constant can be readily determined as $\tau_{th} = C_{th}/G$, where G represents the thermal conductance. In a vacuum environment, heat conduction comprises two main contributions: heat conduction through the material of the resonator (G_{cond}) and heat transfer due to radiation from the resonator's surface (G_{rad}). The heat transfer

through the material is determined by the heat flux through the cross-sectional area of the membrane with the specific thermal conductivity κ_{th} [62, p.199]:

$$G_{cond} = 2\pi^2 h \kappa_{th} \,. \tag{2.7}$$

Assuming a small temperature increase, the heat transfer through radiation can be approximated by the resonators' surface L^2, surrounding temperature T_0, and the emissivity ε_{rad} of the resonator material [62, p.199]:

$$G_{rad} = 2 \cdot (4L^2 \varepsilon_{rad} \sigma_{SB} T_0^3), \tag{2.8}$$

where σ_{SB} is the Stefan-Boltzmann constant. The pre-factor of two accounts for the radiation from both sides of the resonator. Finally, the total heat transfer can be approximated by the sum of both heat transfer mechanisms as [1, 62]:

$$G \approx (G_{cond} + G_{rad}) \,. \tag{2.9}$$

To get a complete picture of the detection limit defined by the NEP (see Equation 2.1), one has to estimate the noise sources of the system. As the resonator's response to power is a change in frequency, we focus on the primary sources that limit the frequency resolution of the system, namely temperature fluctuations according to the fluctuation-dissipation theorem $S_{th}(\omega)$ and the contribution by thermomechanical noise $S_{thm}(\omega)$. Due to the temperature responsivity of the resonator, fluctuations in the resonator temperature from statistical emission and absorption of thermal photons translate to fluctuations in the resonator's frequency. Under the assumption of a lumped-element model of the membrane as depicted in Figure 2.2b, one can make a simplified first-order approximation of the noise by thermal fluctuations by the fluctuation-dissipation theorem given by [62, p.172], [63, 64]:

$$S_{th}(\omega) = \frac{4k_B T^2}{G} H_{th}^2(\omega), \tag{2.10}$$

where k_B is the Boltzmann's constant and T the resonators' temperature. To translate these fluctuations of temperature to fluctuations in frequency, one can apply S_{th} to the temperature responsivity of the resonator $\mathscr{R}_T(\omega)$. Then, one can derive the fractional frequency noise PSD due to temperature fluctuations by [62, p.172][63]:

$$S_{y,th}(\omega) = S_{th}(\omega)[\mathscr{R}_T]^2 = \frac{4k_B T^2}{G} \left[\frac{\alpha_{th} E}{2\sigma_0(1-\nu)}\right]^2 H_{th}^2(\omega). \tag{2.11}$$

This approximation resembles a crude estimation of the temperature fluctuation noise spectral density, assuming the resonator is a constant concentrated mass connected to a thermal reservoir by the heat transfer G. For a more accurate estimation, one has to derive an effective thermal response of the specific resonator geometry. However, based on recent FEM studies (Kanellopulos et al. manuscript in preparation), the approximated estimation of the noise in Equation 2.11 to the NEP is deemed acceptable.

The thermomechanical noise originates from the fluctuations in the phase due to thermally driven variations of the amplitude. Therefore, these fluctuations depend on the mechanical response of the resonator, which depends on the quality factor Q, the effective mass m_{eff}, the resonance frequency ω_0, and displacement amplitude z_r [62, p.164][65]:

$$S_{y,thm}(0) = \frac{2k_B T_0}{m_{eff} Q \omega_0^3 z_r^2}(1 + \mathscr{K}^2). \tag{2.12}$$

Here, $\mathscr{K}$ is a dimensionless coefficient to account for the ratio of noise introduced by the transduction scheme compared to the thermomechanical noise only [62, p.162]. For values of $\mathscr{K} > 1$, the frequency resolution is dominated and limited by the transduction (see Section 2.3). However, for the following discussion of the intrinsic theoretical detection limit, we further assume the system is not limited by the transduction scheme $\mathscr{K} \ll 1$.

The overall PSD of the noise is the sum of both fractional-frequency fluctuations $S_y(\omega) = S_{y,th}(\omega) + S_{y,thm}(\omega)$. For a simplified stationary case, where $\omega \ll 1/\tau_{th}$, the noise PSD reduces to a constant, frequency-independent white noise. Following these assumptions, one can relate the noise PSD to the so-called Allan variance $\sigma_y^2(\tau)$ with the signal integration time τ by [62, p.162]:

$$\sigma_y^2(\tau) = \frac{S_y}{2\tau} \quad \text{with } S_y = \text{constant, white.} \tag{2.13}$$

In practice, when considering additional contributions to the noise PSD introduced by the readout system, the empirical Allan deviation $\sigma_y(\tau)$ and corresponding integration time represent a precise metric for characterizing the frequency resolution of the resonator. Under the assumption of a stationary system and fractional frequency noise as described by the Allan deviation, the NEP can be expressed by [62, p.177]:

$$NEP = \frac{\sqrt{S_y(\omega)}}{\mathscr{R}_{P_0}(\omega)} = \frac{\sigma_y(\tau)\sqrt{2\tau}}{\mathscr{R}_{P_0}(\omega)}. \tag{2.14}$$

2.1.1 Theoretical limitations of the temperature response

The well-established fabrication processes for micro- and nanometer-sized structures and low thermal conductance make silicon nitride an ideal material for NAM-IR spectroscopy. Its minimal absorption across a broad spectral range, except a broad vibrational mode at 860 cm^{-1}, further augments its suitability. The following section discusses the limitations of the power responsivity and NEP using the example of a 50 nm-thin silicon nitride resonator with approximate material parameters listed in Table 2.1. Considering the increased power response for lower tensile stress ($\mathscr{R}_T \propto E/\sigma_0$ see Equation 2.6), the parameters for a silicon-rich silicon nitride (Si_xN_y) are used.

Tab. 2.1: List of approximate and estimated physical properties for a $h = 50$ nm thin silicon-rich Si_xN_y at room temperature (300 K).

Material parameter	Variable	Si_xN_y	Source
Tensile stress	σ_0	100 MPa	Estimate
Young's modulus	E	225 GPa	[66]
Thermal expansion coefficient	α_{th}	1.23×10^{-6} K^{-1}	[67]
Thermal conductivity	κ_{th}	3 $W\,m^{-1}\,K^{-1}$	[68]
Specific heat	C_{th}	800 $J\,kg^{-1}\,K^{-1}$	[68]
Mass density	ρ	3000 kg/m^3	[68]
Emissivity	ε_{rad}	0.05	[3]

For comparison, the power responsivity is estimated for different values of $\alpha_{abs}(\lambda)$ corresponding to the wavelength-dependent absorptivity of Si_xN_y , displayed in Figure 2.3a. The absorption was obtained from the average of five transmission and reflectance measurements of a 50 nm Si_xN_y membrane. The absorption feature at around 2565 cm^{-1} can be attributed to light intensity variations due to the asymmetric stretching mode of carbon dioxide (CO_2).

Figure 2.3b shows the theoretical power responsivity $\mathscr{R}_{P_0}(\omega = 0)$, from Equation 2.3, of a silicon nitride membrane with the material properties from Table 2.1 as a function of the lateral size L. To highlight the dependence of the absorptance, the power responsivity is plotted assuming complete light-to-heat conversion $\alpha_{abs}(\lambda) = 1$, and for different spectral ranges highlighted in Figure 2.3a, like the vibrational mode of Si_xN_y at $\lambda \approx 12\,\mu m/835\,cm^{-1}$ (orange) and in the 'Amide bands' ranging from approximately 1700 µm to 1200 µm (green). The grey-dashed lines indicate the responsivity when limited by conductive heat transfer only. As can be observed from Figure 2.3b, with increasing surface area, the heat transfer is dominated by radiative heat transfer. As a consequence, the responsivity remains constant up to a tipping point around a membrane size of

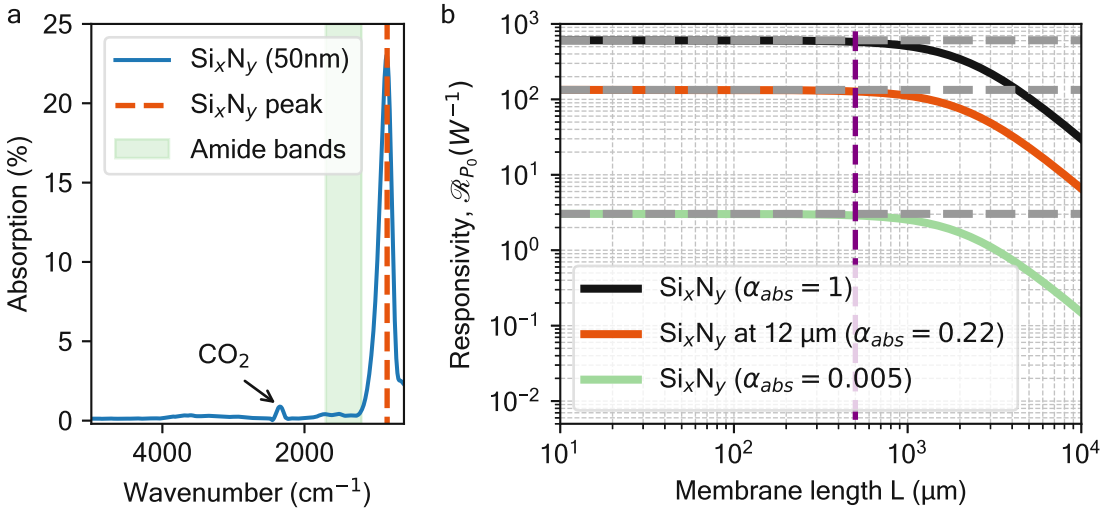

Fig. 2.3: (a) Absorption as a function of wavenumber of a 50 nm thin Si_xN_y membrane, obtained by transmission and reflection measurement using FTIR spectroscopy. (b) Theoretical power responsivity of a nanomechanical membrane as a function of the lateral size L and different absorptance values, based on the material parameters displayed in Table 2.1. The grey-dashed lines represent the theoretical responsivities when limited by conductive heat transfer only. For increasing membrane sizes $>$ 500 µm (purple-dashed line), the radiative heat transfer increasingly dominates the dissipation and, therefore, significantly deteriorates the responsivity [3].

500 µm (purple-dashed line), where the responsivity starts to be dominated by radiative heat transfer. A detailed experimental study on the impact of heat transfer mechanisms on the responsivity and thermal time constant can be found as a collaborative part of this thesis, see [3].

Given the assumption that the frequency resolution is exclusively constrained by the noise sources described in the previous section, with negligible contribution from transduction ($\kappa \ll 1$), one can proceed to estimate the sensitivity of the resonator.

Figure 2.4 presents the theoretical NEP as a function of the membranes' side length L, based on the parameters in Table 2.1 and full absorptance of the impinging power ($\alpha_{abs}(\lambda) = 1$). Due to the linear dependence of $\mathscr{R}_{P_0} \propto \alpha_{abs}(\lambda)$, the NEP for lower absorptance increases accordingly. For the estimation of the thermomechanical noise, we further assume a decent quality factor of $Q = 10^6$ and ideal resonator amplitude at the onset to nonlinearity by [62]:

$$\alpha_{NL} = \frac{3\pi^4}{64}(n^4 + m^4)\frac{Eh}{L^2} \tag{2.15}$$

$$z_r = \sqrt{\frac{8}{3\sqrt{3}}}\frac{1}{\sqrt{Q}}\sqrt{\frac{m\omega_0^2}{\alpha_{NL}}}. \tag{2.16}$$

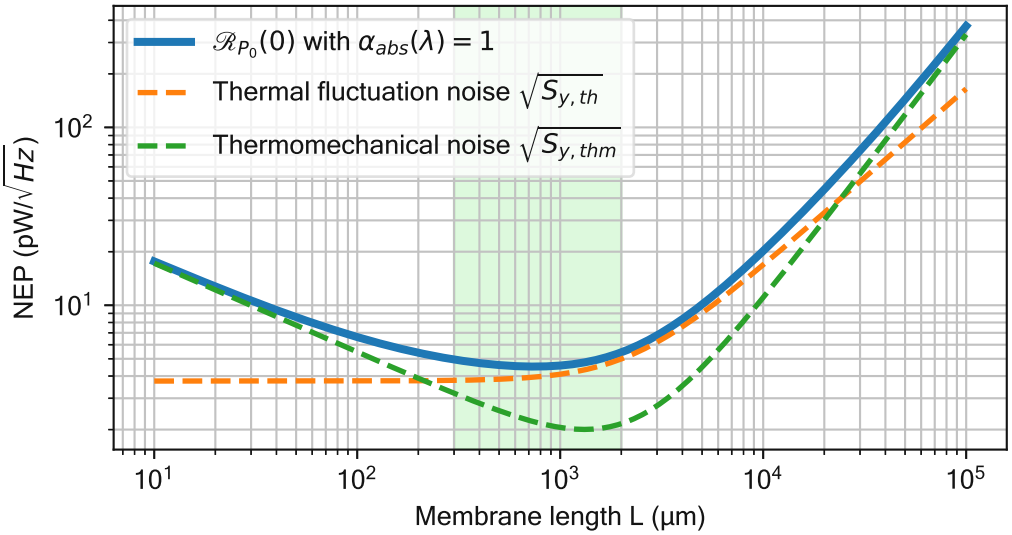

Fig. 2.4: Theoretical NEP and PSD of the main limiting noise sources assuming a full light-to-heat conversion ($\alpha_{abs}(\lambda) = 1$) on a bare Si_xN_y resonator, based on the material parameters in Table 2.1. Regarding the optimal lateral dimensions between 300 µm to 2000 µm, an NEP of approximately 4.5 pW/$\sqrt{\text{Hz}}$ can be reached.

Due to the low-pass characteristic of the temperature response, the thermal fluctuations set a constant noise floor up to a transition point approximately at 1000 µm, where the heat transfer changes from conduction to radiation. Including the contribution of thermomechanical noise, the optimal resonator size to reach the lowest NEP is in the range of $L = 300$ µm to 2000 µm. Within this range, an NEP of approximately 4.5 pW/$\sqrt{\text{Hz}}$ can be reached.

2.1.2 Performance in comparison to transmission spectroscopy

For a comparison of the performance of nanomechanical-based spectroscopy to transmission IR spectroscopy, one has to include the impact of the intensity noise of the probing light source with the fractional intensity $S_I(\omega)$ [1/Hz]. In general, one can express the signal-to-noise ratio (SNR) as the fraction of absorbed power by an analyte $P_{abs} = \alpha_{abs}(\lambda)P_0$ to the detected power P_{det} by [61]:

$$SNR = \frac{P_{abs}}{P_{det}\sqrt{S_I(\omega)}}. \tag{2.17}$$

In transmission spectroscopy, P_{det} depends on the transmittance $T(\lambda)$ with $P_{det} = T(\lambda)P_0$. Assuming the scenario of a small absorptance ($\alpha_{abs} \ll T(\lambda)$) and respectively, a large transmittance $T(\lambda) \approx 1$ and negligible reflectance, the SNR of transmission spectroscopy

can be approximated by [61]:

$$SNR \approx \frac{\alpha_{abs}(\lambda)}{\sqrt{S_I(\omega)}}. \tag{2.18}$$

This approximation of the SNR indicates that the detection limit of transmission spectroscopy scales with the absorptance, diminishing the detection limit when analyzing only a small sample. In contrast, assuming that the intensity noise of the light source can be resolved ($NEP \leq P_{abs}\sqrt{S_I(\omega)}$), the SNR of nanomechanical photothermal detection is approximately given by [61]:

$$SNR \approx \frac{1}{\sqrt{S_I(\omega)}}. \tag{2.19}$$

This independence of the absorptance leads to a so-called *photothermal enhancement* factor of $1/\alpha_{abs}(\lambda)$ of the direct NAM-IR spectroscopy over the transmission spectroscopy, with a performance comparable to a balanced detection scheme.[61] The *photothermal enhancement* plays a role with "noisy" light sources, such as quantum cascade lasers. However, in the case that the intensity noise of the light source can not be resolved by the nanomechanical photothermal sensor ($NEP > P_{abs}\sqrt{S_I(\omega)}$), the SNR is given by

$$SNR = \frac{P_{abs}}{NEP}. \tag{2.20}$$

2.2 Nanomechanical response to mass

When utilizing the resonator for direct IR spectroscopy, the analyte is deposited on the resonator before irradiation. Compared to heat detection by thermal expansion, the additional mass adds inertia to the resonator, resulting in a change in the resonance frequency. This enhances the potential of direct NAM-IR spectroscopy by enabling the identification and quantification of a substance on the resonator in a single measurement.

Mass detection is historically one of the most common applications of nanomechanical resonators [69, 70, 39]. Former studies pushing the limits of mass sensing by nanomechanical resonators demonstrated exceptional sensitivities for detecting single molecules [71] down to the single proton level [38]. Assuming that the additional mass does not alter the intrinsic mechanical properties of the resonator, one can approximate the added mass as an effective increase of the density.

For the case that the entire resonator is covered, the response to mass can be expressed as the derivative of the eigenfrequency $\omega_{n,m}$ concerning the resonator mass m_0 by [62]:

$$\mathscr{R}_m = \frac{1}{\omega(m)} \frac{\delta\omega_0}{\delta m}\bigg|_{m=m_0} = -\frac{1}{2m_0} \tag{2.21}$$

Notably, this expression resembles a linearized response for minor changes and is invalid for larger mass loads. For this case, the response can be approximated either by a higher-order Taylor series or an analytical solution to obtain the load by the change in resonance frequency for an increased density. One can derive a formalism to determine the loaded mass by utilizing the eigenfrequency model of a squared membrane as outlined in [62, p. 52]. Further, the density is defined as $\rho_0 = m_0/(L^2 h)$ where ρ_{load}, f_{load} denote the effective density and frequency of the resonator with added mass, respectively.

$$\rho_{load} = \left(\frac{\gamma}{2L}\right)^2 \frac{\sigma}{f_{load}} \tag{2.22}$$

$$m_{load} = L^2 h\,(\rho_{load} - \rho_0) \tag{2.23}$$

$$= L^2 h \left[\left(\frac{\gamma}{2L}\right)^2 \frac{\sigma}{f_{load}} - \left(\frac{\gamma}{2L}\right)^2 \frac{\sigma}{f_0}\right] \tag{2.24}$$

$$= \sigma h \left(\frac{\gamma}{2}\right)^2 \left[\frac{1}{f_{load}^2} - \frac{1}{f_0^2}\right] \tag{2.25}$$

The pre-factor $\gamma = \sqrt{n^2 + m^2}$ accounts for the different harmonic modes of the membrane. Figure 2.5 presents the resonance frequency change of a L =500 µm squared Si_xN_y membrane for increasing mass loads. As can be observed, even for the addition of a fraction of the resonators' mass, the linearized response strongly diverges from the estimated frequency. Thus, for a precise estimation of mass loads, the analytical solution Equation 2.25 should be used.

2.3 Impact of the transduction on the NEP

Over the past decades of nanomechanical-based sensor systems, numerous concepts for transduction, namely the actuation and detection of motion, have been developed. An extensive collection of the most common techniques and underlying theory can be found in chapter 4 of Schmid et al. [62]. In the context of nanomechanical-based IR spectroscopy, the transduction should ideally not reduce the power responsivity nor add more noise to the system.

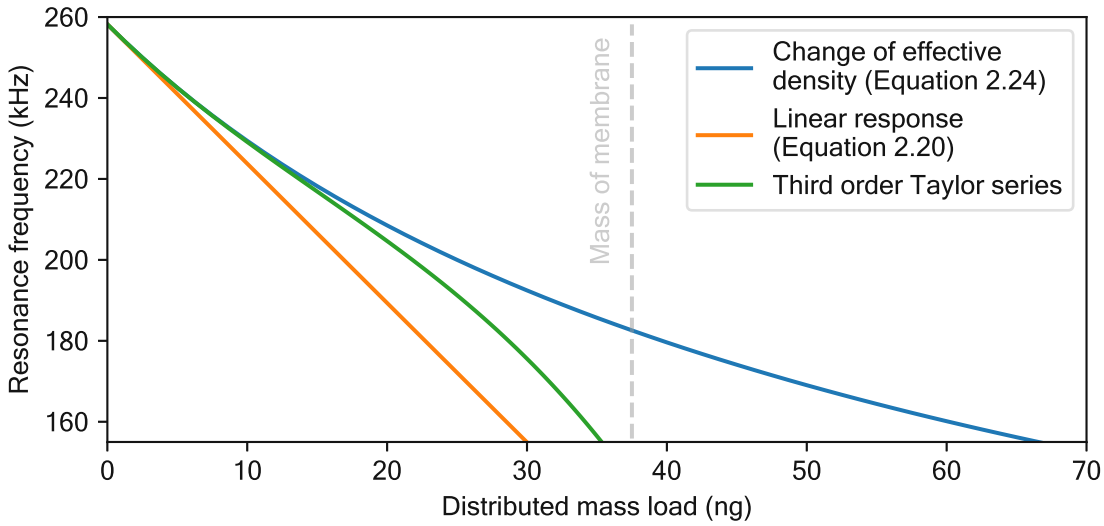

Fig. 2.5: Nanomechanical response to additional distributed mass for a 500 µm sized membrane. The comparison shows the frequency change assuming a linear response following Equation 2.21, a third-order Taylor expansion, and the analytical solution based on the change of density Equation 2.25.

In a recent study featuring NAM-IR spectroscopy, an electrodynamical transduction scheme was implemented [57]. In this approach, the effect of the Lorentz force is used to actuate and detect the out-of-plane motion of the resonator. As illustrated in Figure 2.6, this is achieved by two separate electrodes placed on the resonator surface aligned perpendicular to a homogeneous magnetic field. The resulting Lorentz force can deflect and drive the resonator by applying a sinusoidal current through one electrode. Vice versa, the induced voltage on the other electrode can be used to detect the oscillation. Higher harmonic modes can be transduced depending on the resonator's electrode position as long as the overall induced voltage does not cancel itself out.

Although this method enables a fully integrated electronic transduction of the resonator, the metallic traces increase the heat transfer by conduction, thereby reducing the power responsivity ($\mathscr{R}_{P_0} \propto 1/G$). In contrast, the increased conductance reduces the thermal fluctuation noise $S_{y,th} \propto 1/G$. However, regarding the sensitivity, the $NEP \propto \sqrt{G}$ increases with thermal conductance. Furthermore, the implementation of electrodes introduces electronic noise to the system, such as thermal noise (Johnson-Nyquist) and 1/f noise (Hooge), also referred to as "Flicker" noise [62, 150 ff.].

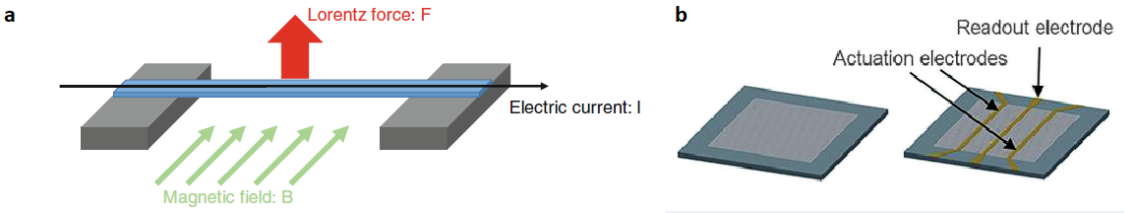

Fig. 2.6: Schematic of (a) a string and (b) a membrane with integrated electrodes for electrodynamical transduction. [62, 57]. Published under license number 5754231216592, John Willey and Sons.

To estimate the impact of the electrodynamical transduction on the frequency resolution, one can compare the magnitude of thermal fluctuation-related noise of the electrode described by Johnson-Nyquist to the thermomechanical noise peak of the resonator. Analog to the Brownian motion of particles, the random thermally excited vibration of the charge carriers in the electrode introduces noise to the electrical conduction [62, p.151]. Due to its thermal nature, this noise can be equally described by the fluctuation-dissipation theorem [72, 73] assuming a white noise PSD described by J.B. Johnson [74] in the units of [V^2/Hz]:

$$S_{V_{th}} = 4k_B T R\,, \tag{2.26}$$

where R is the resistance of the conductor/electrode. To compare the electrical noise level with the thermomechanical noise by displacement fluctuations, one must translate the voltage PSD to an amplitude PSD. This can be achieved by relating $S_{V_{th}}$ with the voltage induced in the electrode when moving in the magnetic field. Assuming a sinusoidal mode shape of the electrode along the membrane resonator, as depicted in Figure 2.6, one can calculate the induced voltage by [62, p.111]:

$$V_{EMF_{Ind}} = B\sqrt{2}z_0 f_1 L[1-\cos(n\pi)]\,, \tag{2.27}$$

where $f_1 = f_n/n$ is the modal resonance frequency, B the perpendicular magnetic field strength and z_0 the maximum displacement of the resonator & electrode, respectively. For the fundamental mode $n = 1$, one can readily derive the displacement to a given voltage by:

$$z_0 = V_{EMF_{Ind}}\left[B\sqrt{2}f_0 L\right]^{-1}\,. \tag{2.28}$$

By substituting $V^2_{EMF_{Ind}}$ by the respective voltage noise power spectral density $S_{V_{th}}$ (2.26), one can relate the induced voltage with the voltage-noise defined by Johnson-Nyquist

to translate it into an amplitude PSD [m^2/Hz]:

$$S_{z_{Vth}} = 4k_BTR\left[B\sqrt{2}f_0L\right]^{-2}. \tag{2.29}$$

To finally appraise the contribution of $S_{z_{Vth}}$ to the fractional frequency noise of the resonator, one can compare the displacement driven by the Johnson-Nyquist noise to the thermomechanical noise peak of the resonator. Assuming a Lorentzian peak with an average thermomechanical displacement of $< z_{th}^2 >= k_BT/m_{eff}\omega_0^2$, this can be approximated by [62, p.149]:

$$S_{z_{th}} = \frac{4k_BTQ}{m_{eff}\omega_0^3}. \tag{2.30}$$

Together with the derived displacement noise by the electrode, one can estimate the impact of the transduction on the noise by calculating the dimensionless factor $\mathscr{K}^2 = S_{z_{Vth}}/S_{z_{th}}$ (introduced in Section 2.1.1, [62, p.162]). For $\mathscr{K} < 1$, the transduction scheme can resolve the thermomechanical peak. Combinding Equation 2.29 and Equation 2.30, one obtains the following expression for the estimation of $\mathscr{K}$:

$$\mathscr{K}^2 = \underbrace{\frac{R}{B^2L^2}}_{\text{Transduction}} \underbrace{\frac{2\pi^2\, m_{eff}\omega_0}{Q}}_{\text{Resonator}}. \tag{2.31}$$

As, in general, a small $\mathscr{K}$ is desired, the implemented electrodes should have a low resistance and be placed in a large magnetic field. The resonator should have a low effective mass and high mechanical Q factor. Although Equation 2.31 indicates that a low resonance frequency is beneficial, the increasing contribution of Flicker noise $\propto 1/\omega_0$ will counteract this gain.

For an indicative approximation of $\mathscr{K}$, we consider a 50 nm thin squared membrane with $L = 500\,\mu$m made of Si_xN_y (see parameters Table 2.1). We further assume an electrode with a resistance of $R = 100\,\Omega$ placed in a magnetic field of $B = 0.5\,$T. Based on an empirical intrinsic quality factor of $Q_{intrinsic} = 3400$ (see [52]) and the damping dilution model by Schmid et al. [62, p.101], one can estimate a quality factor of $Q \approx 1.2\cdot10^6$ for a bare Si_xN_y resonator. By the insertion to Equation 2.31 we obtain a factor of $\mathscr{K} \approx 0.74$.

In this scenario, the frequency resolution of the resonator is not limited by electronic noise originating from the transduction scheme. However, in practice, the implementation of electrodes and analytes on the surface significantly reduces the resonator's quality factor. Empirical values from this work obtained from a 1 mm squared membrane featuring electrodes reached a mechanical time constant of about $\tau_{mech} = 50\,$ms. As a result, the realistic quality factor is only $Q = 0.5\,\omega_0\,\tau_{mech} \approx 40\cdot10^3$.

This notably increases $\mathscr{K} \approx 4$, causing transduction noise to dominate the frequency resolution. Consequently, the theoretical NEP is increased to $10.9\,\mathrm{pW}/\sqrt{\mathrm{Hz}}$ compared to $4.6\,\mathrm{pW}/\sqrt{\mathrm{Hz}}$ for the same membrane without electrodes. Despite the dominant noise, electrodynamical transduction remains a very practical solution that can be readily implemented to enable an integrated readout of the resonator. Till today, this transduction is used in many applications which have enabled nanomechanical photothermal IR detection with $NEP = 7\,\mathrm{pW}/\sqrt{\mathrm{Hz}}$ and photothermal polarization microscopy reaching 3 Å resolution [75].

2.4 Sampling techniques for direct NAM-IR spectroscopy

To utilize direct NAM-IR spectroscopy, the analyte must be brought to the resonator surface. Most studies presenting NAM-IR spectroscopy [76, 55, 56, 57, 77] accomplished this by employing common aerosol techniques. In this approach, the liquid analyte (or dispersion of nanoparticles) is nebulized and dried to airborne particles. By incorporating a perforation into the resonator, aerosols can flow through it, effectively utilizing it as an impaction-based particle filter. To derive conclusions for the optimization of aerosol-based sampling, the following section briefly introduces the dependencies of the sampling efficiency based on the main capturing mechanisms.

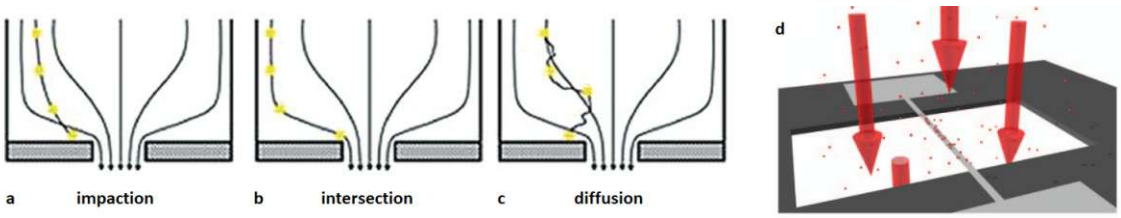

Fig. 2.7: Schematic of the three major collection mechanisms for airborne particles: (a) diffusion (b) interception and (c) impaction, taken from [57]. (d) Schematic of aerosol sampling on a string resonator [76]. Published under license number 5754231216592, John Willey and Sons.

Figure 2.7(a-c) illustrates the three major mechanisms for capturing/filtering particles from an aerosol stream: diffusion, interception, and impaction. The combined effects of these mechanisms determine the overall capturing efficiency. By focusing on the 'fiber diameter' (considering a filter-fiber element) and aerosol velocity, one can approximate the collection efficiency E_C based on the single-fiber efficiency theory [78, 79] and sim-

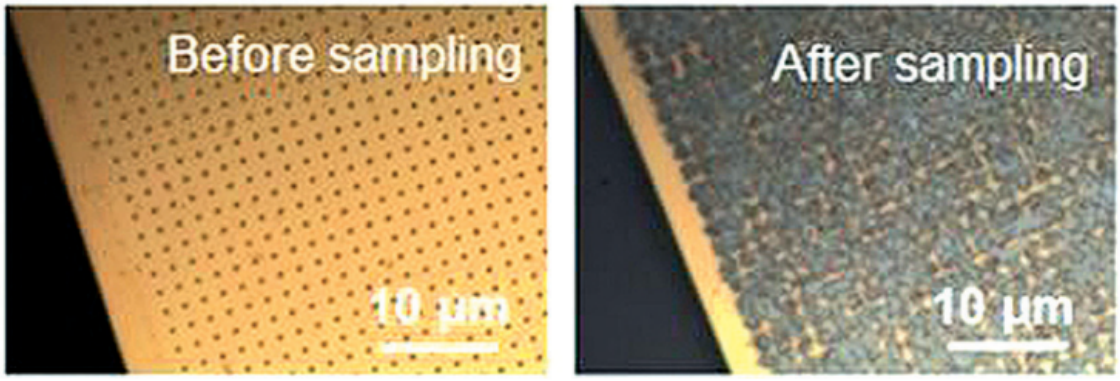

Fig. 2.8: Micrograph of a Si_xN_y membrane resonator with a 1 µm perforation (a) before and (b) after sampling with an aerosol of indomethacin. Due to the small perforation, the membrane gets clogged during the sampling. Published under license number 5754231216592, John Willey and Sons [57].

plify it to a model proposed by [76]:

$$E_C = E_D + E_{Im} = \underbrace{a_1(d_f u)^{-2/3}}_{E_D} + \underbrace{a_2 \frac{u}{d_f}\left(1 + \frac{d_p}{d_f}\right)}_{E_{Im}}, \tag{2.32}$$

where E_D, E_{Im} are the respective efficiencies for diffusion, impaction, and d_f is the fiber diameter and u the aerosol velocity. The pre-factors a_1, a_2 comprise specific properties of the particle and fluid in which they are suspended, such as dynamic viscosity and the Kuwabara hydrodynamic factor (see [79, 76] for more detail). The sampling efficiency for interception of particles depends on the ratio of the single fiber to particle diameter but not the velocity and is excluded from this approximation.
From Equation 2.32, one can directly deduce that the aerosol velocity and smaller fiber diameter linearly increase the efficiency. Previous studies utilizing a $d_f = 3\,\mu m$ wide Si_xN_y string resonator and high particle velocity of $52.5\,m\,s^{-1}$ demonstrated a single-fibre collection efficiency up to 65(31) % for the sampling of 28 nm silica nanospheres [76]. Concerning the theoretical collection efficiency defined by Equation 2.32, one can derive the following conclusion for an optimized aerosol sampling for NAM-IR spectroscopy:

- Find a trade-off between a small perforation cross-section to maximize the aerosol velocity without causing a turbulent flow or clogging during sampling.
- Minimize the pitch to reduce the effective fiber diameter.

In a first attempt, this has been experimentally demonstrated for NAM-IR spectroscopy with fully perforated membrane resonators reaching a sampling efficiency of 59(21) %

[57]. However, as can be observed in Figure 2.8, the perforation was applied to the entire resonator with a comparably small perforation of 1 µm and large pitch. This can lead to clogging of the resonator during sampling. As a result, the aerosol flow is interrupted up to the rupture of the thin resonator under the constant pulling force by the sampling pump.

Alternatively, a liquid analyte can be dropped- or spin-casted on the resonator as depicted in Figure 2.9(b,c) - see for example [59, 60, 75]. In this method, the analyte is applied directly. Initially, a small droplet of the solution is deposited onto the center of the resonator, and it is left to dry or spread through spinning. However, this process often leads to a 'coffee-ring' effect, where the dried analyte concentrates outside the membrane. A possible solution would be a localized surface functionalization to 'activate' the resonator's center by enabling a covalent bond of the analyte to the surface.

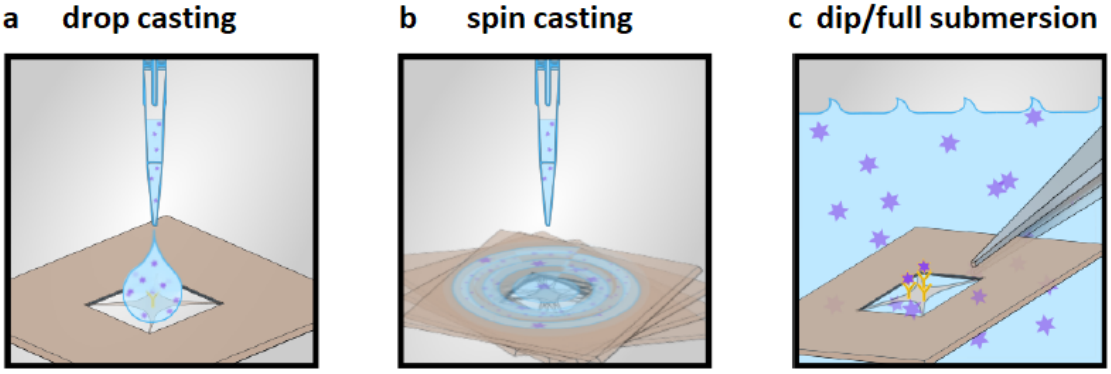

Fig. 2.9: Schematic of the liquid sample deposition methods: (a) drop casting, (b) spin casting, and (c) full submersion. For up-concentrating the analyte by drop-casting or full submersion, a suitable surface functionalization must be applied before sampling. Copyright 2023, adapted under a CC-BY 4.0 license, by R. West et al. [61].

In combination with drop-casting, this is, for example, made possible by adding a localized silanization on sample plates deployed in Matrix-Assisted Laser Desorption/Ionization (MALDI). Furthermore, a suited functionalization allows the full submersion/incubation of the resonator in the solved analyte to specifically capture the target compound, as depicted in Figure 2.7a - see for example [80]. Depending on the adhesion of the analyte to the resonator surface, a full submersion, even without functionalization, can be sufficient and is a common practice for the analysis based on cantilevers [81].

Besides drop-casting and surface functionalization, deposition by spin casting represents a simple method that provides high reproducibility, particularly when applying viscous analytes, such as for polymeric films.

This has successfully been demonstrated for the detection of polyvinylpyrrolidone (PVP) [55] and for the evaluation of solid-state forms of tadalafil films through NAM-IR spectroscopy [59]. Furthermore, it is an appropriate method if the focus of the study is set to the analysis of low concentrations where a high distribution of the analyte is desired, such as photothermal microscopy of single molecules or single nanoparticles [60, 82].

2.5 Conclusions for nanomechanical-based IR spectroscopy

Based on the presented theory, the following considerations can be made for designing a nanomechanical resonator for IR spectroscopy:

Resonator geometry. Using Si_xN_y as the resonator material, the lowest NEP can be achieved through the utilization of a thin resonator with a lateral size ranging from 300 µm to 2000 µm. The NEP can be further decreased by reducing the resonators' thickness. However, this will have a negative impact on the robustness and fabrication yield. Alternatively, the heat transfer by conduction can be minimized by reducing the cross-sectional area of the suspension. This can be accomplished by changing the resonator geometry, e.g., from a membrane to a trampoline-like shape.

Tensile stress. The tensile stress of the resonator represents a trade-off between high power responsivity and low fractional frequency noise. While the power responsivity would benefit from reduced stress ($\mathscr{R}_{P_0} \propto 1/\sigma_0$), the reduced Q factor, in contrast, will consequently increase the frequency noise. Considering the positive impact of the Q on $\mathscr{K}$ when using an electrodynamic transduction scheme supports the use of a higher tensile stress. However, in practice, it is not possible to reach the theoretical frequency resolution of $\sigma_y = 10^{-10}$ as for stoichiometric Si_3N_4 with a tensile stress of $\sigma_0 = 1\,\mathrm{GPa}$. Therefore, the gain of the power responsivity by reducing the tensile stress dominates this trade-off.

Absorptance and heat transfer. Apart from the tensile stress, the responsivity to impinging power scales with the absorptance and inversely to conductance $\mathscr{R}_{P_0} \propto \alpha_{abs}(\lambda)/G$. The implementation of an absorbing element will also significantly increase the heat transfer. Higher absorptance is accompanied by higher emissivity, which consequently increases the heat transfer by radiation. Likewise, broad spectral absorbers such as impedance-matched films made of metal are good thermal conductors.

Regarding NAM-IR spectroscopy, it is more effective to directly measure the absorption spectrum of compounds by detecting their heat dissipation on the resonator, rather than relying on indirect spectroscopy based on transmitted light. Direct measurement reduces the additional heat capacity when compared to a broad spectral absorber.

For the application of photothermal IR detection, where a broad spectral absorber is needed, the resonator size should ideally not exceed the range dominated by heat conduction. This way, the gain by additional absorptance will not be counteracted by the heat loss due to radiation, thereby boosting the power responsivity.

3 Experimental methods

This chapter outlines the fabrication technique used to create nanomechanical resonators and the methods employed to monitor their resonance frequency. Additionally, the working principle of Fourier-transform infrared (FTIR) spectroscopy is introduced.

3.1 Fabrication

All nanomechanical resonators in this work were made of silicon nitride using standard clean room techniques based on UV lithography. With respect to gaining an enhanced power responsivity by lower tensile stress, a silicon-rich Si_xN_y was used. All fabrication steps in this thesis were conducted on commercial 4-inch silicon wafers coated on both sides with 50 nm Si_xN_y deposited using low-pressure chemical vapor deposition (LPCVD). Due to deviations in the LPCVD process, the tensile stress of the Si_xN_y in this thesis varied between 50 MPa to 150 MPa.

Figure 3.1 schematically visualizes the major fabrication steps on the example of a Si_xN_y string and the associated effects of each treatment. For each process step, a photosensitive layer (photo-resist) is spin-coated on the surface of the wafer, which can be structured by a defined exposure to UV light through a shadow mask and subsequent development/removal of exposed photo-resist. Depending on the process (top-down or bottom-up), the structured photo-resist is used as a deposition or etching mask. During all steps, an additional protective photo-resist is added to the unprocessed surface to protect it from unwanted processing, scratches, or contamination during fabrication. Further, after the completion of every step, the wafer is thoroughly cleaned in an ultrasonic bath using acetone, isopropyl alcohol, and Milli-Q water. The presented process cycle resembles a general fabrication protocol and can be equally used to fabricate any suspended Si_xN_y geometry used in this work, including perforated trampolines and membranes.

A. Double side polished silicon wafer with a Si-crystallization of <100>and double-side coated by 50 nm LPCVD Si_xN_y .

B. The fabrication initiates with the addition of metallization to form the electrodes, employing a 'bottom-up' technique. This involves spin-coating the front side with a reverse-bake resist, followed by structuring it in a two-step exposition process. The developed resist delineates the electrode pattern, featuring an additional overhang strategically designed to facilitate the lifting off of residual resist.

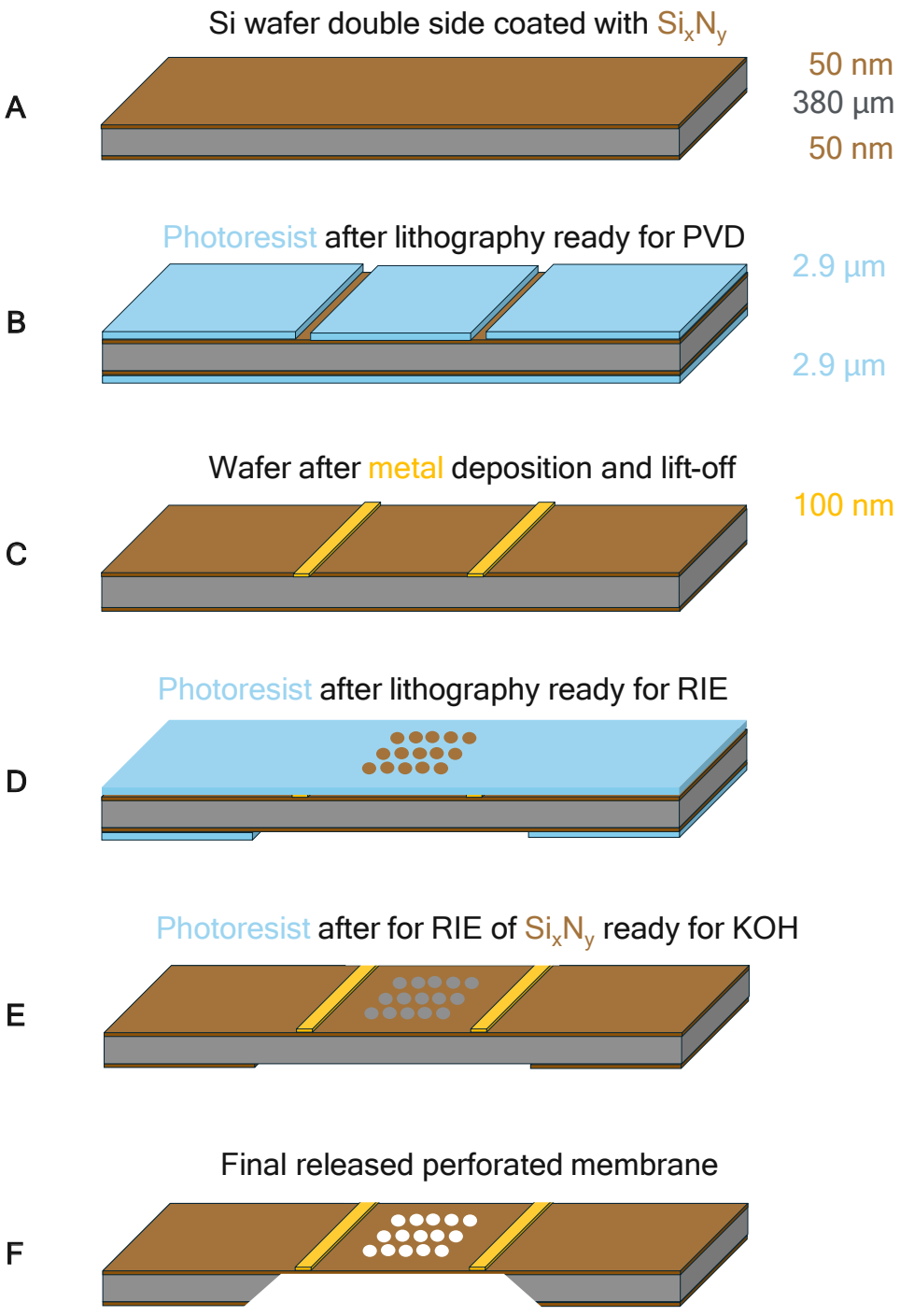

Fig. 3.1: Illustration of the main process steps for fabricating a suspended Si_xN_y resonator on the example of a single string. For each step, a photosensitive resist is spin-coated and structured by UV exposure through a dedicated designed shadow mask, followed by developing, and a top-down or bottom-up process.

The metallization is done by physical vapor deposition (PVD) of an adhesion layer (typically 10 nm chromium) followed by 100 nm gold.

C. After metal deposition, the resist is removed by a common 'lift-off' procedure. In this procedure, the wafer is cleaned for several minutes in three consecutive ultrasonic baths of acetone and isopropyl alcohol Figure 3.1 C shows the cleaned wafer featuring electrodes.

D. In the next step, the perforation of the resonator is etched into the top Si_xN_y layer by reactive ion etching (RIE). Therefore, the front side is spin-coated with a positive resist and structured by UV exposition. The developed resist can be used as an etching mask for the Si_xN_y layer using RIE with a CF_4/O_2 plasma. After completion, the residual resist is stripped by a standard lift-off process. The same process is repeated on the backside to fabricate an etch mask for the release of the membrane.

E. For the final release of the resonator, the backside Si_xN_y layer needs to be structured to generate an etch-mask for the potassium hydroxide (KOH) bath. Therefore, another lithography is performed using a mask for the back-side openings and subsequently removes the Si_xN_y by RIE.

F. After this preparation, the wafer can be drawn in a bath of 40 wt% KOH for anisotropic wet etching through the whole Si wafer. The advantage of KOH is its selective etch rate, which depends on the crystal orientation. In the case of silicon, it is therefore important to use wafers with an orientation of [100]. The etch rate ratio of the orientation is approximately [111]:[100] = 1:400, which leads to a trapezoidal grave with an angle of $\arctan(\sqrt{2}) = 54.7^\circ$. Additionally, due to the high etch selectivity of Si compared to the Si_xN_y (1000:1), the resonator material is rarely affected by the process as long as they are not exposed for several hours after breaking through the wafer. With a nominal wafer thickness of 380 µm Si, the full release takes about 7.5 hours to reach the top Si_xN_y layer. In the last step, the released wafer is gently cleaned in several fresh beakers of Milli-Q water and manually diced into single resonator chips after drying in ambient conditions.

3.2 Frequency tracking schemes

NAM-IR spectroscopy relies fundamentally on the thermally induced detuning of the resonance frequency. Consequently, the precise tracking of frequency with respect to resolution and bandwidth assumes critical importance for its applicability and sensitivity. In an ideal tracking scheme, the frequency resolution should not limit the sensitivity. A widely used technique in the NEMS community for frequency tracking is based on a lock-in amplifier in a so-called phase-locked loop (PLL) configuration [83]. Figure 3.2a shows a block diagram of a typical PLL scheme. In this method, a PID controller responds to changes in the resonance frequency by maintaining a constant phase relation between the output and input signal. This is done by matching the lock-in amplifier's internal/local oscillator (LO), which is used to drive the resonator, to the measured input frequency. A commercial PLL configuration from Zurich Instruments was used throughout most measurements presented in this thesis.

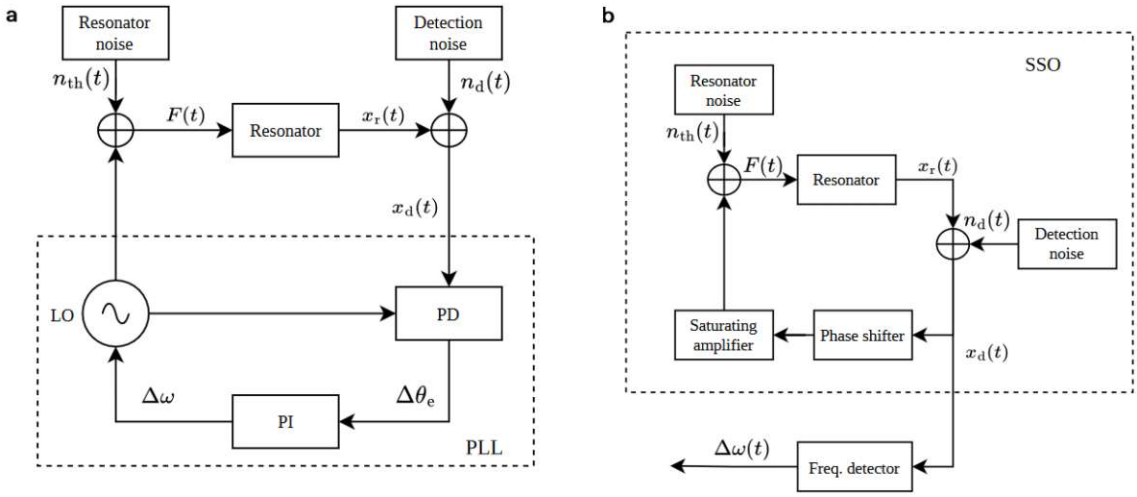

Fig. 3.2: Block diagrams highlighting the main processing components of a frequency tracking scheme based on, (a) a phase-locked-loop (PLL), and (b) a self-sustained oscillator (SSO). Figure adapted from [8] under license number RNP/24/APR/077595.

Instead of maintaining a constant phase relation, the resonator can be transduced by a self-sustained oscillation (SSO). In this approach, the sinusoidal signal coming from the resonator is amplified, shifted in phase by $\pi/2$, and sent back to drive the resonator. The SSO scheme has the advantage of maintaining the resonator on resonance without the need to adjust a PID controller. However, compared to the PLL, the specific phase delay for a given frequency needs to be adapted for larger frequency changes.
In the PLL configuration, the current frequency is obtained from the phase difference to the local oscillator. In comparison, for the SSO scheme a frequency counter (or addi-

tional PLL) is used outside of the loop, as depicted in Figure 3.2b. The ultimate frequency resolution is limited by the internal clock of the lock-in or frequency counter. However, in the case of nanomechanical resonators, the resolution is strongly dominated by the thermal- and thermomechanical fractional frequency noise.
In addition to resolution, another crucial parameter for an "ideal" tracking scheme is the bandwidth and, respectively, the response time. For a PLL scheme, the time to adapt to changes in the resonance frequency is defined by the lowpass characteristic of the PD/PI control loop. In contrast, due to the nature of the SSO, the response to changes in frequency is instant and only limited by the integration time of the frequency counter. Therefore, the SSO configuration enables a significantly faster and more robust tracking of frequency changes than the PLL.
The most common approach for an SSO-based tracking scheme is the self-sustained actuation of the resonator by a phase-shifted pulse. The pulse is triggered by zero-crossing of the periodic input signal. As part of the thesis of Hajrudin Besic, an analog and digital SSO with a frequency counter was developed and tested for application in NAM-IR spectroscopy [8]. Throughout this study, it was demonstrated that both tracking schemes can achieve the same frequency resolution. The faster and more robust tracking while providing the same resolution makes the SSO scheme the preferred solution for NAM-IR spectroscopy.

3.3 Fundamentals of FTIR spectroscopy

FTIR spectroscopy's fast acquisition and large spectral range have made it one of the most proliferated techniques for the optical analysis and identification of chemical compounds. The essence of this technique lies in modulating a wide spectral light source and transforming the recorded interferogram into a spectrum through Fourier transformation. Figure 3.3 shows the main components and optical pathways of a common FTIR spectrometer. The light source (so-called *globar*) comprises an electrically heated silicon carbide rod, which acts as a black-body radiator with a temperature of $>1350\,\mathrm{K}$ (for the example of a Bruker Vertex 70 spectrometer). The emitted spectrum is in the range of around 1.4 µm to 20 µm / 7000 cm^{-1} to 500 cm^{-1}). After passing a defined aperture followed by optical collimation, the light is modulated in a Michelson interferometer configuration, dividing the light by a beam splitter into a static and a moving path. During this modulation, an IR detector continuously records the transmitted (or reflected) light from the sample. In common FTIR systems, a pyroelectric element made of Thallium-doped Lutetium Gadolinium Silicate (DTLGS) is typically used.

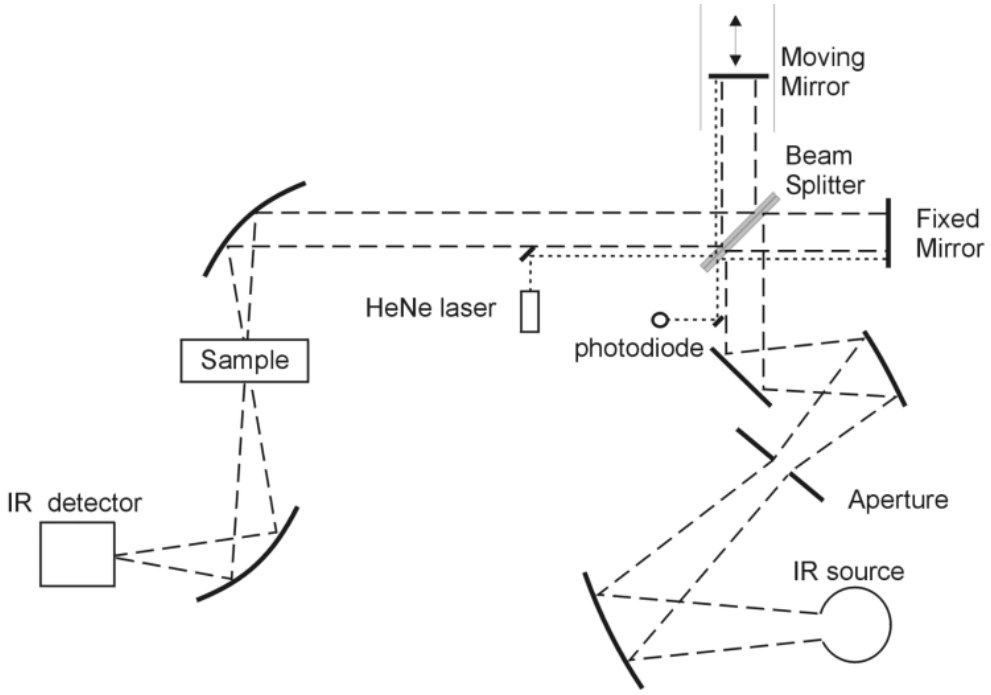

Fig. 3.3: Schematic principle of FTIR spectrometer comprising a broad spectral light source modulated by a Michelson interferometer. A monochromatic reference beam enables a precise determination of the optical pathway. Reproduced with kind permission by B. Lendl and [84].

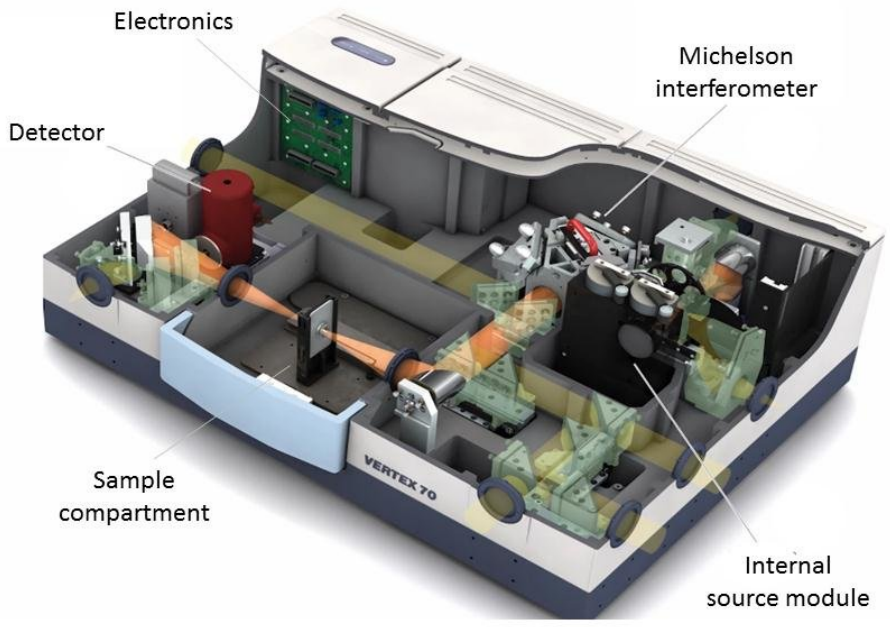

Fig. 3.4: Schematic of a commercial FTIR spectrometer highlighting the key components. The internal source module is a globar made of a SiC rod. Image courtesy by Bruker Optics (2023).

To enable higher sensitivity, this is often replaced by a liquid nitrogen-cooled detector made of mercury cadmium telluride (MCT). For better visualization of all components, a schematic of a commercial FTIR spectrometer (Bruker Vertex 70) is displayed in Figure 3.4.

Figure 3.5a shows a common interferogram showing the alternating light intensity of a commercial FTIR. At the point of equal optical distance, also called zero path difference (ZPD), all wavelengths form a constructive interference, as illustrated in Figure 3.5a. This significant increase and decrease of the intensity is commonly known as the *center burst*.

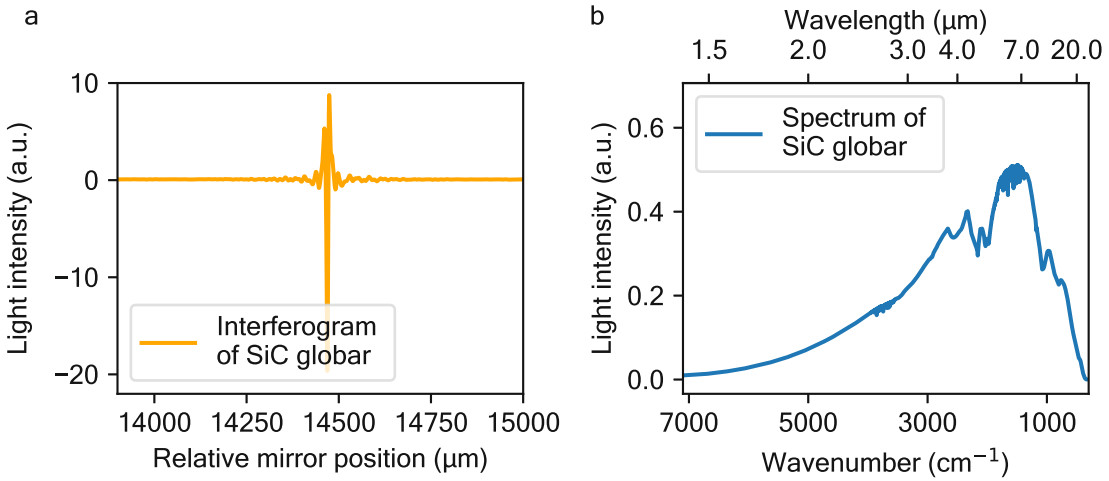

Fig. 3.5: (a) Closeup of the center burst of an interferogram recorded by a commercial FTIR light source comprising an uncooled DTLGS detector and (b) Fourier-transformed spectrum showing the emission profile of the globar.

Applying a Fourier transformation to the interferogram results in the black body spectrum of the globar, as depicted in Figure 3.5b. This mathematical operation transforms the recorded intensity as a function of the optical pathway in [cm] to spectral intensities [1/cm]. The exact mirror velocity and location is continuously obtained from the interference pattern of a monochromatic light source, e.g., a diode or helium-neon laser. The features within the black-body spectrum in Figure 3.5b originate from a non-linear response of the detector, and atmospheric absorption bands of water vapor and CO_2 which can be reduced by purging the optical pathways with unpolar gases such as nitrogen. To compensate for the intensity profile of the globar and account for atmospheric absorptions, typically, a background spectrum of the system is recorded before the sample is applied.

One of the major disadvantages in transmission spectroscopy is the dependence of the SNR on the analyte absorptance (see Section 2.1.2) and the sample preparation. From the early years of FTIR spectroscopy till today, the calibration curve of the device for a specific chemical compound is often obtained by mixing different concentrations of the analyte with a powder of potassium bromide (KBr) and pressing it into pellets. A time-consuming and tedious process.

Novel acquisition techniques such as attenuated total reflectance (ATR)-FTIR spectroscopy significantly improved the feasibility of applying chemical compounds for fast analysis. In this approach, the light from the FTIR is focused on a crystal, typically made of Zinc selenide (ZnSe) or diamond, at an angle of total internal reflection. The resulting evanescent field at the crystal surface is highly sensitive to absorption, reducing the reflected light's overall intensity. This enables the simple application of solid or liquid chemical compounds on the surface of the crystal instead of pressing it into pellets. Like with transmission spectroscopy, the spectrum can be again obtained by subtracting the background spectrum of the clean crystal from the spectrum of a sampled crystal surface. For a more detailed insight into the technique FTIR spectrometry and accompanying methods, see P.Griffiths & J. De Haseth [85].

4 The story of an ideal absorber

The following chapter's results, formulations, figures, and discussions are based on the publication [2].

Efficient absorbers of electromagnetic radiation are a fundamental element of infrared (IR)/terahertz (THz) technology. In particular, thermal IR/THz detectors have remained the only technology covering the entire spectral range from the visible to the far-IR (THz) regime. They exploit the conversion of the absorbed photothermal power to either a change in electrical resistance or electric potential, as in bolometers or pyroelectrics and thermocouples, respectively [86]. Considering the limitations discussed in the theory chapter (see Section 2.1.1), bare Si_xN_y shows a significant drawback when utilizing the nanomechanical resonator as a photothermal detector for infrared light. The low absorption coefficient to a large spectral range strongly reduces the power responsivity. This can be improved by adding a suitable absorber to the resonator. Ideally, the absorber should provide a high absorption coefficient over a broad spectral range without increasing the thermal capacity and conduction. The following chapter delves into potential absorption techniques and describes the pathway to an optimized absorber for application NAM-IR detection.

4.1 Trade-offs in absorption techniques

An absorber suitable for IR detection should provide long-term stability and a broad and linear spectral response while having a small thermal mass. This has been the focus for advancement in IR/THz detection for decades and has led to a reduction in the effective thickness of the absorber to the order of 10 nm in the present day [86]. At this scale, contemporary solutions are numerous: from antenna structures [87, 88, 89] to metamaterials [90, 91, 92], which promise absorptivities up to 100 % but are always limited by their resonance bandwidth. A progressive solution to improve the spectral range of detection has been to use a stack of plasmonic structures with differing lateral sizes; nonetheless, the bandwidth of these sensors remains limited to a small range e.g., from 0.8 to 1.3 THz [93]. A most recent thrust toward the ultimate limit of uncooled detection has been to employ the exceptional properties of 2D materials such as graphene [86], even making the detector itself the primary absorber, for example, as uncooled NEMS resonator [54]. However, due to graphene's low absorptivity in the near-IR to mid-IR of only 2.3 % [94, 95], thicker layers or modifications using plasmonic metastructures are still required.

A more traditional method of absorbing IR light, which is typically used in thermal detectors such as a Golay cell, is the application of an engineered metallic thin-film with a sheet resistance matching half the free space impedance $\sqrt{\mu_0/4\varepsilon_0} \approx 188\,\Omega$ [96, 97, 98]. Here, μ_0 and ε_0 are the magnetic and electric permittivity in vacuum. Based on the theory introduced by Woltersdorff [98] and further extended by Hadley et al. [99] and Hilsum[100], a wavelength-independent absorptivity of up to 50 % can be achieved, assuming the optical constants n, κ are approximately equal. However, for metals such as gold, this criterion is only valid in the far-IR.

Many approaches using thin layers of e.g. bismuth, silver (Ag), or platinum [101, 102, 103, 104, 105, 106], unseeded metastructures [107], and alloys, such as titanium nitride (TiN), nickel-chromium (NiCr)[45, 108], and indium-tin-oxide (ITO)[109], have been successfully tested for this purpose. However, some alloys/metals are prone to oxidization, affecting the absorptivity over time. Regarding the thickness needed to match the desired impedance, alloys such as TiN, with an optimum of 14 nm, would be in the same dimension as the nanomechanical resonator itself [1] and thereby add significant thermal mass and heat transfer to the system. Other metals, such as gold, need a comparably large thickness to reach the percolation threshold, setting a lower limit for thin-film thickness at the insulator-to-metal transition, which generally makes them too conductive to match the necessary sheet resistance [110]. However, more recently, it has been shown that it is possible to fabricate ultrathin metal films (UTMF) of Ag [111] and Au [112] far below the classical percolation limit, using a surfactant layer of oxidized copper. This opens the possibility of deploying such a UTMF made of Ag or Au to act as an impedance-matched absorber for IR detection based on a nanomechanical resonator. The following section briefly introduces the theoretical concept behind impedance-matched absorption and its implementation to NAM-IR spectroscopy.

4.2 Theory of impedance matched absorption

The model of impedance-matching absorption [98, 99, 100] is based on the assumption that the refractive index n and extinction coefficient κ of the metal are to be equal. To get a better understanding of when this assumption is valid, the Drude model is used and rewritten in terms of plasma frequency ω_p and electrical resistivity ρ:

$$\hat{\varepsilon} = \varepsilon_1 + \mathrm{i}\varepsilon_2 = 1 - \frac{1}{\omega^2/\omega_\mathrm{p}^2 + \mathrm{i}\varepsilon_0\,\rho\,\omega}\,, \tag{4.1}$$

where ω is the angular frequency of the optical field. The refractive index and extinction coefficient is then given by $n = \sqrt{|\hat{\varepsilon}| + \varepsilon_1}$ and $\kappa = \sqrt{|\hat{\varepsilon}| - \varepsilon_1}$, respectively. In order for the assumption ($n = k$) to be valid, the imaginary part of the relative permittivity ε_2 must dominate. This is true when

$$\omega \ll \varepsilon_0 \, \rho \, \omega_\mathrm{p}^2 \, . \tag{4.2}$$

In this regime, the Drude model can then be simplified to

$$\hat{\varepsilon} \approx \frac{1}{\varepsilon_0^2 \, \rho^2 \, \omega_\mathrm{p}^2} + \mathrm{i} \frac{1}{\varepsilon_0 \rho \, \omega} \, , \tag{4.3}$$

where it can be seen that the real part is limited to some finite value, whereas the imaginary part is increasing for longer wavelengths. For gold, assuming bulk values $\rho = 2.2 \times 10^{-8}\,\Omega\cdot\mathrm{m}$ and $\omega_\mathrm{p} = 2\pi \cdot 2.1\,\mathrm{PHz}$, this limit is approximately at a wavelength of 56 µm. Below this limit, it should not be possible to achieve high absorptivity unless the material parameters change such that the physical condition is met, which is indeed the case for UTMFs [110]. Especially regarding electrical properties, the resistivity can be many factors of magnitude higher than compared to bulk [113, 114, 115]. To a certain extent, this can be described by the so-called scattering hypothesis; whereby the materials' resistivity is defined as a sum of scattering contributions [116]

$$\rho = \rho_0 + \rho_\mathrm{GB} + \rho_\mathrm{SS} + \rho_\mathrm{SR} \, , \tag{4.4}$$

where ρ_0 is the bulk resistivity, $\rho_\mathrm{GB} \propto D^{-1}$ is the grain-boundary contribution, $\rho_\mathrm{SS} \propto d^{-1}$ is the surface scattering contribution, and $\rho_\mathrm{SR} \propto d^{-3}$ is the roughness contribution. Here, d is the metal thickness, and D is the mean grain width of the metal film. For thin films, one can approximate D to be equal to d [115]. However, with increasing thickness, a limiting grain size of D_∞ is reached. The grain-boundary contribution can therefore be extended to $\rho_\mathrm{GB} \propto 1/D_\infty + 1/(Cd)$, where D_∞ is often found to be limited up to ~20 nm, respectively the range of the materials' electron mean free path. The dimensionless factor C typically ranges from 0.5 to 1 [115]. Below percolation, ohmic bridges and tunneling effects govern the resistivity, which can be described by e.g. Monte-Carlo simulations or the filamentary vibron quantum percolation model [117, 118], but however, are beyond the scope of this thesis. Collectively, all these resistivity contributions lead to broadening the absorptivity bandwidth of thin films down to shorter wavelengths, as described by Equation 4.2. Thereby, for a UTMF matching half the free space impedance, it is possible to provide an absorption coefficient of up to 50 % down to the near IR range.

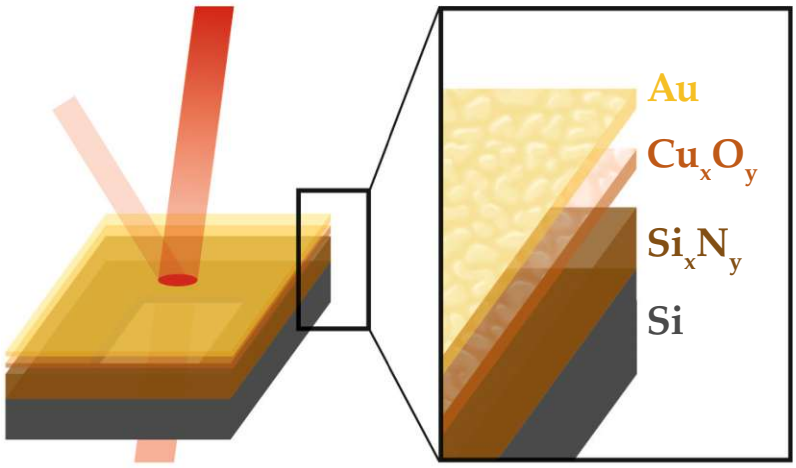

Fig. 4.1: Illustration of the fabricated layers and probing direction. The samples are based on 50 nm Si_xN_y membranes comprising an initially 1.2(2) nm sputtered and further naturally oxidized copper layer. To characterize optimal thickness, varying Au layers were deposited on top using standard physical vapor deposition. Figure and caption adapted from [7], copyright 2023 under a CC BY 4.0 license.

4.3 Fabrication of ultrathin gold layers

Figure 4.1 shows a schematic illustration of a UTMF fabricated on the surface of a Si_xN_y resonator. To enable the optical characterization of the UTMF by classical transmission FTIR spectroscopy, the experiments were performed on 2.5x2.5 mm squared membranes fabricated with the same protocol as described in Section 3.1. For the ultrathin gold fabrication, a Cu layer was deposited by sputter deposition using a Von Ardenne LS 730 S. The deposition rate was set to 1.5 $\text{Å}\,\text{s}^{-1}$, extrapolated from several test depositions. An initial Cu thickness of 1.2(2) nm was deposited for all samples used in the following characterization. To ensure a smooth and clean surface, the Si_xN_y membranes were plasma cleaned using Argon-based reactive ion etching in the same vacuum chamber immediately before Cu deposition.

Following Maniyara et al. [112], the samples were stored in ambient air for one day to undergo oxidation. During this process, oxidization of Cu can lead to a volume increase up to 68 % (assuming formation of Cu_2O [112]). Thus, the resulting seed layer thickness is expected to be slightly larger than the initial deposited film. In a final step, gold was evaporated from a tungsten boat with a deposition rate of 0.3 $\text{Å}\,\text{s}^{-1}$ at 3×10^{-8} mbar. The deposition rate and extracted nominal thickness were continuously monitored by a quartz resonating sensor. The thin-film morphology was analyzed by means of atomic force microscope images of the 2 nm Au layer (where percolation is expected) and the bare Si_xN_y .

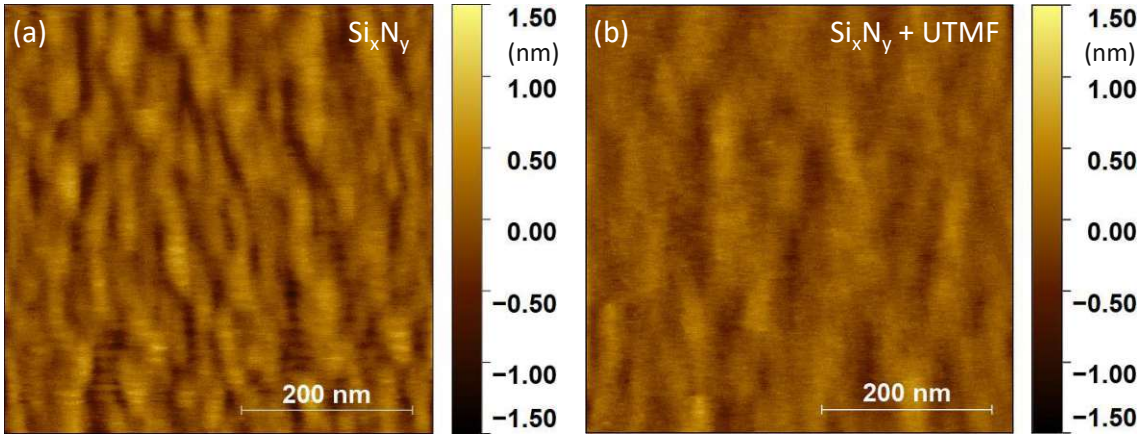

Fig. 4.2: AFM analysis of (a) the bare Si_xN_y resonator and (b) the resonator with a 2 nm thin Au layer. The comparison shows, that the surface of the Au UTMF indicates a smooth and continuous metal layer. Figure and caption adapted from [7], copyright 2023 under a CC BY 4.0 license.

As can be observed from Figure 4.2, the comparison of the surface topology indicates that a gold thickness of only 2 nm resembles a closed continuous metallic film with a slightly reduced roughness than the underlying Si_xN_y .

4.4 Results and discussion for UTMF impedance-matched absorption

To study and find the optimal UTMF, different Au thicknesses were deposited on individual Si_xN_y membranes from the same batch with the same pre-seeded Cu_2O layer. The following section shows the resulting electrical and optical properties to determine the appropriate thickness to enable impedance-matched absorption.

4.4.1 Analysis of sheet resistance

The sheet resistance of each UTMF was analyzed by a homemade *Van der Pauw* four-point probe method. In this technique, four evenly spaced electrical contacts are placed on the material's surface. A known current is passed between two contacts, while the voltage is measured between the other two. In this configuration, additional resistances of the probe system, such as contact- or wire resistance, are compensated. An average sheet resistance can be calculated by analyzing the voltage and current measurements and knowing the geometry of the probe configuration. This method is particularly useful for characterizing thin films and ensuring their quality in various electronic and semiconductor applications. In a common *Van der Pauw* measurement,

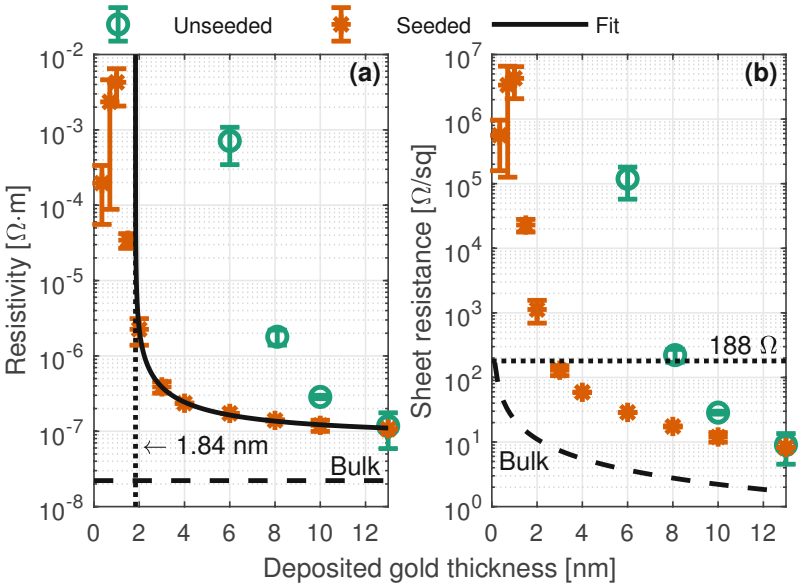

Fig. 4.3: Electrical properties of UTMFs. (a) Measured resistivity of seeded and unseeded Au layers as a function of deposited thickness. Due to the oxidized copper seed layer, a metallic behavior of Au can be obtained down to 2 nm. The resistivity can be well described by the scattering hypothesis Equation 4.4 and is strongly governed by grain-boundary and surface scattering $\propto d^{-1}$. To fit the data, a 1.84 nm offset is included to compensate for the percolation threshold and uncertainty of effective thickness. (b) Resulting sheet resistance of the same samples. Thus, the optimal thickness for an impedance-match of 188 Ω is expected around 2.5 nm. Bulk gold data taken from [119]. Error bars represent the standard deviation obtained from 10 measurements on each sample. Figure and caption adapted from [7], copyright 2023 under a CC BY 4.0 license.

typically, a cloverleaf-shaped geometry of the metal layer is needed. However, due to the comparably small chip size containing the membrane, the setup's predefined cloverleaf geometry exceeded the chip's lateral dimension. Therefore, a specialized homemade setup from the physical department at TU Wien was employed. The setup comprises cylindrical probe heads provided by 'Jandel', a 'Keithley 6221' current source, and a 'Keithley 2182A' nanovoltmeter. The probe head was attached to a load-bending beam, 'Burster 8511–5050', to monitor the contact force applied on the surface during the measurements. All samples were measured in a current range of 10×10^{-7} A to 10×10^{-3} A with a maximum contact force of 2.2 N to avoid scratching the metallic layer.

Figure 4.3 shows the measured resistivity and corresponding sheet resistance of seeded vs. unseeded gold as a function of the deposited layer thickness. Consistent with previous studies on ultrathin copper and gold films [113, 111, 120], the resistivity can be partly fitted by the scattering hypothesis Equation 4.4 including a variable offset to account for the percolation threshold and potential uncertainty of the effective film thickness. The data can be well described by the model Equation 4.4 down to about

2 nm, including a positive offset of 1.84 nm and is governed by the grain-boundary and surface scattering term $\propto d^{-1}$. The offset can be directly related to the percolation threshold. It is exactly between 1.5 nm to 2 nm where the resistivity drops below the insulator-to-metal transition value of around 6 µΩ·m, defined by *Ioffe-Regel* [121]. Thus, percolation must occur in between those samples. As can be seen, Au layers below 1.5 nm show an unexpected reverse trend of the resistivity with increasing thickness. This effect has previously been observed for UTMFs below percolation and can be related to the growth of islands and isolated atoms, which act as additional scattering centers [122, 123].

Compared to the bulk resistivity of Au with 2.2×10^{-8} Ω·m, the 13 nm thick layer converges to a three times higher value. As mentioned, the grain-boundary scattering term includes a limiting grain size factor of $1/D_\infty$, which significantly lifts the resistivity up to an equivalent thickness in the range of the electron mean free path ~20 nm. Thus, with respect to previous studies [115], such an increased value can be expected. Regarding the measured sheet resistance, the optimal thickness for matching with half the free space impedance to 188 Ω is expected around 2.5 nm Au.

To investigate whether there is a potential contribution of the oxidized copper used as a seed layer, additional experiments with varying Cu thicknesses revealed that bare Cu could also be used as an impedance-matched absorber but only if measured directly after deposition. However, due to oxidization over time [124, 111], all reference samples with oxidized copper showed a significant increase of resistivity back to the insulating state and consequential loss of absorptivity. In contrast, this is not the case for gold UTMFs which showed no change in optical or electrical properties over time. A comparison between seeded and unseeded membranes of this batch showed no significant dependence of the electrical or optical properties on the oxidized seed layer thickness.

4.4.2 Analysis of optical properties

All optical analysis was recorded via FTIR spectroscopy conducted on a Bruker Tensor 27. To minimize systematic deviations, transmittance and reflectivity measurements were performed within one measurement using a specified A 510/Q-T set-up. This accessory allows the acquisition of transmission and reflection with an incident angle of 15° on the same spot on the sample. To avoid the optical contribution of the silicon substrate, an aperture of 2 mm was used.

Optical data for the underlying resonator material was needed to obtain a proper fit for the transmittance and reflectivity of ultrathin Au. This was extracted from multiple FTIR measurements performed on bare Si_xN_y membranes, presented in Figure 4.4a.

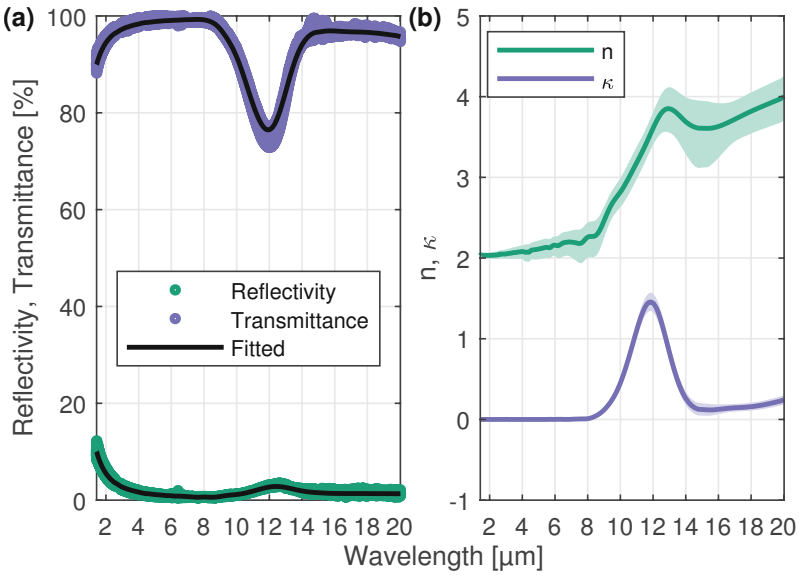

Fig. 4.4: Optical properties of the support layer. (a) Average of ten individual FTIR measurements on 50 nm silicon nitride membranes. (b) Fitted optical constants using a general matrix model [125] by grouping measured data into fixed wavelength points, from which the optical constants were estimated individually. The shaded region indicates the uncertainty estimated as a 50 % increase in the sum of squared residuals. Figure and caption adapted from [7], copyright 2023 under a CC BY 4.0 license.

Here, the drop of transmittance and slight increase of reflectivity between 9 µm to 12 µm is due to the major vibrational mode of Si_xN_y [55]. Using an optical model [125] adapted to a single Si_xN_y layer to predict the transmittance and reflectivity, a nonlinear fit was done at each wavelength separately to estimate the optical constants. To reduce the uncertainty of the fit, the measured data were grouped into spectral blocks with 50 % overlap. This increases the amount of data per spectral point at the cost of spectral resolution. The result is shown in Figure 4.4b with 618 spectral points. Notably, the fit is not *Kramers-Kronig* constrained [126], which was not possible due to the limited spectral range of the measurements. However, for the purpose of this study, the data and fitted n, k values were deemed acceptable.

Figure 4.5a shows the measured transmittance and reflectivity of all seeded gold layers. The data is fitted using the aforementioned optical model, combined with the Drude model from Equation 4.1, and including the previous extracted optical properties for Si_xN_y . As can be seen from the R^2 coefficient of determination, the thicker layers show a metallic behavior. They can be well fitted down to 2 nm, consistent with the percolation threshold obtained before. For those thicknesses, the extracted plasma frequency with $\omega_p \approx 2\pi \cdot 3.0(7)$ PHz is slightly increased compared to bulk but remains constant within its uncertainty.

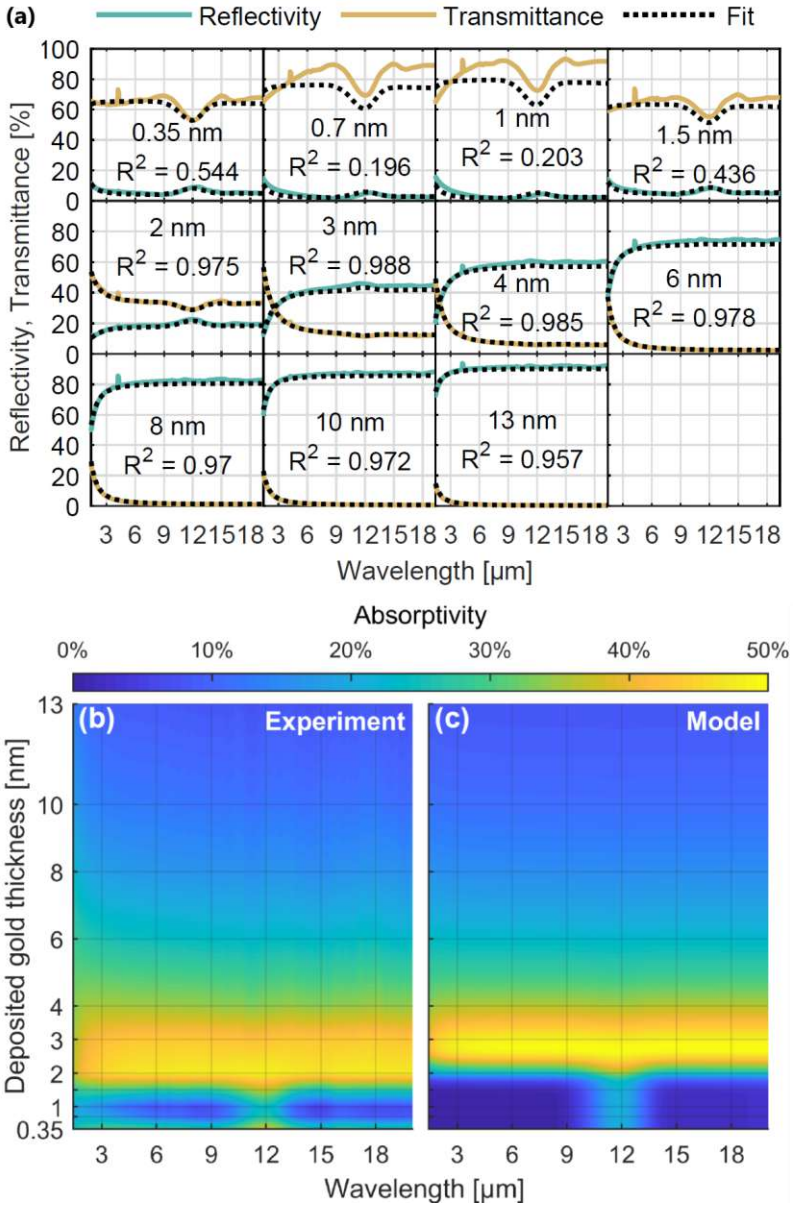

Fig. 4.5: Optical Properties of the UTMFs. (a) Measured transmittance and reflectivity of (seeded) Au layers obtained by FTIR spectroscopy. All spectra are fitted by the given Drude Model Equation 4.1, including the measured resistivity. R^2 is the coefficient of determination for each fit. As for thicker layers, all spectra are in good agreement with the optical properties of a metallic film, the layers below 2 nm show a divergence due to the insulator-to-metal transition. For the metallic-like layers, the obtained plasma frequency remains constant with $\omega_p \sim 2\pi \cdot 3.0(7)$ PHz. (b) Absorptivity as a function of deposited gold thickness and wavelength was obtained experimentally from FTIR measurements. The data has been linearly interpolated for the plot. Each horizontal grid line corresponds to a sample. All measured layers were evaporated on 50 nm Si_xN_y membranes comprising an oxidized copper seed layer. (c) Calculated absorptivity using the fitted Drude parameters and measured resistivity via Equation 4.3 and extracted optical properties of Si_xN_y . Figure and caption adapted from [7], copyright 2023 under a CC BY 4.0 license.

Due to the loss of metallic behavior, the model can not be effectively applied below percolation (2 nm), which can be clearly seen by the dropping R^2 coefficient. In this region, an increase of the transmittance from the 0.35 nm to the 0.7 nm and 1 nm sample can be observed. Previous studies on thin Au layers around the percolation threshold have confirmed this antireflection phenomenon [127], whose origin lies in the divergence of the dielectric constant ε_1 from the bulk value in that specific region [110]. Therefore, one could suggest using ultrathin Au below percolation as a potential antireflection coating.

Figure 4.5b shows the measured, linearly interpolated absorptivity (1 − reflectivity − transmittance), plotted over the wavelength and deposited Au thickness. One can clearly determine a maximum absorptivity of 40 % to 50 % between the 2 nm and 4 nm Au layer, with a slight decrease towards smaller wavelengths. The absorption peak with a maximum at 12 µm below a gold thickness of 2 nm can be attributed to the supporting Si_xN_y substrate, as can be seen in Figure 4.4. The slight increase in absorptivity for the thinnest Au layer of 0.35 nm could be related to the observed reverse trend of the resistivity as can be seen in Figure 4.3.

Figure 4.5c presents the corresponding calculated absorptivity based on the previously obtained optical properties of bare Si_xN_y and the relative permittivity (see Equation 4.3), comprising the measured resistivity and extracted plasma frequency. A comparison to the data shows a good agreement with a minimal offset of ~ 0.35 nm towards the optimal thickness, which lies in the uncertainty of the quartz sensor used as a reference during deposition. Concerning the derived criteria Equation 4.2, the increased resistivity and plasma frequency leads to an almost wavelength-independent high absorptivity, ranging from 2 µm up to the spectral detection limit of 20 µm of the FTIR. The absorptivity is expected to remain constant also in the far-IR (THz) regime. Regarding the long-term stability of the impedance-matched UTMF, subsequent measurements verified that the 2 nm samples showed no significant change in absorptivity over a period of five months being stored under ambient conditions. Investigations of similar Au thin films on oxidized Cu also showed a high stability [128].

4.4.3 Impact of UTMF to the mechanical properties

For deploying the UTMF as an absorber in a nanomechanical system, the additional layer should ideally not compromise the mechanical properties of the resonator. Therefore, the impact of the UTMF on the tensile stress and quality factor was analyzed. Figure 4.6 shows the effective tensile stress of 50 nm thin and 1 mm squared membrane resonators with varying UTMF layers of gold, obtained from the resonance frequency.

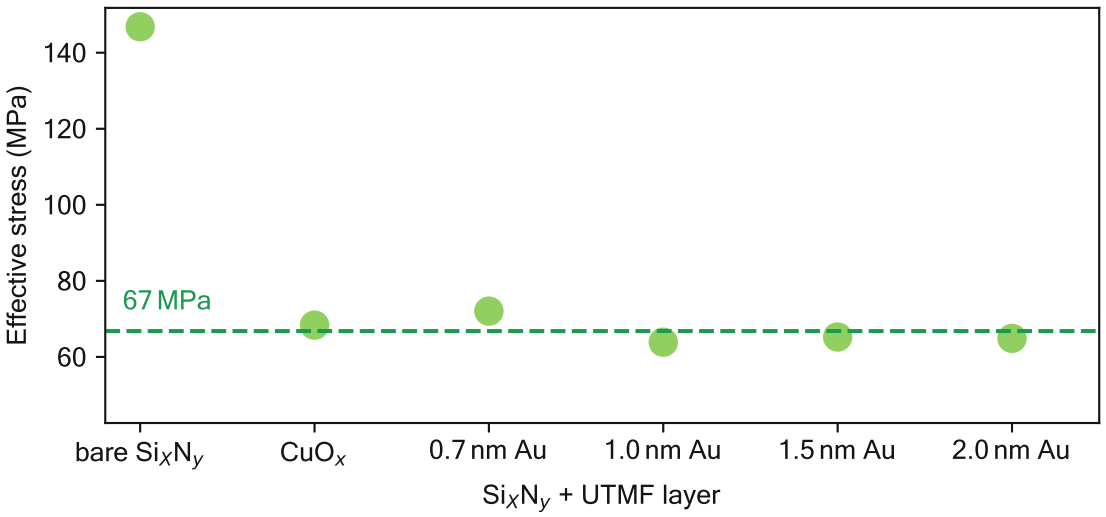

Fig. 4.6: Effective stress of a 50 nm thin and 1 mm squared Si_xN_y membrane featuring different UTMF layers. The initial treatment of sputtering a Cu seed layer is the major drive in reducing tensile stress. In contrast, the subsequent deposition of Au thin films does not change the tensile stress.

As can be observed, starting from the CuO_x seed layer, all resonators equipped with a UTMF show a significantly reduced tensile stress compared to the bare Si_xN_y . However, the major contribution to the effective stress change originates from the deposition of the seeded layer.

Considering the seed layer is added in a sputtering process followed by oxidation of the copper, such a reduction of tensile stress can be expected. Previous studies showed that using oxygen plasma with similar power as used for the deposition of the seed layer (100 W) leads to oxidization of the top 2 nm layer and, in the same fashion, reduce the tensile stress [52]. In contrast, adding a gold UTMF (which can not oxidize) to the seeded layer does not change the effective stress of the system.

Another parameter for assessing the performance is the mechanical damping of the system characterized by the quality factor. This is typically obtained by measuring a ring-down of the resonators' amplitude when switching off the actuation of the resonator. Due to the mechanical damping, the amplitude follows an exponential decay with the mechanical time constant $\tau_{mech} = Q/\pi f_0$ (see Equation 2.12). A detailed description and study on Si_xN_y resonators using this technique can be found by Saedghi et al. [4]. For the resonator with an optimized UTMF of 2 nm, a quality factor of 730,000 could be obtained, which is comparable to the Q factor of bare resonators.

4.5 Conclusion & outlook

The chapter presented the path to a suitable absorber for applying a nanomechanical resonator as a broad spectral IR detector. Combining the concept of impedance-matched absorption with the novel fabrication method of ultra-thin metal films enabled the implementation of an ultra-thin and highly efficient absorber. In good agreement with theoretical assumptions, it was possible to gain 47(3) % absorptivity over the entire MIR range from 2 µm to 20 µm. According to the theory, this wavelength-independent absorptivity is expected to be also valid in the far-IR (THz) domain, as demonstrated by previous studies [129].

Electrical and optical analysis of the fabricated layers demonstrated the significantly increased resistivity and impact on the optical properties of such ultrathin metal films, which broaden the lower limit of impedance-matched absorption to 2 µm. In this context, it was possible to approximately match the optimal sheet resistance of 188 Ω. The extracted dielectric functions verified that for those samples, the imaginary part of the relative permittivity is strongly enhanced compared to the real part, which in this region can be almost neglected. Comprising a small offset of the layer thickness, the calculated absorptivity is in good agreement with the experimental results.

Analyses of the tensile stress and Q factor before and after deposition of the absorber show no negative impact on the mechanical properties of the resonator.

Besides the enhanced absorptance, the impedance-matched absorber affects several parameters concerning the sensitivity. The application of a metallic absorber increases heat transfer by thermal conductance and emissivity (see Equation 2.9), which both reduce the power responsivity. Furthermore, the increased absorptivity makes the resonator more sensitive to the intensity noise of the probing light source. This can be a particular issue when implementing an optical readout of the resonance frequency. Thus, an uncoated area for the probing laser should be considered when using the UTMF-enhanced resonator with an optical transduction scheme. Consequently, these effects reduce the sensitivity.

To fully gain from the absorptance of the impedance-matched absorber, the resonator size should be kept below the radiation-dominated regime (see Figure 2.3) with $\mathscr{R}_P \propto \alpha_{abs}(\lambda)/G_{cond}$. Including the average absorptance of the UTMF compared to Si_xN_y , and the increased thermal conductance, the absorber will boost the power responsivity by one order of magnitude. Furthermore, this can be addressed by reducing the absorber area to the IR beam size, as demonstrated in Piller et al. [1].

In the course of this study, several other metals and composite alloys have been investigated for implementation as impedance-matched absorber. Among them, chromium, titanium, titanium-nitride, and platinum were tested. Although the Au-UTMF represents the state-of-the-art solution for a nanomechanical resonator as an IR detector, the ease of depositing a 5 nm platinum thin film without the need for a seed layer has proven to be a suited and effective alternative (see [5, 6]).
This has pushed the sensitivity for NEMS-IR detection based on trampoline-shaped resonators to a NEP of 7 $pW/\sqrt{Hz}$, approaching the theoretical photothermal limit of detection at room-temperature [6]. Due to the impedance-matched absorber, this sensitivity is linear over the entire spectral range of 2 µm to 20 µm. However, in some cases, the platinum layer peeled off during the fabrication of germanium nanowires for bolometry [5]. In contrast, a chromium thin film of about 7 nm also enables impedance-matched absorption while maintaining excellent adhesion to the Si_xN_y substrate. However, compared to the UTMF or platinum, chromium drastically increases the tensile stress, reducing the resonator's power responsivity.

5 Setup development and characterization for NEMS-IR spectroscopy

This chapter delves into the technical evolution of a proof-of-concept device, transitioning it into a fully integrated system for NEMS-IR spectroscopy with *in situ* desorption capabilities.
Initially, attention is directed toward the development and characterization of an aerosol sampling setup. Subsequently, this setup is integrated into a compact vacuum chamber, enabling *in situ* aerosol sampling and NEMS-IR spectroscopy. The system is tested with single compounds and solvents to validate its functionality. Following this, a dedicated section explores the optimization of resonator geometry, seeking to find a balance between high sensitivity and enhanced sampling efficiency. Finally, the system is successfully merged with a commercial FTIR, thereby enabling NEMS-FTIR spectroscopy.
The occurrence of frequency drifts, resulting from temperature changes or desorbing analytes in a vacuum, motivated the development of a novel setup. Compared to its predecessor, this iteration features an enhanced contact mechanism, atmospheric compensation, and integrated temperature control. In the concluding section, the potential of temperature control for desorption and adsorption analysis is demonstrated.

5.1 Development and characterization of an aerosol sampling setup

In pursuit of developing a system capable of analyzing low-abundance analytes while ensuring high efficiency and minimal sample loss, various sampling techniques have been explored. Among these, aerosol-based sampling has proven to be a promising method for NAM-IR spectroscopy [56, 57]. In this approach, the liquid analyte is nebulized or atomized and subsequently dried into particles for sampling on a resonator via inertial impaction. This involves streaming the aerosol through openings in a suspended or perforated resonator.
Alternatively, analytes can be drop- or spin-casted. However, this often results in a coffee-ring effect or distribution across the entire surface. By integrating an optimized perforation pattern into the resonator design, aerosol-based sampling offers the advantage of concentrating the analyte onto a specific area of the resonator's surface (see Section 5.2.2). Despite the phase transition from liquid to solid, which may cause sample loss, aerosol-based sampling remains a viable solution.

Setup development. Figure 5.1 shows a schematic of the sampling setup developed and used throughout this thesis. Inspired by the previous work of Kurek et al. [57], the system is based on a self-aspirating jet nebulizer (ESI - MicroFlow PFA-ST) connected to a cyclonic spray chamber (Meinhard ML148030). The spray chamber functions as a cut-off filter for larger droplets >1 µm which is followed by a diffusion dryer (TOPAS) to remove the liquid fraction. In a homemade sampling chamber, the perforated resonator is sealed between two O-rings pushed on the chip by a magnetic holder. The aerosol flow is generated by a cost-effective membrane pump (Schwarzer Precision) and set to 1 L min^{-1} by a ball float flow meter.

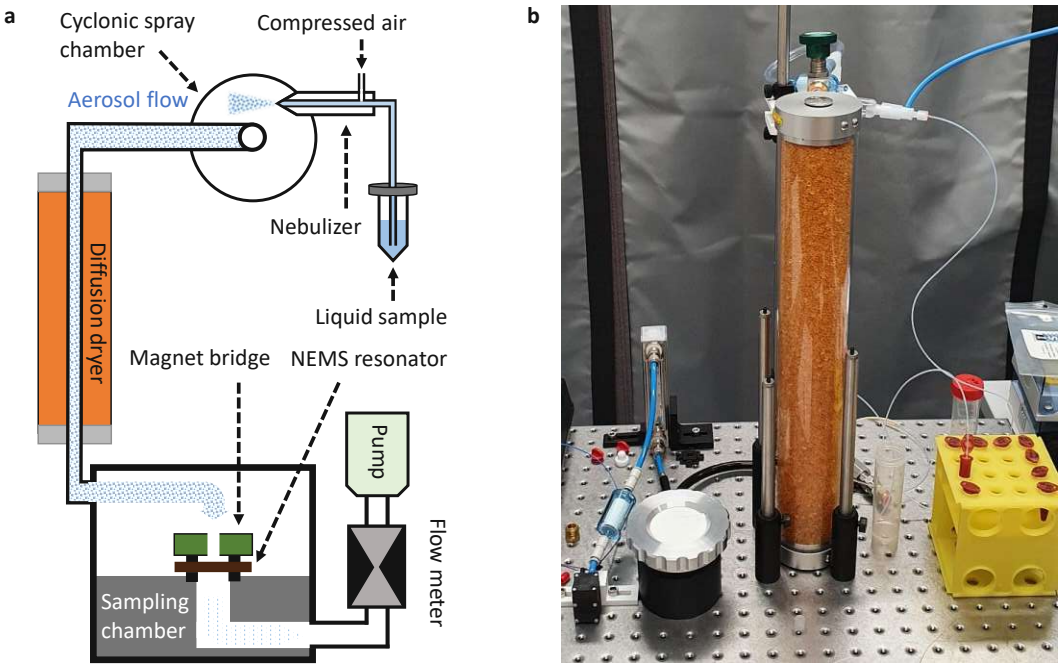

Fig. 5.1: Homemade aerosol sampling setup for liquid analytes. (a) Schematic illustration of the main components and (b) picture of the first setup version comprising a dedicated sampling chamber. Figure adapted from VII.[7].

Characterization of sampling parameters. For low analyte concentrations, a larger droplet size is preferred to augment the particle size of the dried aerosol. However, large droplets might not sufficiently dry into a solid particle when passing the diffusion dryer, which affects the sampling efficiency. Therefore, the system was tested with solutions made of sodium chloride (NaCl) with varying concentrations and liquid uptake rates of the nebulizer. In addition to the liquid uptake rate and ideal concentration, the sampling setup was tested for different gas pressures and aerosol flow rates.

The characterization and optimization of sampling parameters was part of a supervised Bachelor thesis conducted by K. Waltenberger [130]. In this work, an optimal concen-

tration range for aerosol sampling was obtained for $10\,\mu g\,mL^{-1}$ to $1000\,\mu g\,mL^{-1}$. With the focus set to sample low abundant analytes, the following efficiency analysis was performed with an NaCl concentration of $100\,\mu g\,mL^{-1}$. Assuming a spherical droplet with a diameter of $1\,\mu m$ of this solution and NaCl density of $2160\,kg\,m^{-3}$, the dried aerosol has an approximate particle diameter of $\sim 36\,nm$.

Figure 5.2 shows the sampling efficiency of NaCl solution on single Si_xN_y string resonators as a function of the resonator width, liquid uptake rate and gas pressure. According to impaction-based sampling theory by W. Hinds [79] (see Equation 2.32), the single-fiber collection efficiency drops for an increasing fiber width ($E_c \propto u/d_f$). This can be observed in Figure 5.2a by the decreased efficiency with increasing string width across all self-aspiration capillaries.

The results presented in Figure 5.2a show, that the self-aspiration capillary with the lowest uptake rate provides the highest sampling efficiency. The reduced loss of larger droplets in the cyclonic spray chamber can be attributed to the smaller droplet size resulting from the decreased nebulized liquid volume.

In contrast, Figure 5.2b indicates an improved efficiency for the use of smaller gas pressure at the nebulizer, which, due to the *venturi effect*, leads to an increase of the liquid uptake rate. Combining both parameters, one can conclude that a low uptake rate is generally beneficial, while the gas pressure can be used to fine-tune the rate for a trade-off in droplet size and sample loss at the spray chamber. For a detailed examination of this relationship, the reader is referred to the study conducted by Novak et al. [131].

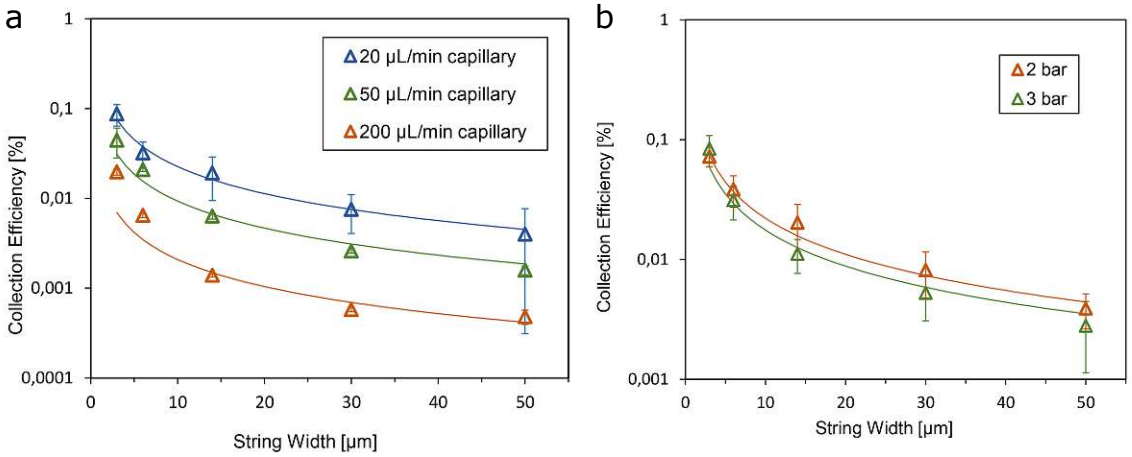

Fig. 5.2: Sampling efficiency of single Si_xN_y string resonators for different operating parameters. (a) Consistent with the sampling theory, thinner strings show a higher single-fiber capture efficiency. The lowest uptake rate resulted in the highest sampling efficiency. (b) The comparison of two operating pressures shows that a smaller pressure benefits the sampling efficiency. Image courtesy by K. Waltenberger [130]

Outlook. Throughout this work, the aerosol sampling setup was continuously improved. A notable and recent advancement involved upgrading the pneumatic nebulizer to the Meinhard CytoNeb model and incorporating a specialized spray chamber, known as the 'Meinhard CytoSpray'.

Figure 5.3 illustrates a schematic depiction of the enhanced sampling setup, featuring the 'CytoNeb' nebulizer, 'CytoSpray' chamber, and a syringe pump for precise liquid sampling volume control [132]. Unlike the cyclonic spray chamber, this device primarily eliminates the largest droplets at the periphery of the spray cone. For a comprehensive examination of droplet distribution within a spray cone, refer to Kahen et al. [133].

Furthermore, the cyto-spray chamber facilitates an additional laminar sheet flow to mitigate wall losses and promptly desiccate the nebulized droplets. Through the combination of its design and additional sheet flow, this spray chamber achieves a theoretical aerosol transport efficiency of up to 90 %. The integration of this setup and the development of a dedicated microfluidic injection system was part of a recent supervised bachelor thesis conducted by D. Stadlmann [132]. Initial experimental findings suggest a notable enhancement of the sampling efficiency up to 60 % for particles with a diameter of 1 µm.

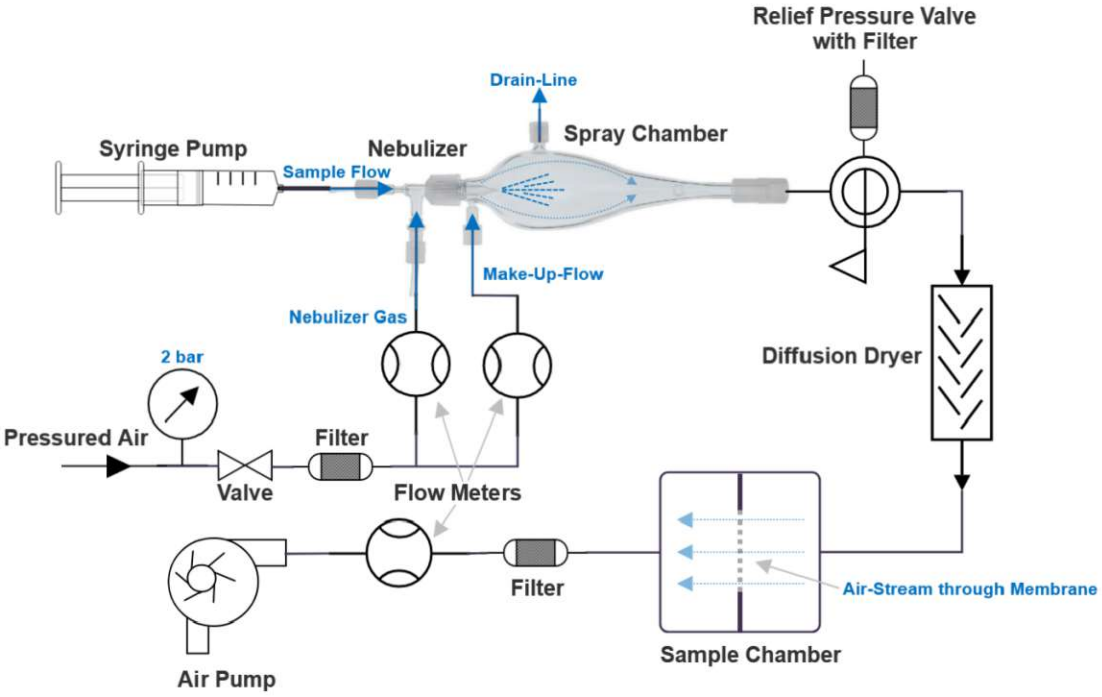

Fig. 5.3: Schematic draft of the recently improved aerosol sampling setup. The upgraded system comprises a specialized nebulizer, spray chamber, and syringe pump for a defined and constant liquid sampling volume. Image courtesy by D. Stadlmann [132].

In addition to the advancements in aerosol generation, significant enhancements were made to the sampling chamber. The initial version of the chamber and magnetic chip holder utilized Teflon and 3D-printed polylactic acid (PLA). These materials tend to accumulate charge, which reduces the sampling efficiency of the typically charged aerosol. Furthermore, the sample holder induced a vortex-like effect on the resonator, as can be observed from the caffeine-sampled chip depicted in Figure 5.4a. This was caused by the aerosol entering from the side into the orifice of the sample holder.

The accumulation of charge on PLA and the induced vortex effect contributed to the loss of analyte during sampling and led to an uneven distribution of analyte across the chip. To address these issues, a compact sampling chamber constructed from aluminum was developed as part of a supervised bachelor thesis conducted by C. Leuschner [134]. In contrast to the previous Teflon-based chamber, the aerosol flow now directly enters the resonator from the chamber lid. Figure 5.4b presents an example of a resonator sampled in the upgraded aluminum chamber. A direct comparison with the previously sampled resonator reveals a more uniform analyte distribution with the improved chamber design.

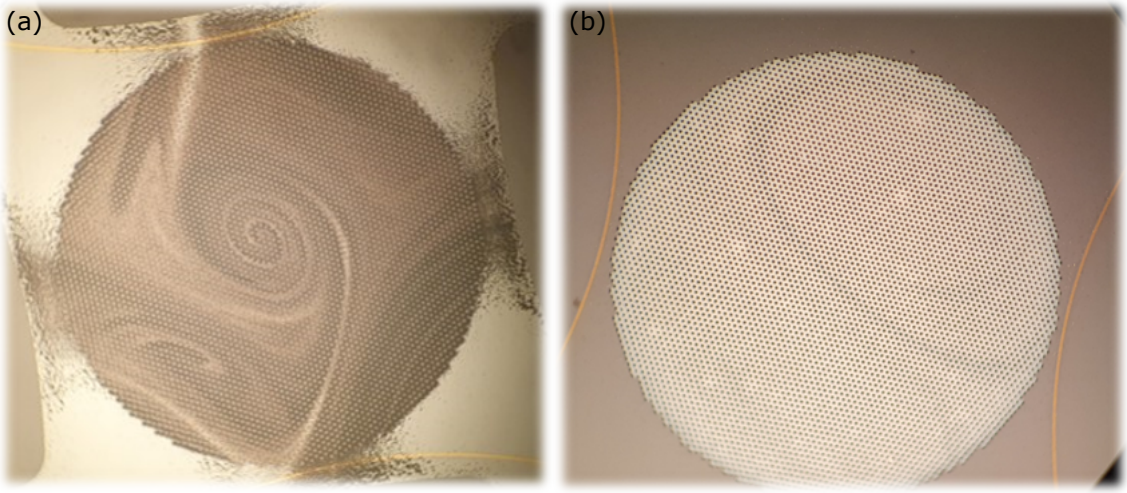

Fig. 5.4: (a) Micrograph showing the inhomogeneous distribution of the analyte due to vortex formation of the aerosol flow direction in the old sampling chamber. (b) Example of a homogeneous sampled chip using the improved aluminum-based sampling chamber.

5.2 NEMS-IR spectroscopy setup with integrated sampling

With a focus on a multipurpose analytical device, the setup should ideally provide an integrated transduction of the resonator, as well as the ability to perform *in situ* sampling. In addition, it should include a mechanism for easy and quick exchange of a chip comprising the resonator.

Implementation of transduction. Despite the reduced sensitivity, implementing an electrodynamic transduction scheme eliminates the necessity for optical re-alignment for each new chip and presents a practical and cost-effective solution. Therefore, the resonators were equipped with two parabolic-shaped 5 µm wide electrode traces along the perimeter of the maximum displacement of the 2,1 / 1,2 mode. In this fashion, one electrode can be used to drive and the other to detect the resonator's motion in a PLL configuration without considerable cross-talk. Figure 5.5a shows a micrograph of the two golden electrodes along the edge of a perforated trampoline resonator. The metal thickness was chosen as a trade-off between additional heat transfer reducing the power responsivity and small electrical resistance to gain a high S/N of the transduction scheme (see Section 2.3). The average resistance of the transduction electrodes was ≈100 Ω.

Fast electrical connection. For connecting the electrodes to the readout electronics, an electrical contact bridge with four spring-loaded probes (Fixtest 707.05.05H20.045) was designed. The bridge comprises a metallic screw on each side attracted by the same magnets used for providing the perpendicular magnetic field for transduction. This way, the spring-loaded probes are automatically centered and pushed on the outer contact pads on the resonator chip, as indicated by the orange dots in Figure 5.5b. The developed contact bridge enables the direct use of a resonator 'out-of-the-box' from the clean room, eliminating the need for any preparation, such as wire bonding or integration to a printed circuit board (PCB).

Figure 5.6 shows a schematic illustration of the NEMS-IR spectroscopy setup featuring *in situ* aerosol sampling. To enable the electrodynamic transduction scheme, the aluminum housing incorporates several neodymium magnets. Configured in a Halbach-array, this arrangement provides a constant and homogeneous magnetic field of approximately 0.8 T at the resonator.

Implementation of aerosol sampling. To integrate the aerosol sampling, the vacuum chamber features two membrane valves connected to the sampling system. The generated aerosol, coming from the diffusion dryer, enters through the top valve and is pulled through the perforation of the resonator by a pump connected to the bottom valve. The resonator chip is placed on an O-ring in a dedicated, micro-machined groove.

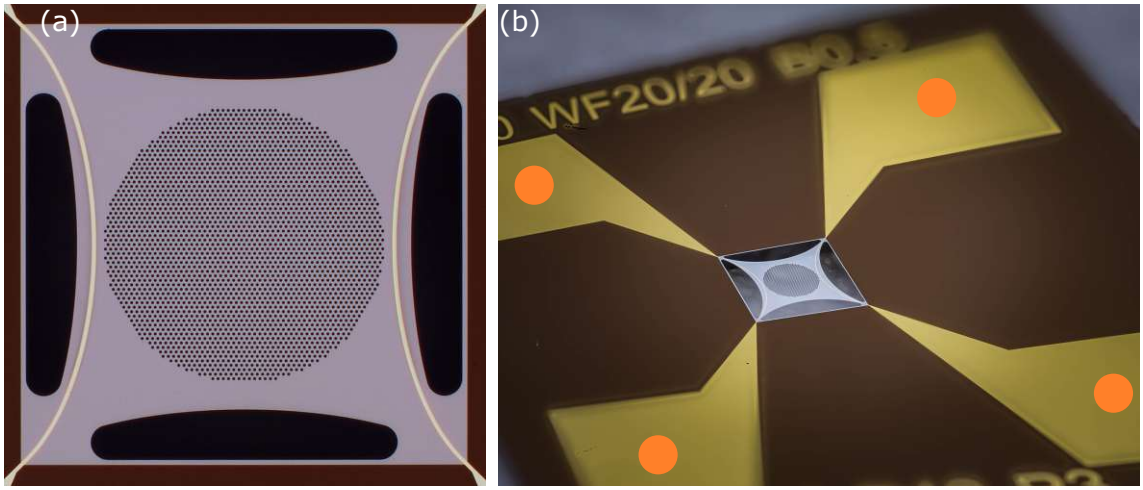

Fig. 5.5: Micrograph of trampoline resonators featuring electrodes for electrodynamical transduction. (a) Close-up picture of the resonator with the electrode located along the resonator perimeter, and (b) a picture of the entire resonator chip highlighting the connection points to the contact pads. Image courtesy by Pfusterschmid, G.

In addition to providing the electrical contact, the spring-loaded probes push the chip to the O-ring to ensure the aerosol flow is guided through the resonator only.

Implementation of IR light source. Throughout most of the studies presented in this work, a quantum cascade laser (MIRCat - Daylight Solutions) with a spectral range of 1779 cm^{-1} to 1122 cm^{-1} / 5.6 µm to 8.9 µm was used. The IR beam is focused on the central area of the resonator by a parabolic mirror (Thorlabs MPD169-M01, RFL=6”). The mirror is placed on a linear XYZ-stage and focuses the beam through a wedged and anti-reflection coated window made of Zinc Selenide (Thorlabs WG71050-E4). In the first iteration of the setup, the scanning wavenumber of the laser had to be manually adjusted to the frequency change of the resonator measured using a Python script. As part of a supervised bachelor thesis conducted by R. Pliesnig [135], an extensive multi-threaded interface (GUI) based on Python was developed. The interface facilitates simultaneous control over the laser and lock-in amplifier, used for frequency tracking. Consequently, the GUI enables fully automated spectra acquisition and grants the ability to operate the laser in either step scan or sweep mode, with defined step times or sweep velocity.

Figure 5.7 shows a picture of the entire system with the connected aerosol sampling setup, light source and a close-up of the acquisition chamber. The chamber made of aluminum, comprising the features for the magnet Hallbach-array, chip groove, etc., was designed in CAD software and fabricated by a CNC manufacturer (Weerg.com).

To ensure the magnets stay in place and give guidance for the contact bridge, a 3D-printed cover included a contraption/notch for the contact bridge. The sockets for the

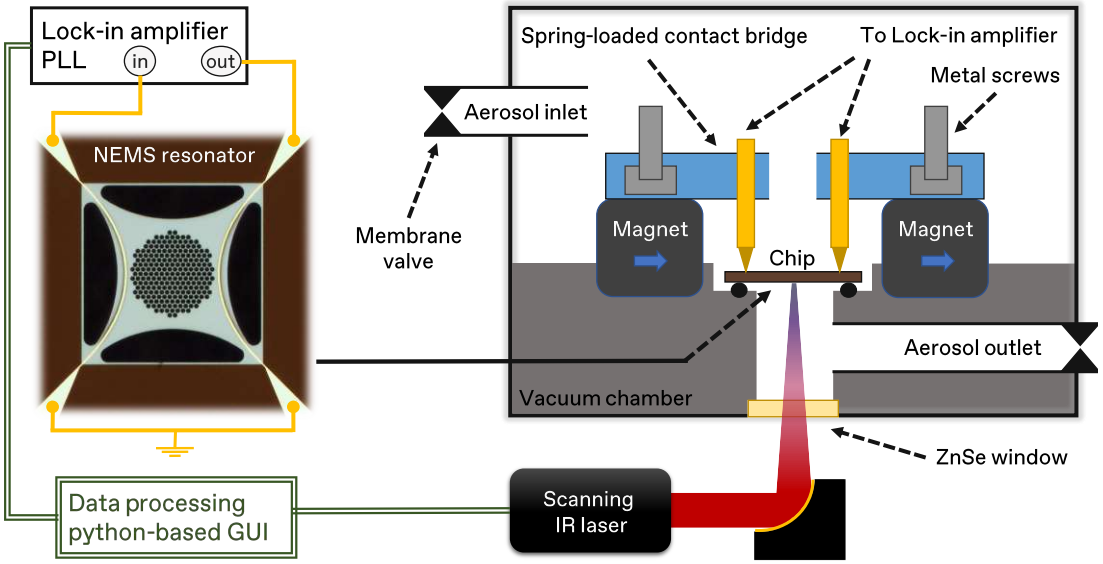

Fig. 5.6: Schematic illustration of the setup for acquisition and *in situ* aerosol sampling. At the core, the developed system comprises a vacuum chamber with several engineered ports for the aerosol sampling setup, a ZnSe window for the IR light, a HALLBACH-array of magnets for the transduction, and a contact bridge for fast chip exchange. A homemade Python-based interface enables automated spectra acquisition.

spring-loaded contacts were drilled by a 0.9 mm drill into the 3D-printed PLA using a micro-CNC milling machine in-house. The metal screws were pushed into pre-defined printed sockets. The electrical connection of the spring-loaded probes of the contact bridge to the lock-in amplifier was made by soldered cables to a vacuum-proof USB port.

Typically, for commercial vacuum systems a specific polishing at the flanges is added to guarantee no leaking. Moreover, one has to consider a potential outgassing of the 3D-printed PLA. Therefore, the system was initially tested with a molecular turbo-pump where a decent final pressure of 5×10^{-6} mbar could be reached. However, to enable a fast venting and evacuation for chip exchange, the setup was operated with a rotary-vane pump (Pfeiffer Model DUO3M) with a nominal pressure of 5×10^{-3} mbar.

5.2.1 Characterization for NEMS-IR spectroscopy with single compounds

Characterization of the QCL power spectrum. In the first experiment, the power profile of the laser is characterized. The homemade GUI allows two different acquisition modes: 'sweep' with a defined continuous change of the wavenumber per second, and a 'step scan' with defined dwelling times. Figure 5.8 presents the default average power spectrum of both QCL modules provided by DAYLIGHT SOLUTIONS, and below,

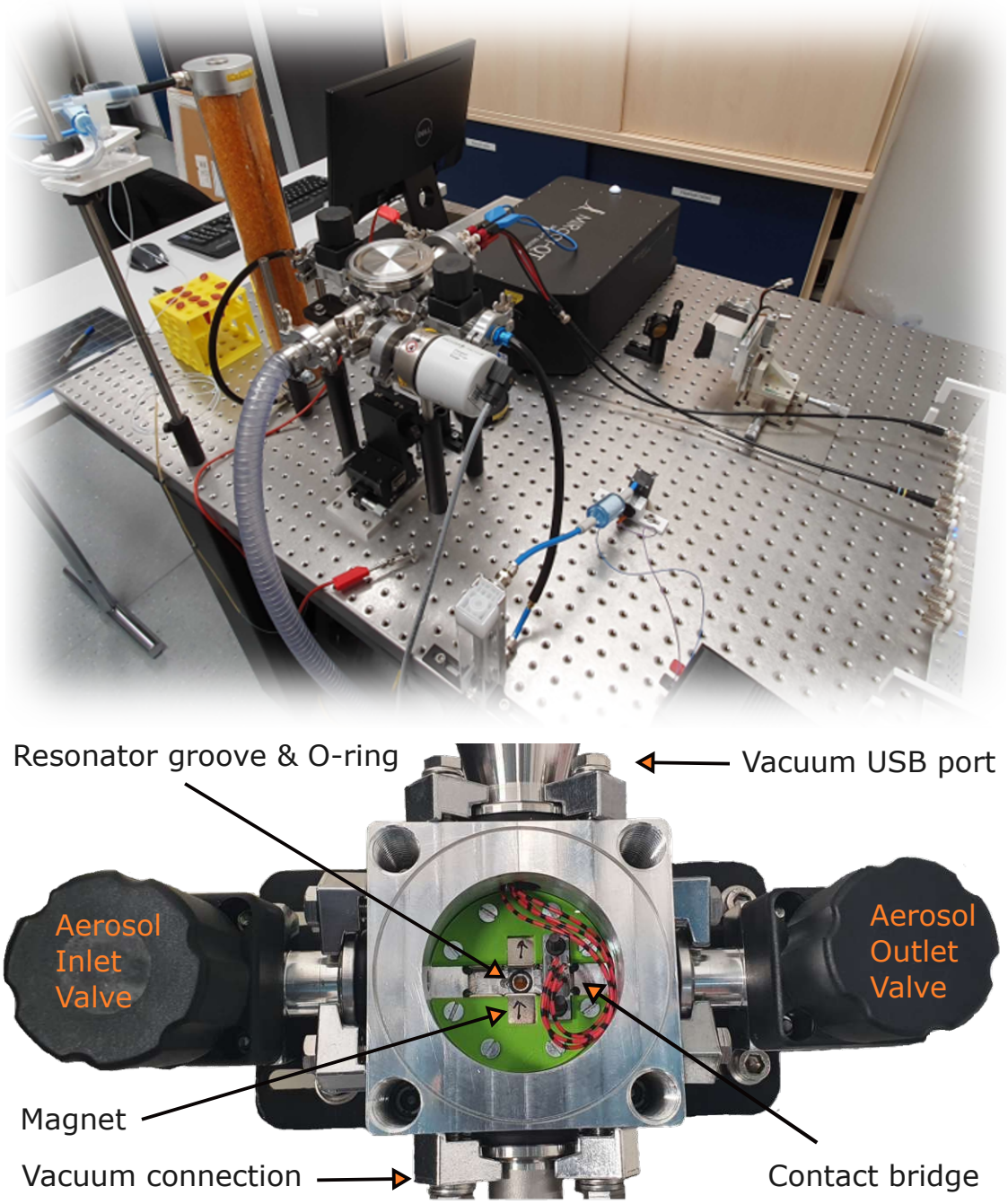

Fig. 5.7: (top) Picture of the operating NEMS-IR setup including QCL light source and the aerosol sampling setup and (bottom) close-up picture of the acquisition vacuum chamber highlighting the main inner components described in the schematic illustration Figure 5.6.

the spectrum recorded by a resonator using a step scan mode with a resolution of $1\,\mathrm{cm}^{-1}$. Generally, the spectrum obtained shows the main shape and features provided by the manufacturer. The QCL power was reduced by a factor of 100 using a neutral density filter in the optical path before the parabolic mirror. Hitting the edge of

Si_xN_y 's vibrational mode towards lower wavenumbers (see Figure 4.4), the continuously increasing absorption of Si_xN_y leads to a distortion of the power profile. The strong spectral features in the lower wavenumber range of the spectrum are caused by the typical atmospheric rotational vibration modes of gaseous H_2O (see Figure 3.5).

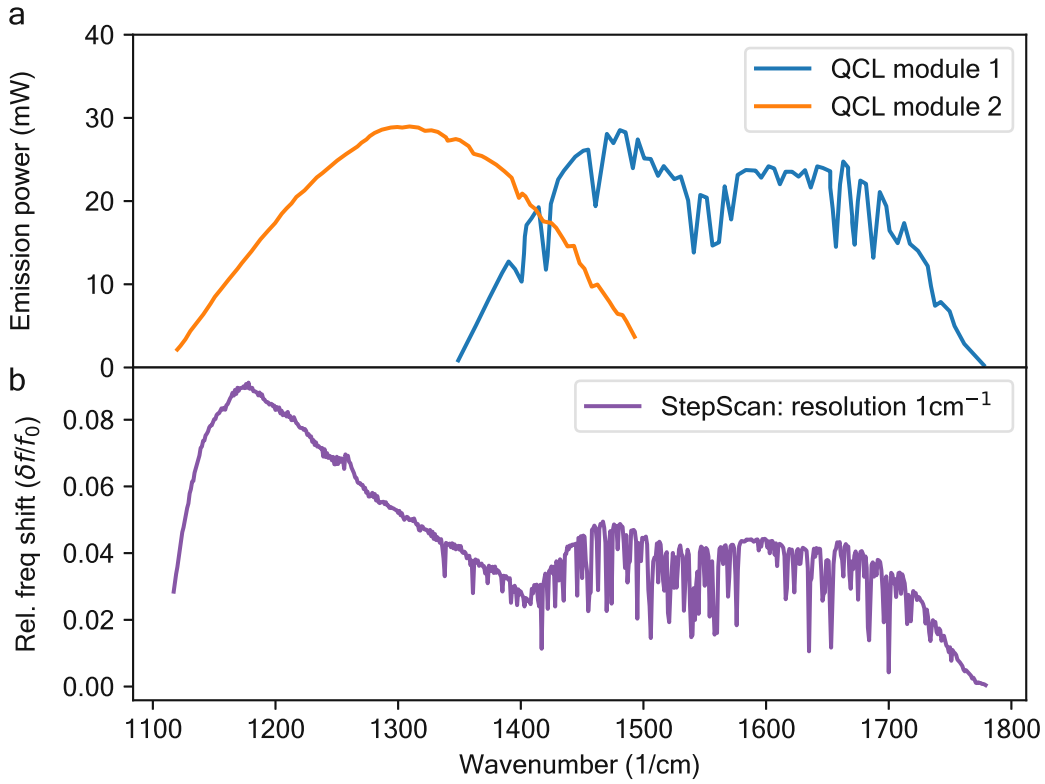

Fig. 5.8: Comparison of QCL power spectrum for (a) default settings (duty cycle 5 %) provided by Daylight Solutions and (b) recorded in the NEMS-IR setup by a Si_xN_y trampoline-shaped resonator using a step scan mode. For the acquisition, a neutral density filter was used to reduce the incident light intensity on the resonator.

The presence of water vapor in the beam path reduces the available power that reaches the resonator. In both acquisition modes, the QCL allows a continuous transition between both modules, which can be seen by a kink in the spectrum near 1400 cm.

Step scan versus continuous sweep. As mentioned above, the QCL and developed GUI allow operation in two spectral acquisition modes. The step scan provides the best relative frequency response values to the probing wavenumber due to the immediate acquisition of the resonance frequency before and during light emission. This compensates for any thermal-related drifts of the resonator frequency during the measurement.

However, a high-resolution step scan with a dwell time of (on/off) 0.5 s, a measurement as presented in Figure 5.8 needs a total acquisition time of about 11 min. Furthermore, operating the system with a PLL frequency tracking scheme, the lock-in amplifier often loses the lock of the resonance frequency for larger sudden jumps, making the spectra acquisition a tedious process. In contrast, the sweep mode provides a fast and continuous acquisition.

Concerning the average thermal relaxation time of the resonator of about 25 ms, obtained from fitting the frequency change upon emission (see III.[3]), with a scanning speed up to 40 cm^{-1} s it is possible to obtain the same resolution of 1 cm^{-1}.

Figure 5.9a compares different sweep velocities. As can be observed, the spectral features up to a sweep rate of 25 cm^{-1} s are well resolved but show a shift of the entire spectral range. This effect results from a timing-related error between sending the command to the laser and the start of the sweep, which causes an offset of the polled resonator frequency. To correct this shift, the peak position of a distinct absorption feature in the grey-shaded area in Figure 5.9a was evaluated for different sweep velocities and compared to a high-resolution step scan. Figure 5.9b shows the peak positions obtained for each sweep velocity, which is used for correcting the spectral shift accordingly. Taking this correction factor into account, the sweep mode enables a drastic improvement of the acquisition time, which, for a rate of 25 cm^{-1} s is providing a full spectrum with even higher resolution in just 26 s.

NEMS-IR spectroscopy of a polymer. For the first proof-of-concept experiment, the V2 system was tested with a solution containing polyvinyl alcohol (PVA). PVA is used in-house as a water-soluble support filament in the 3D printer and presents a simple analyte for testing the system to detect a polymer. The test analyte was prepared by a piece of the filament dissolved in Milli-Q water to a concentration of about 26 µg mL^{-1}.

To compensate for the power profile of the QCL, a spectrum of the empty/clean membrane resonator was recorded beforehand. After acquiring a background spectrum of the empty resonator, the system is vented, and the resonator sampled *in situ* using the aerosol setup. Figure 5.10 displays a micrograph of the 500 µm perforated membrane resonator sampled with approximately 6.7 ng PVA. The equivalent mass-load was evaluated by Equation 2.25, using the resonance frequencies of $f_0 = 203\,305$ Hz and $f_{load} = 191\,946$ Hz. From f_0 and the material parameters for Si_xN_y (see Tab. 2.1), a tensile stress of 91 MPa was obtained. Figure 5.11 shows the resulting spectra for hydrolyzed PVA obtained by NEMS-IR spectroscopy. To correct the power profile of the QCL, the response is calculated from the fraction of the relative frequency response for the loaded vs. empty chip (R_{load}/R_{clean}). The spectra were recorded with the GUI

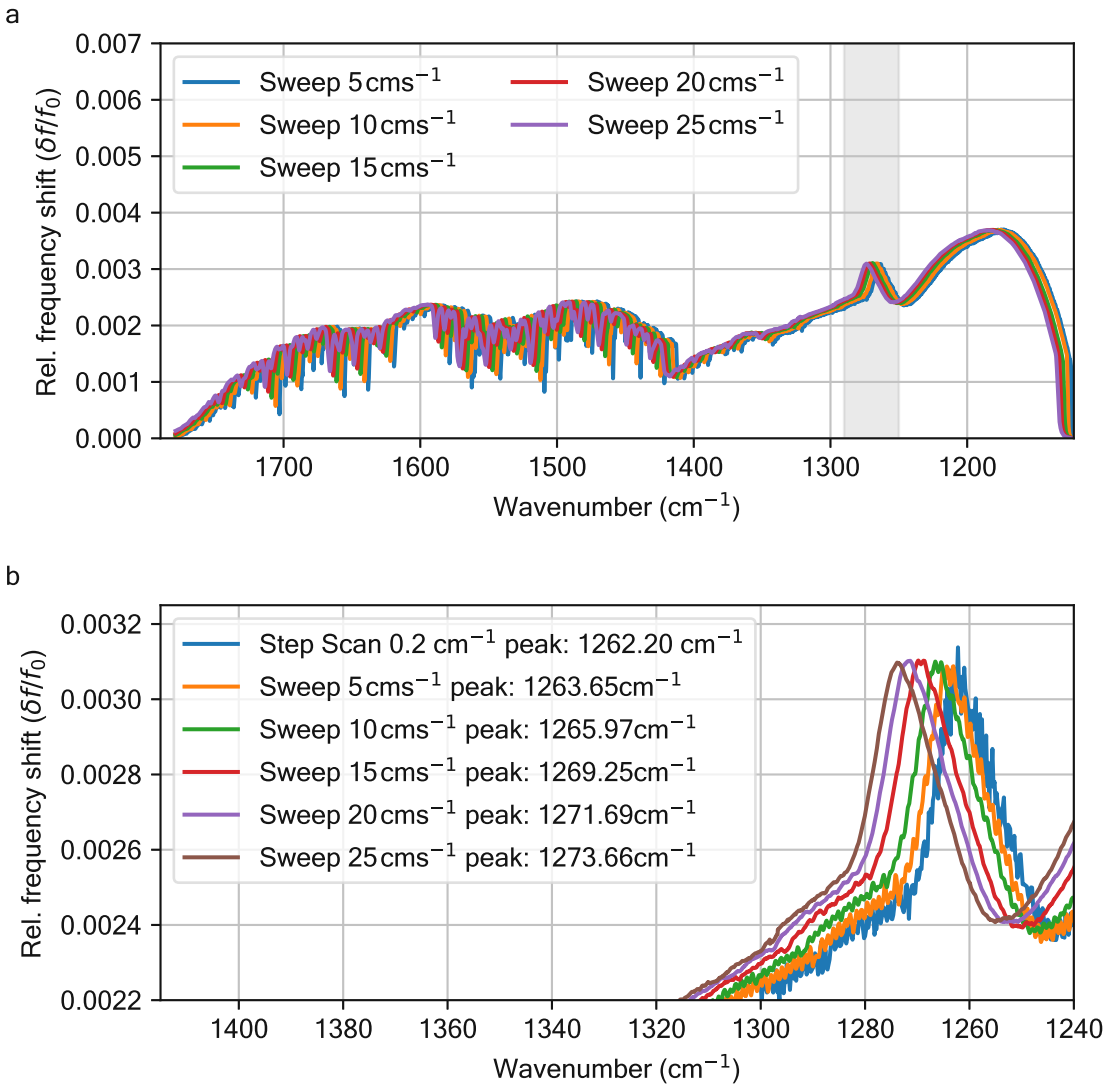

Fig. 5.9: Comparison of the QCL power spectrum using step scan and sweep mode. (a) The correlated relative frequency shift to the spectral wavenumber is affected by increasing scanning speed. This is due to a timing-related error of the laser between sending the command and the actual start of the sweep. (b) Evaluation of a shift correction of the peak position using a spectral feature (highlighted in (a) by the grey area) for different scanning speeds compared to the exact position using a high-resolution step scan.

using a step-scan mode with a resolution of 5 cm^{-1}. In comparison to literature [136], most of the vibrational modes such as ν(C=O) in the range of 1745 cm^{-1} to 1710 cm^{-1} originate from carbonic acid, saturated & unsaturated aldehydes and ketones. Further, one can identify OH from carbonic acid at 1440 cm^{-1}, and the bending mode γ_w(CH2). A direct comparison to an ATR reference spectrum from 'Elsevier library spectrabase' (ID 7W6RylUsSRT, 75 % hydrolyzed PVA, Sigma Aldrich) shows, in general, a good match.

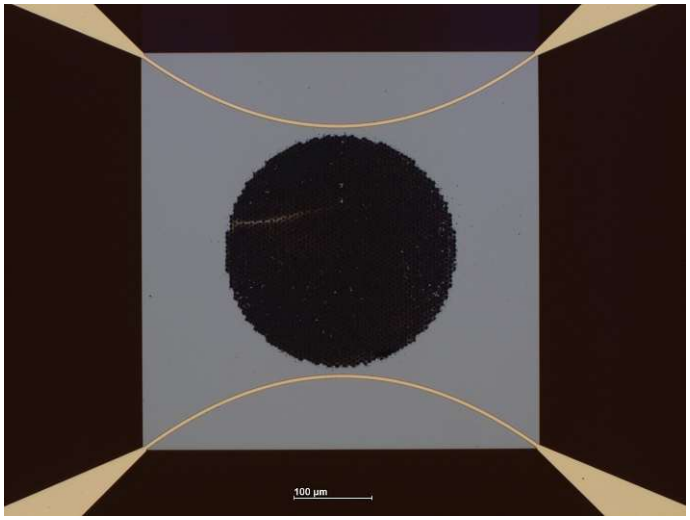

Fig. 5.10: Micrograph of a central perforated 500 µm resonator sampled with approximately 6.7 ng PVA from solution.

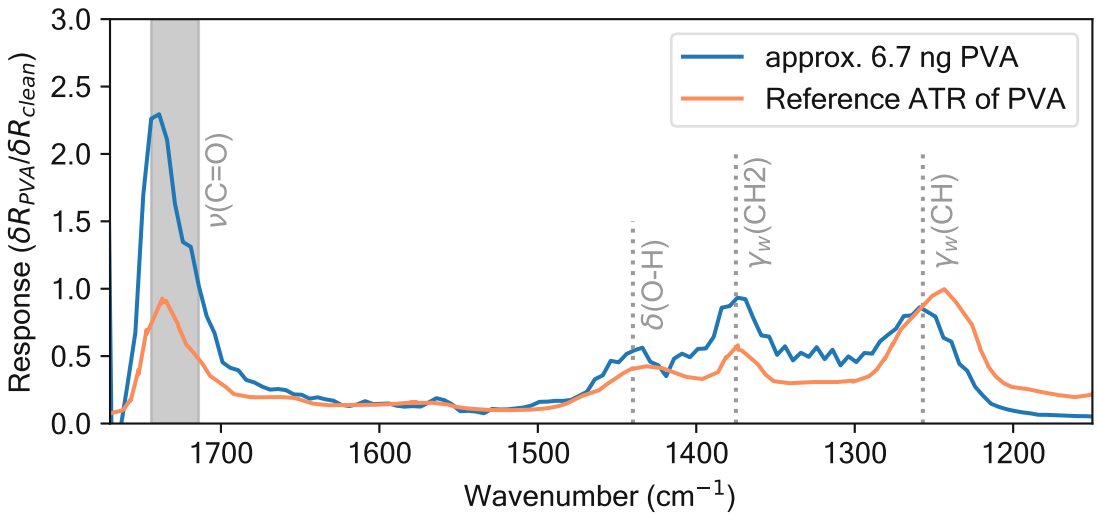

Fig. 5.11: QCL-power corrected spectrum of sampled PVA recorded by NEMS-IR spectroscopy compared to literature. The comparison to an ATR reference spectrum of hydrolyzed PVA shows, in general, a good match except for the spectral band position of the γ_w(CH) band, which is normally located at 1240 cm.

However, compared to the reference spectra and literature, the low spectral band position of the γ_w(CH) band is shifted. Considering that the PVA was sampled from solution, and the compound originated from a filament containing a mixture of different PVAs and other compounds to control the melting point, such a change due to different chemical compositions can be expected.

Analysis of trace impurities in organic solvents. In collaboration with the chemical department at TU Wien, the NEMS-IR setup was tested for the analysis of metal-organic gold clusters. During the study of low concentrations, several strong spectral features more prominent than the expected vibrational modes of the analyte could be observed. This gave rise to analyzing the organic solvents used for dilution.

Figure 5.12 shows the NEMS-IR spectra of the residues from sampled organic solvents. Clearly, these power-corrected spectra show strong absorption features at 1730 cm^{-1}, 1460 cm^{-1}, 1380 cm^{-1}, and 1280 cm^{-1}, which can be assigned to typical vibrational modes of functional groups such as carbonyl, alkane, and ester. Despite the HPLC-graded purity of 99.99 %, organic solvents such as methanol can still contain up to 150 ng mL^{-1} organic residues [137].

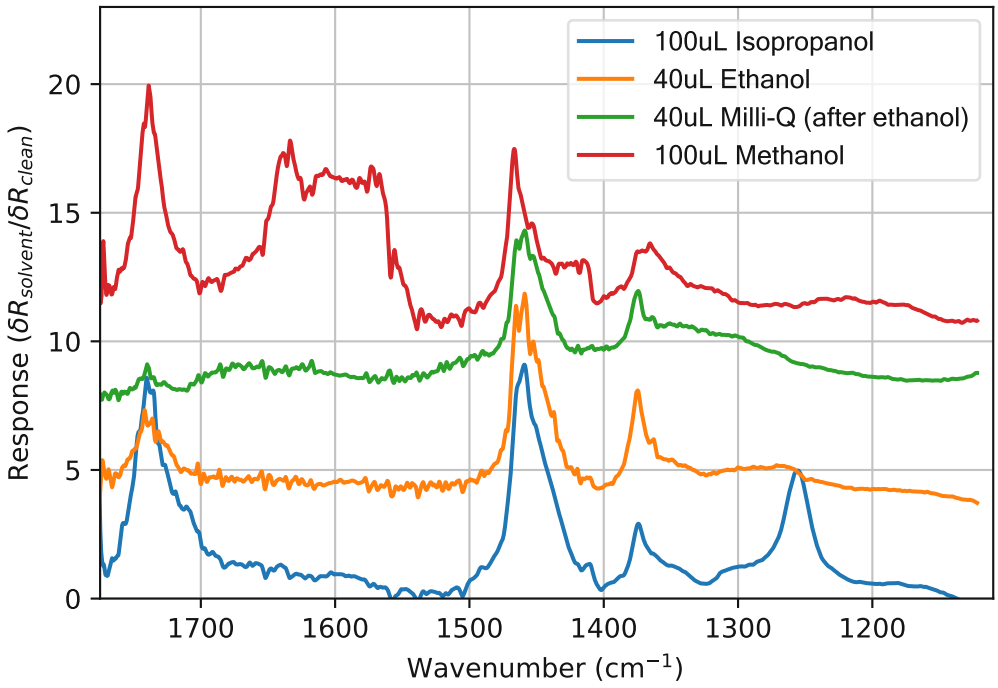

Fig. 5.12: NEMS-IR spectroscopy of organic residues from sampled HPLC-graded solvents on 500 µm perforated membranes. The spectral peaks at 1730 cm^{-1}, 1460 cm^{-1}, 1380 cm^{-1}, and 1280 cm^{-1} can be assigned to typical vibrational modes of carbonyl, alkane, benzene, and ester hydrocarbon groups which belong to known trace impurities of organic solvents [137, 138].

A dedicated study using MS analysis of classical solvents identified residuals of esters, n-hydrocarbons, and chlorinated hydrocarbons [137] which match well with the vibrational modes obtained in Figure 5.12. This underlines the high sensitivity of the NEMS-IR spectroscopy system and its potential use for analyzing trace contaminants.

Additionally, 'flushing' the system with Milli-Q water after sampling the same amount of, e.g., ethanol, still resulted in the same contamination on the resonator. This can be due to residues of sampling ethanol. As a result, the system was flushed for a minimum of 10 min before and after the sampling of a new analyte. However, this indicates that *in situ* aerosol sampling can contaminate the acquisition chamber and needs to be considered for future system iterations.

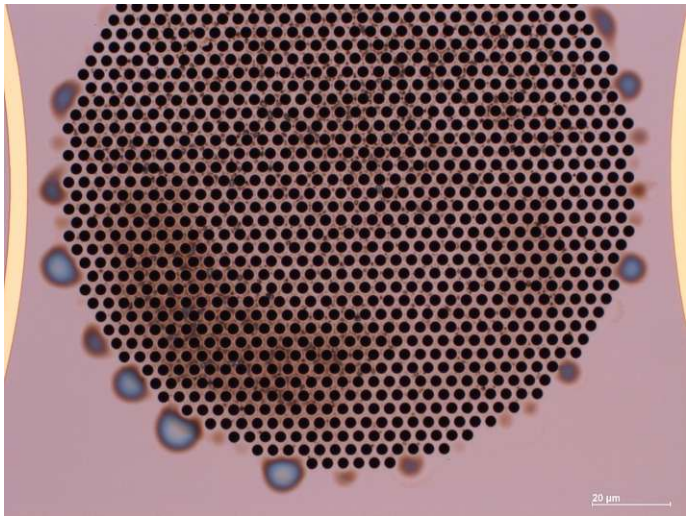

Fig. 5.13: Micrograph of the organic residuals from HPCL-grade isopropyl alcohol sampled on a perforated membrane resonator.

5.2.2 Optimization of the resonator design

In past developments of NAM-IR spectroscopy, several resonator geometries have been tested, ranging from cantilevers [139] over double-clamped strings [56] up to a perforated membrane [57]. Due to the strongly reduced heat transfer by conduction, a Si_xN_y string resonator provides the highest responsivity. However, to be used as an analytical device, the efficiency of sampling plays a crucial role. Despite a remarkable single filter-fiber collection efficiency of 65 % [76], a string only captures a small fraction of the available sample from an aerosol stream. In contrast, a perforated membrane significantly increases the absolute sampling efficiency but inherits the lowest relative response to absorbed heat. Further, in the example of Kurek et al. [57], the perforation pattern with 1 µm holes and distribution over the entire resonator caused clogging and sampling of analyte outside of the IR beam spot.

Following the considerations of the theory chapter and previous studies, a series of varying resonator geometries were developed and tested. Figure 5.14 shows a selection of several resonator designs ranging from a central perforated membrane to free-standing

perforated trampolines. The aim of the design is to find a trade-off between a high sampling efficiency, concentrating the analyte to the central area of the beam spot, and maintaining a high responsivity by reducing the heat transfer of the resonator.

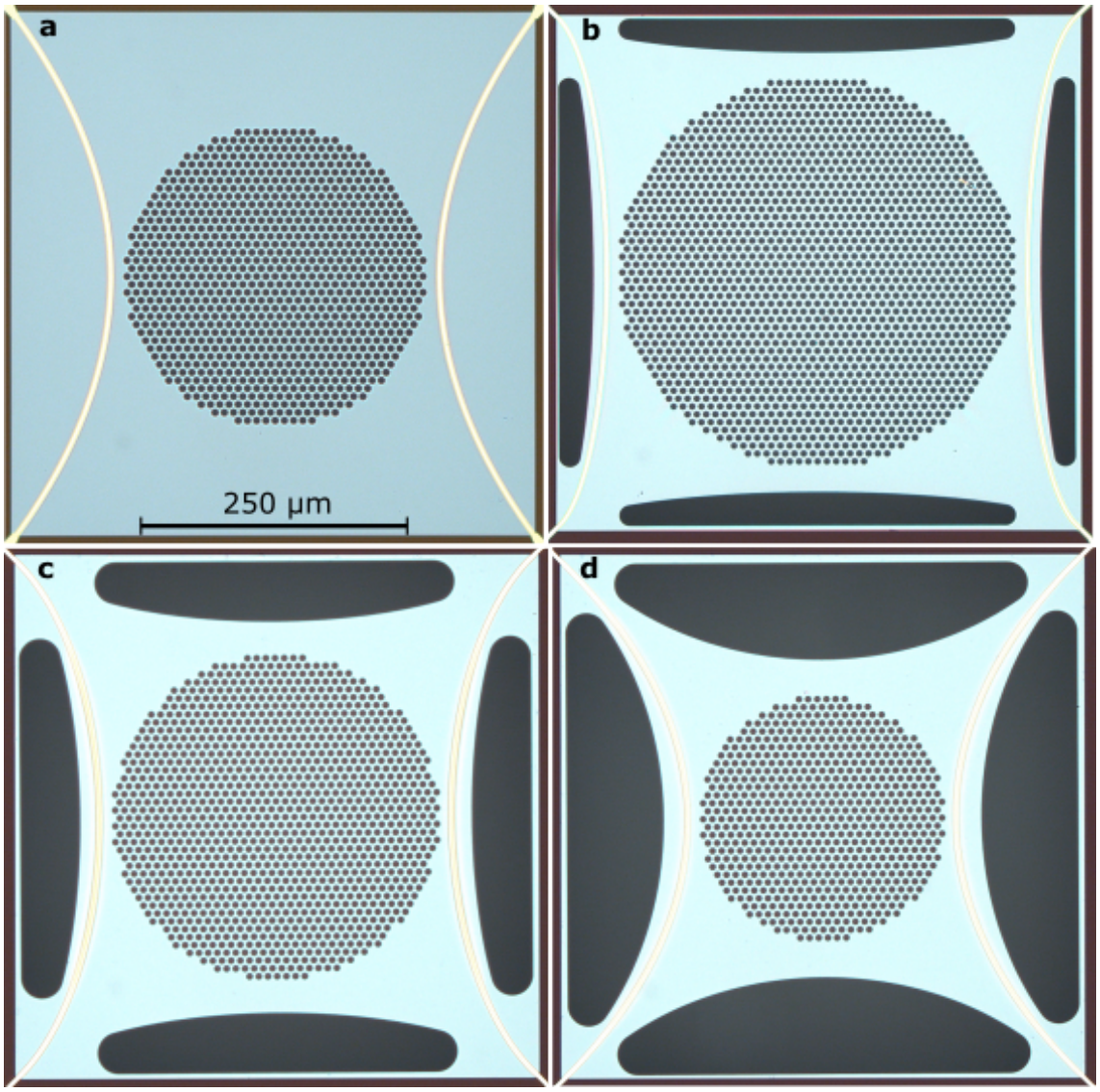

Fig. 5.14: Microscopic images of a selection of resonator geometries ranging from (a) a central perforated membrane to (b-d) perforated trampolines with a reduced clamping cross-section. All resonators are suspended over a 500 µm released window. The designs represent a trade-off between high sampling efficiency and high responsivity.

Comparison of sampling efficiency. The performance regarding efficiency and responsivity of the resonator designs was investigated as part of a supervised bachelor thesis. The following results are taken from [140]. For the analysis, all resonators were sampled by 10 µL to 40 µL of a solution of H_2O:isopropyl alcohol with a concentration of 57 µg mL^{-1} Indomethacin.

As expected, the perforated membrane resulted in the best sampling efficiency 1.53(9) % compared to a trampoline resonator 1.0(2) %) suspended over the same released area. The generally low efficiencies can be attributed to the significant sample loss in the cyclonic spray chamber during aerosol generation. Due to a lack of a suited particle counter by the time of the experiments, the loss could not be quantified. The efficiencies obtained are based on the fraction of the captured mass on the resonator extracted from the frequency change Equation 2.25 to the total introduced sample mass. Current experiments with a particle counter and using the same membrane design with an improved setup featuring a cyto-spray chamber and dedicated chip holder show sampling efficiencies up to 30 %. The efficiency of the trampoline designs using the improved system and methods is yet to be determined.

Comparison of power responsivity. To compare the performance in terms of power responsivity, the relative frequency shift for different amounts of Indomethacin was evaluated and linearly fitted to retrieve a normalized response value for each design. The relative frequency shift was taken from the strongest vibrational modes of Indomethacin within the spectral acquisition range, namely 1305 cm^{-1}, 1467 cm^{-1} and 1678 cm^{-1}. The relative frequency shifts were then normalized and plotted as a function of the sampled mass to extract a thermal response per sampled mass of Indomethacin. Figure 5.16 shows the response obtained per sampled mass for the most distinct resonator designs. The nomenclature '*M500 D6P3*' describes the resonator type (*M* = membrane / *T* = trampoline) lateral dimension of 500 µm, and perforation pattern, where *D* represents the perforation diameter and *P* the width between two holes.
Figure 5.15 shows the example of this analysis for a 500 µm sized trampoline-shaped resonator. As expected, the response per sampled mass on a trampoline-shaped resonator is generally higher than for a membrane. Regarding the lateral dimension, both 500 µm resonators show a slightly better thermal response than their 1000 µm sized relatives. Considering the 500 µm sized resonators to be at the onset of decreasing response to absorbed power (see theory Figure 2.3), a reduced response for the larger resonators can be expected.

Conclusion for the performance. To assess the overall performance of the resonator for the application in NEMS-IR spectroscopy, one has to consider both the response and sampling efficiency. With the priority set on an analytical device for low abundance samples, the gain in sampling efficiency of the membrane exceeds the sacrifice in power responsivity. However, for applications where high sensitivity is desired over efficiency, the T500 trampoline with the smallest clamping area shows the best performance.

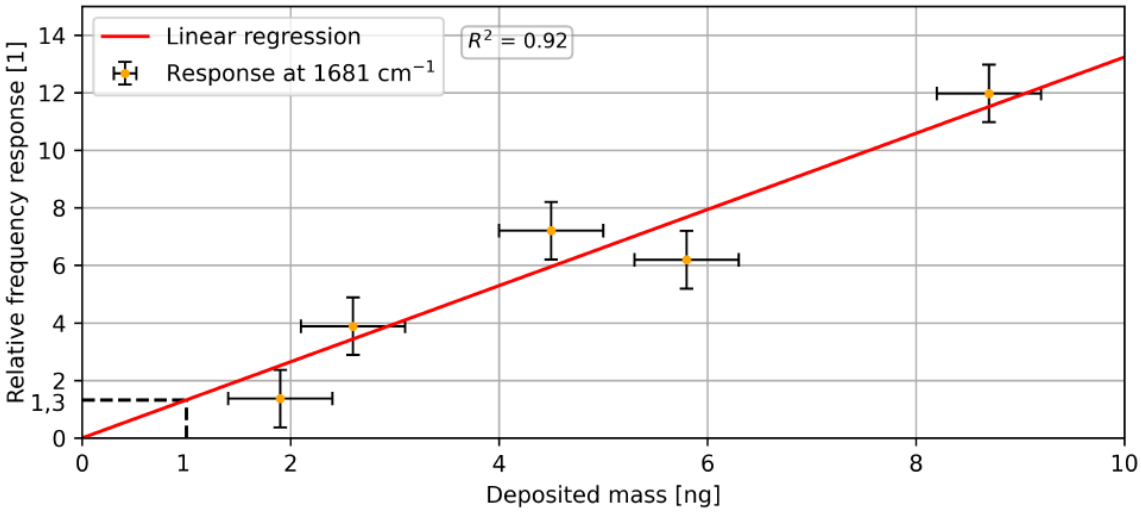

Fig. 5.15: Exemplary evaluation of the normalized relative frequency response for a trampoline resonator suspended over a 500 µm window. To compare the resonator designs, a linear fit is added to extract a thermal response per nanogram of Indomethacin. Image courtesy by C. Willert [140].

Resonator	Peak @ 1681 cm^{-1}	Peak @ 1467 cm^{-1}	Peak @ 1305 cm^{-1}
T500 D3P3	$1{,}32 \pm 0{,}226$	$1{,}13 \pm 0{,}180$	$1{,}06 \pm 0{,}153$
M500 D6P3	$1{,}03 \pm 0{,}121$	$0{,}81 \pm 0{,}134$	$0{,}56 \pm 0{,}077$
T1000 D3P1	$0{,}84 \pm 0{,}224$	$0{,}70 \pm 0{,}174$	$0{,}50 \pm 0{,}132$
M1000 D3P3	$0{,}58 \pm 0{,}012$	$0{,}59 \pm 0{,}020$	$0{,}40 \pm 0{,}050$

Fig. 5.16: Comparison of linear response per sampled mass for the most distinct resonator designs. Following the theoretical considerations, the trampoline generally shows a higher response to the same mass; likewise, the smaller resonators show a slightly higher response. Image courtesy by Willert, C. taken from [140].

Design considerations for robustness. Besides providing a high sampling efficiency and responsivity, a good fabrication yield and robustness of the resonator are desired. As can be observed from Figure 5.17a, the direct clamping of a trampoline as used in previous studies [75] causes a sudden mechanical stress change in the clamping area. This has often led to a low fabrication yield and rupture of such resonators during an experiment with high light intensities.

Following the benefits in robustness and mechanical quality factor presented by Sadeghi et al. [141], a round-edge clamping was implemented for all trampoline designs. Finite element simulations (COMSOL Multiphysics 5.4) of the round-edge clamping in Figure 5.17b with a suggested virtual radius of 20 µm clearly show a reduced and smoother stress field than a direct clamping. The practical experience of the duration of this

project showed consistent fabrication yields of >95 % and no sudden rupture of a resonator during an experiment.

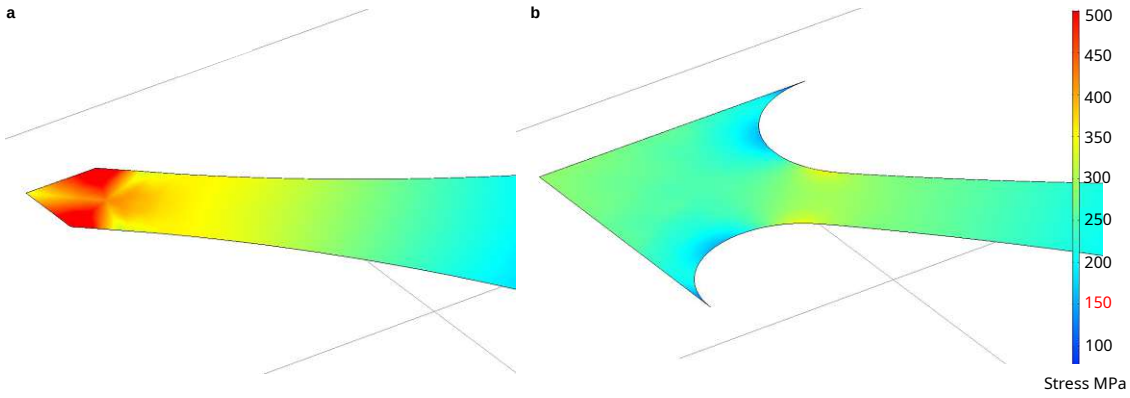

Fig. 5.17: Simulated stress distribution of the trampoline clamping area with an initial tensile stress of 150 MPa. Changing the clamping from (a) a direct connection to the frame to (b) a round edge with a virtual radius of 20 µm significantly reduces peak forces in the clamping area. Figure and formulation from VII.[7] - Copyright 2023 under a CC BY 4.0 license.

5.2.3 Proof-of-concept for NEMS-FTIR spectroscopy

In the following section, a proof-of-concept coupling of the NEMS-IR setup to a commercial FTIR spectrometer is demonstrated. Although the QCL resembles a fast and powerful light source for NEMS-IR spectroscopy, it covers only a small range of the IR spectrum. In contrast, an FTIR typically provides a spectral range from 5000 cm^{-1} to 500 cm^{-1} / 2 µm to 20 µm, making it a suited alternative. Figure 5.18 shows the schematic illustration of the NEMS-IR setup connected to a commercial FTIR spectrometer (Bruker Vertex 70). This research-focused FTIR features additional optical ports to couple out the modulated beam. The light of the external port is focused on the resonator by a combination of a flat and parabolic mirror.

To accomplish the communication and integration of the NEMS-IR setup with the FTIR's electronics & software, respectively, the resonator's response needs to be converted to a suited voltage. The lock-in amplifier used for the frequency tracking allows for a conversion of changes in frequency from the set 'center frequency' in the PLL to a voltage. Finally, the analog voltage with a linear conversion factor of 100 $mV\,Hz^{-1}$ can be sent via the auxiliary output of the lock-in to a dedicated analog-to-digital converter of the FTIR (AnaBox). Due to the measurement principle based on interferometry, the resonator is not measuring the response to individual emitted wavenumbers but the modulated light intensity of the globar resulting in an interferogram.

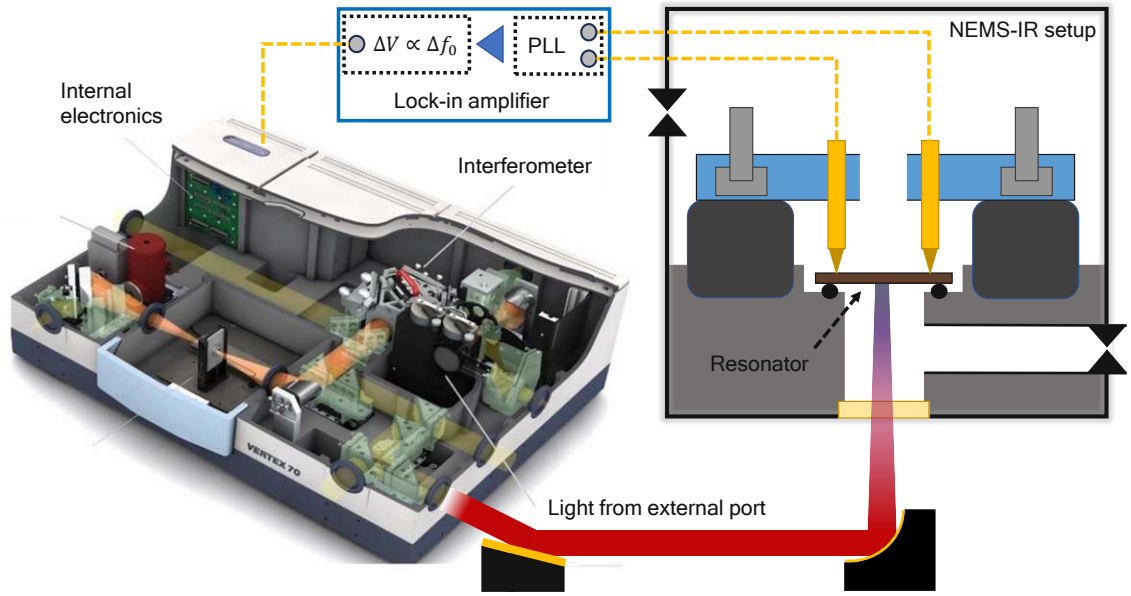

Fig. 5.18: Schematic illustration of the NEMS-IR setup coupled to the external port of a commercial FTIR. The light coming from the FTIR is focused on the resonator by combining a flat and parabolic mirror. The lock-in amplifier is used for frequency tracking of the resonator and converting changes from the PID center frequency to an analog voltage. The analog output is then connected to the internal electronics of the FTIR through an analog-to-digital converter (AnaBox by Bruker). This way, the setup can be operated by the FTIR software to acquire a spectrum.

Figure 5.19 shows an exemplary interferogram recorded by the modulation of the resonance frequency from a trampoline-shaped resonator. Due to the large thermal time constant of the nanomechanical resonator compared to the internal detector, a step scan mode of the FTIR was used. Using a classical continuous mode, where the mirror of the interferometer is moving with a defined speed, the resonator can not follow the modulation of light faster than 25 ms (40 Hz). In contrast, the step scan mode enables the acquisition at fixed mirror positions with a defined dwell time. As a drawback, this significantly increases the measurement time for a single spectrum to several minutes compared to a few seconds. A more detailed analysis of the impact of the modulation speed on the NEMS-FTIR spectra can be found in the last chapter Section 7.2.

Besides the scanning speed, the NEMS-IR setup suffers from thermal-related drifts of the resonator frequency in the duration of one step scan measurement, as can be seen by the constant increase in Figure 5.19. Such drifts are caused by a bad thermal connection of the resonator chip to the vacuum chamber, which for the purpose of *in situ* sampling is placed on a NBR O-ring ($\kappa_{NBR} \approx 0.3\,\mathrm{W/(mK)}$). In contrast, this drift could be readily compensated for the fast spectra acquisition in the QCL configuration.

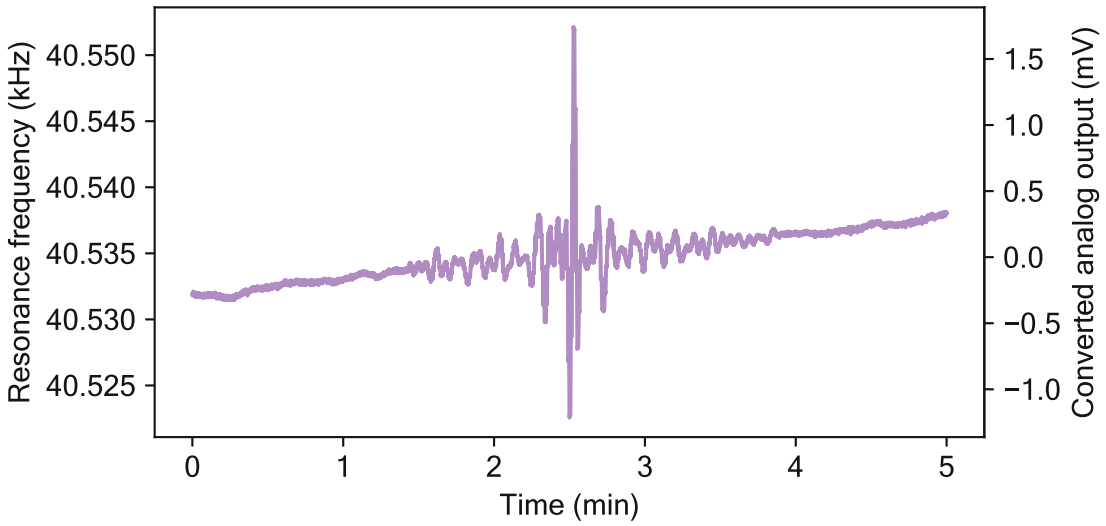

Fig. 5.19: Exemplary interferogram of an FTIR recorded by the modulation of the resonance frequency of a trampoline-shaped resonator. Using the conversion tool of the lock-in amplifier, changes of the center frequency set to 40.535 kHz are converted to voltage with a factor of 100 mV Hz^{-1}.

More specifically, for the GUI-enabled step scan mode, the current base frequency is evaluated for each individual step.

However, when operating the setup alongside the FTIR, this drift frequently poses challenges with voltage conversion, leading to issues such as clipping and especially affecting the AnaBox's input limitations. As a result, the conversion factor has to be reduced, which in turn reduces the converted signal available for the Fourier transformation. Alternatively, one has to wait for the stabilization of the resonator frequency or, ideally, integrate a thermo-electric element in good thermal contact with the resonator. Regardless of the aforementioned drawbacks, the combined NEMS-FTIR system was tested with a solution of PVA.

Figure 5.20 shows the resulting spectrum of a membrane resonator sampled with about 4.5 ng PVA. The comparison to the PVA spectrum recorded with the QCL-based setup and the reference spectrum shows, in general, a very good match. Moreover, the NEMS-FTIR spectrum shows the advances of an enlarged spectral range. This enables the photothermal detection of the high wavenumber vibrational modes such as ν(OH) stretching at 3350 cm^{-1} and ν(CH) of the PVA alkyl backbone at 2925 cm^{-1} & 2855 cm^{-1} [142, 143]. The prominent absorption feature at 890 cm^{-1} can be attributed to the Si_xN_y of the resonator itself. Surprisingly, this peak is significantly shifted from the 835 cm^{-1} maximum obtained in the classical transmission mode of the FTIR.

This could be related to a false phase- and quadrature information generated during the step scan acquisition [144]. However, this does not affect the spectral position of vibrational modes of the sampled analyte, which matches the band positions in the literature. The effect of the dislocated $\nu(Si_xN_y)$ peak position is still under investigation. Overall, considering the decent spectrum for only a few nanograms of PVA compared to the milligrams typically needed in conventional transmission spectroscopy, this study shows the high potential of NEMS-based FTIR spectroscopy.

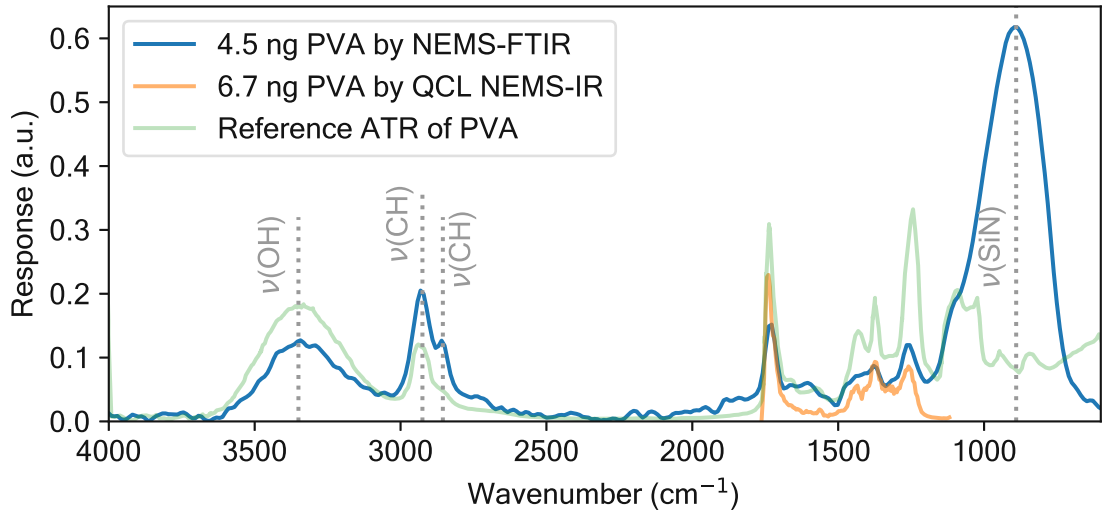

Fig. 5.20: NEMS-FTIR spectroscopy of PVA sampled on a perforated membrane resonator. The comparison to the PVA spectra measured by the QCL system and the ATR reference shows, in general, a good match. The strong absorption band in the low wavenumber region can be attributed to the vibrational mode of the Si_xN_y resonator material (see also Figure 4.4).

5.3 NEMS-IR setup featuring a temperature control

Based on the insights gained from all proof-of-concept measurements performed on the previous NEMS-IR setup, several upgrades were implemented to a new system. Figure 5.21 shows a schematic illustration and picture of the upgraded setup, highlighting the main components such as an improved contact bridge based on a PCB, a turbopump system, and a thermo-electric element and copper block featuring a thermo-resistor. The mechanical load on the soldered cables by mounting/unmounting the contact bridge often broke the electrical connection. Therefore, dedicated PCBs for a new contact bridge and connection to the 9-Pin SubD vacuum flange were designed.

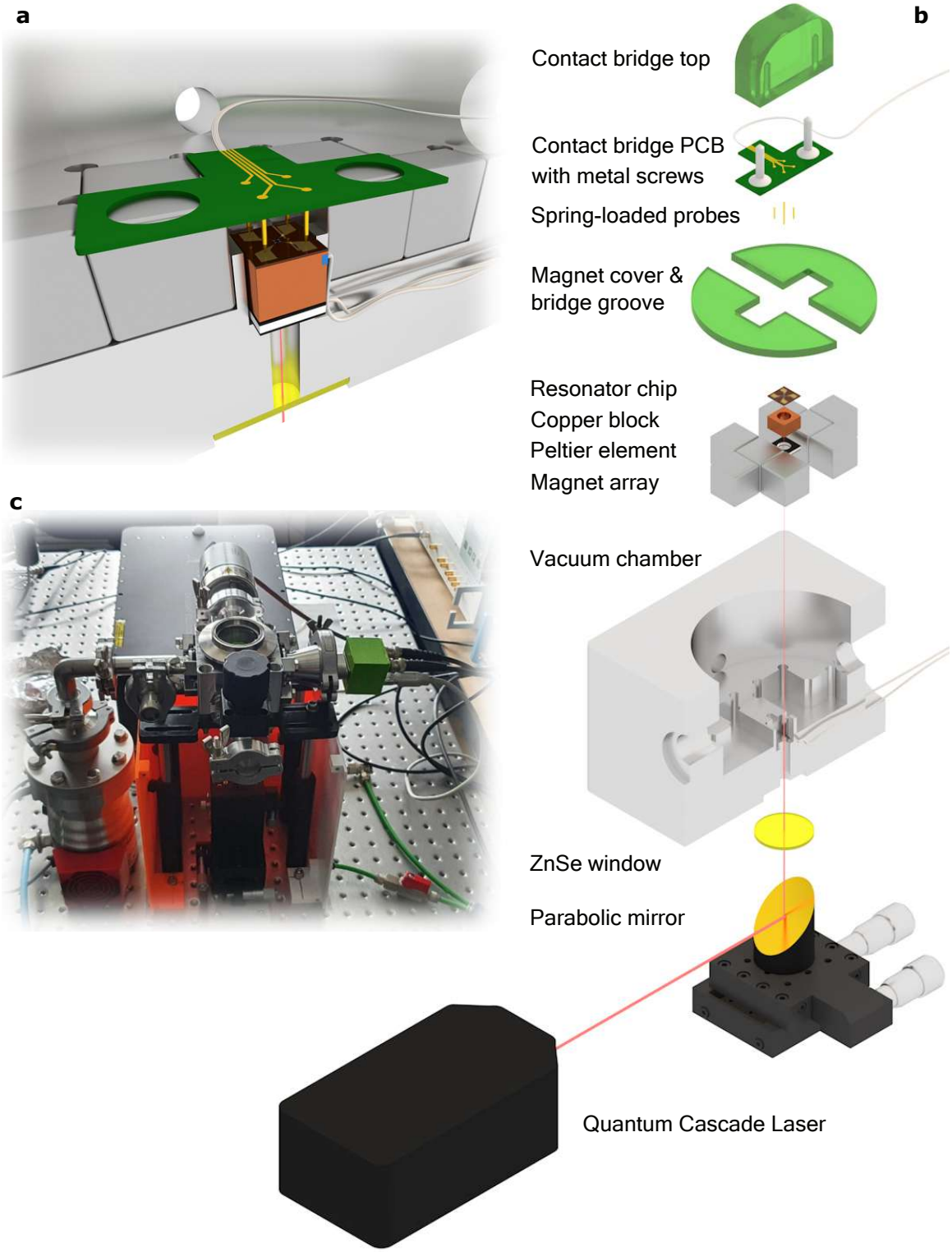

Fig. 5.21: Overview and insights of the upgraded NEMS-IR setup. (a) Close-up illustration of the vacuum chamber with a resonator chip placed on the copper block and thermo-electric element and connected to the PCB contact bridge. (b) Explosion figure highlighting all components of the system. (c) Picture of the assembled setup featuring a turbopump and opened purge box (orange) for reducing absorption by water vapor.

This enables a connection to the contact bridge by a flat-band cable and a novel 3D-printed design with ergonomic groves for placing the bridge in the chamber. To minimize variations of the light intensity by water vapor in the beam path, a 3D-printed box equipped with a gas inlet was designed and wrapped with cling film. This way, a defined and approximately constant atmosphere can be provided during the measurements, which is important to reduce the noise for the power profile correction of the spectra. Figure 5.22 displays the power profile of the QCL module in the spectral range of the water vapor absorption. The spectra were recorded with a trampoline-shaped resonator under constant settings but for different atmospheres in the purge box. For the highest purge flow of 250 L h^{-1} nitrogen, the absorption peaks of water vapor can be significantly reduced and kept constant for the duration of measurements. Since the laboratory did not provide a direct nitrogen supply, the purge gas was later changed to dry air from the pressurized air supply, which performed similarly.

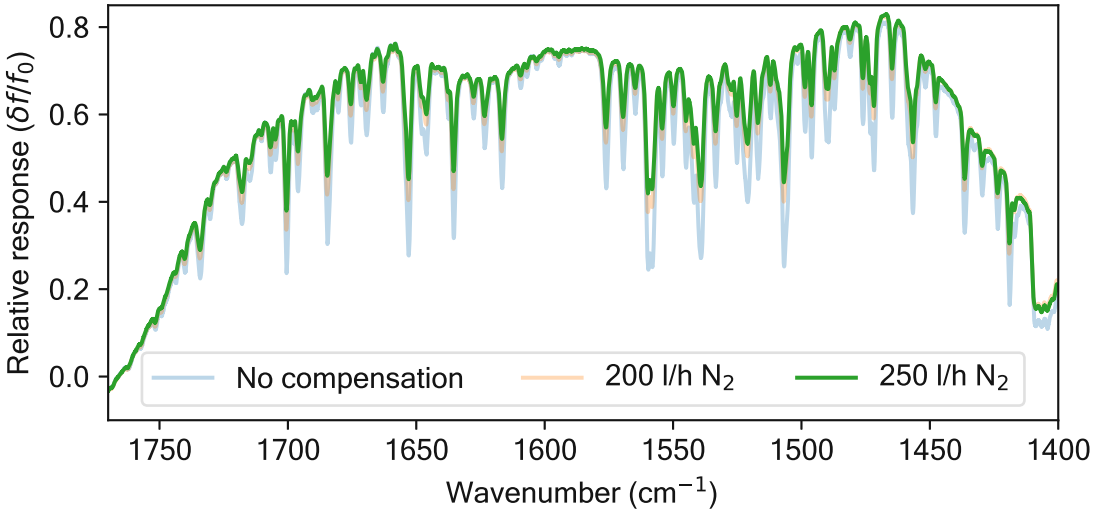

Fig. 5.22: Comparison of the QCl power spectra measured with a trampoline-shaped resonator for different volume flows of nitrogen in the purge box. With a volume flow of 250 L h^{-1} nitrogen, the absorption of water vapor bands can be significantly reduced and kept at a constant level.

The *in situ* sampling feature in the initial setup generation facilitated direct measurement of both background spectrum and analyte without requiring chip exchange. However, it frequently resulted in cross-contamination from prior experiments, as illustrated in Figure 5.12. Despite extensive system flushing attempts, these contaminants sometimes remained. Moreover, this setup did not enable remote or mobile in-field sampling of the resonators, for instance, concerning environmental aerosols. Consequently, the sampling was relocated outside the system and back into a dedicated sampling chamber.

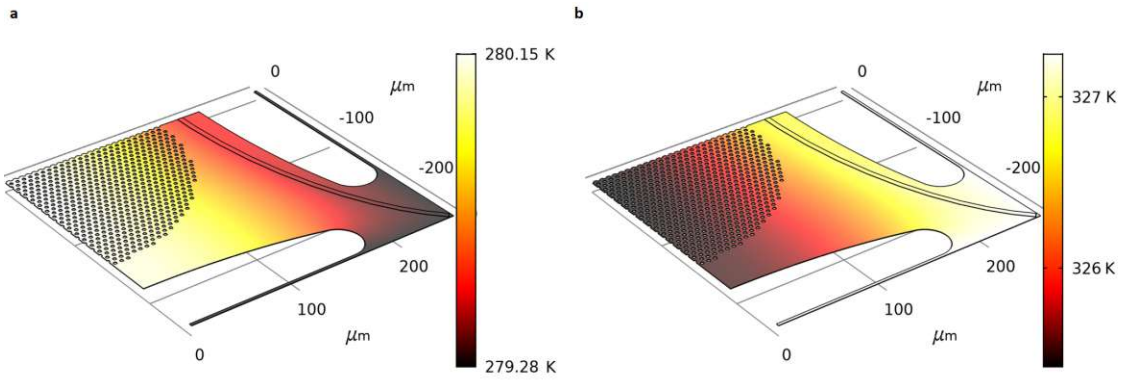

Fig. 5.23: FEM simulation of temperature distribution of a trampoline-shaped resonator under (a) cooling and (b) heating of the frame. The low heat transfer of the material compared to the high thermal conduction of the electrodes leads to an inhomogeneous temperature field along the resonator. Figure and caption adapted from the supplementary information [7]- Copyright 2023 under a CC BY 4.0 license.

One of the most prominent issues during all measurements was the drift of the resonance frequency due to bad thermal coupling or residual liquid desorbing from the resonator in a vacuum. This was tackled by implementing a thermo-electric element and copper block acting as a heat sink to buffer fast changes in the temperature. The temperature of the thermo-electric element and copper block is held constant by a PID controller (DX5100 - TEC Microsystems) with a thermo-resistor PT1000 integrated below the resonator at the top of the copper block. Considering the low heat transfer of the resonator, the temperature of the central perforated area comprising the analyte will differ from the set temperature of the copper block.

Figure 5.23 shows the temperature distribution of a trampoline resonator simulated by FEM (COMSOL Multiphysics 5.4). As can be observed, the significantly higher thermal conductance of the transduction electrodes leads to a faster thermalization of the resonator to the set chip temperature. Still, for the case of heating the chip as in Figure 5.23b, the central perforated area temperature can be about 3 K lower than the chip frame.

For calibrating the chip/frame temperature holding the resonator, a dummy chip was equipped with a thermo-resistor soldered to the contact pads, as displayed in Figure 5.24a. The resistor was electrically connected to the SubD port of the vacuum chamber by hijacking the contact bridge. This way, the temperature of the chip center could be measured simultaneously with the temperature of the copper block, which inherits the same thermo-resistor connected to the temperature controller.

Figure 5.24b shows the resulting temperature curves obtained from the thermo-resistor of the copper block (set temperature of the PID), the thermo-resistor on the chip, and

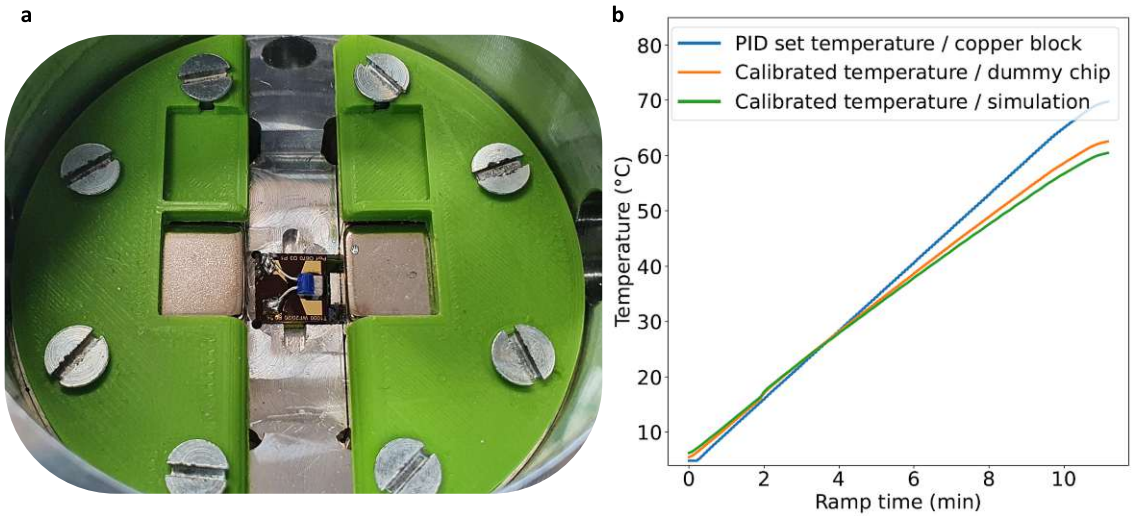

Fig. 5.24: Calibration of the resonator temperature (a) Picture of the modified resonator chip with soldered thermo-resistor. (a) Obtained temperature by on-chip thermo-resistor compared to programmed temperature ramp and FEM simulation of the resonator center. Figure adapted from the supplementary information [7] - Copyright 2023 under a CC BY 4.0 license.

the related frame temperature used for simulation of the resonator center. As can be observed, the resonator temperature differs to slightly lower values at high temperatures and vice-versa for cooling of the chip below room temperature (22 °C). For all further analysis, the calibrated temperature profile was used.

5.3.1 Application for desorption and adsorption analysis

The introduction of analytes such as caffeine turned out to be semi-volatile under the operating vacuum of the setup. Figure 5.25 shows the rising resonance frequency of a caffeine sampled chip at room temperature (~22 °C). The continuous rise approaching a constant value can be explained by the desorption of caffeine from the resonator, following a typical first-order desorption kinetic (assuming no dissociation or recombination of the desorbed species [145]). A more detailed study of the desorption kinetics can be found in the following chapter.

The desorption trajectory follows up to an equilibrium state, where the resonator remains at a constant frequency due to the remaining 'clean' surface. It is noteworthy, that for sampled analytes containing organic solvents, the resonator remains stable with some residual contaminants which are not volatile. This, however presents a suited method to correct the analyte spectrum from the background spectrum of the contaminants.

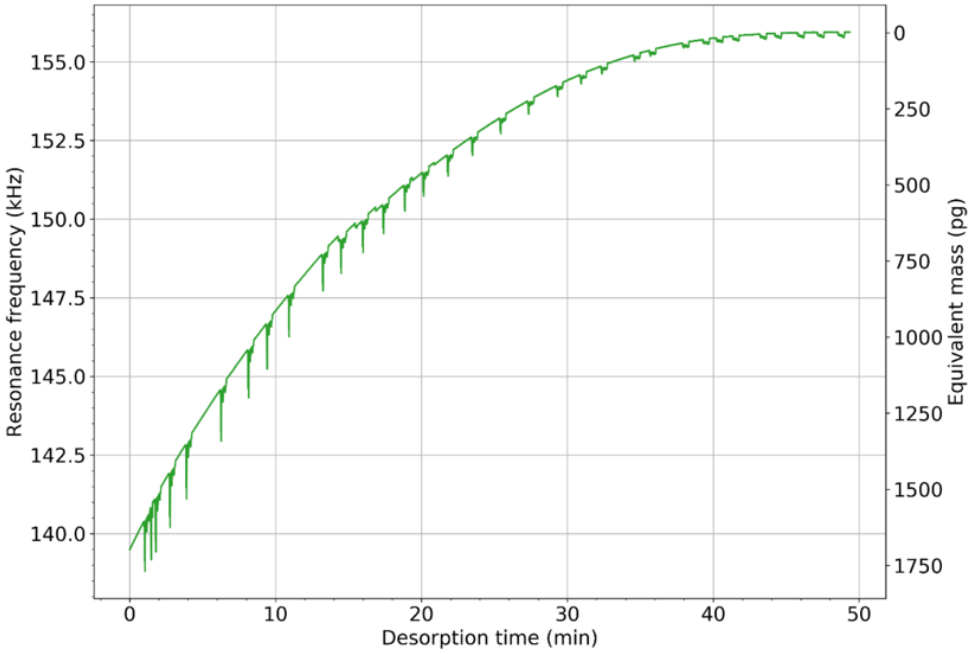

Fig. 5.25: Resonance frequency of a trampoline loaded with caffeine set to room temperature. In a vacuum, the semi-volatile caffeine desorbs from the resonator surface back to the clean resonator frequency. During this process, several spectra of the current caffeine load were recorded.

During the desorption process, the current mass load by caffeine can be analyzed by NEMS-IR spectroscopy, which can be seen by the sudden 'spikes' along the frequency trajectory in Figure 5.25.

Figure 5.26 shows the raw response for a set of different caffeine mass-loads on the resonator. The spectral assignments of literature values show a perfect match to all vibrational modes predicted for caffeine in the available spectral range [146]. This holds true for decreasing amounts of caffeine, which show a linear decrease of the response, which indicates the desorption to be a suited tool for analyzing the detection limit. Considering this response for single nanograms of material, these spectra underline the power of NEMS-IR spectroscopy over classical approaches such as transmission FTIR, where milligrams of the sample are needed.

Integrating a thermo-electric element into the NEMS-IR setup further enables the control of the resonator temperature and, thus, the desorption process of semi-volatile compounds. Figure 5.27 shows the frequency of a caffeine-sampled resonator for different settings of the resonator temperature. Clearly, with increasing temperature, the desorption rate of caffeine can be altered. The spikes in the frequency are a result of NEMS-IR acquisitions performed during this study.

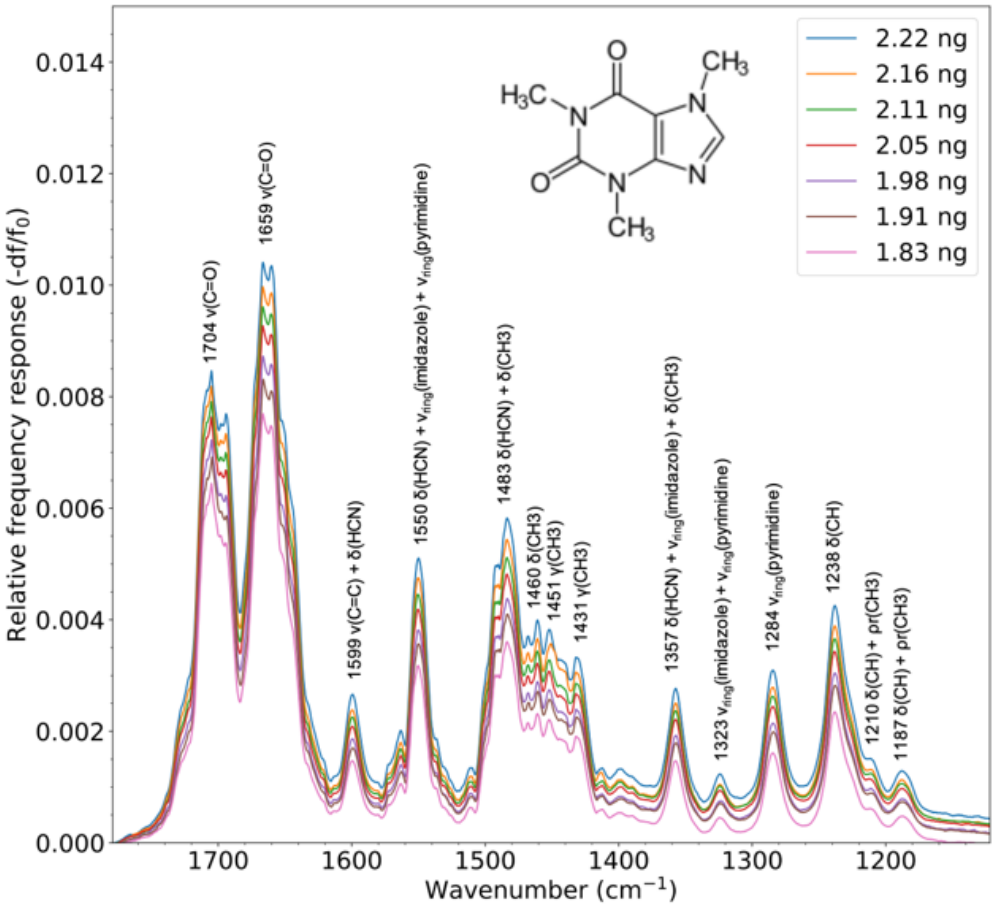

Fig. 5.26: NEMS-IR spectra of different amounts of caffeine. Comparison of the spectra to literature shows that all vibrational modes within the acquisition range can be identified [146]. The measurement indicates that desorption can be used as a suited feature to precisely study the detection limit of the system.

At the end of this study, the temperature is changed back to the initial 10 °C, indicating a similar desorption rate in terms of frequency change as for the same temperature at the beginning of this experiment. Further, apart from the desorption rate, a change in temperature also influences the 'static' resonance frequency. This is due to different thermal expansion or contraction of the chip-frame, respectively, compared to the suspended resonator. Besides the control of desorption by increasing the temperature, also the adsorption of compounds can be analysed. Operating the resonator below room temperature will make the surface act as a cold-finger trap in the vacuum chamber. This effect was studied on an initially clean resonator set to 5 °C for the duration of one hour. Figure 5.28a shows the resulting drop in resonance frequency due to the continuous condensation/adsorption of residual molecules in the vacuum chamber. Recording several NEMS-IR spectra during this process, one can see rising spectral features at 1730 cm^{-1},

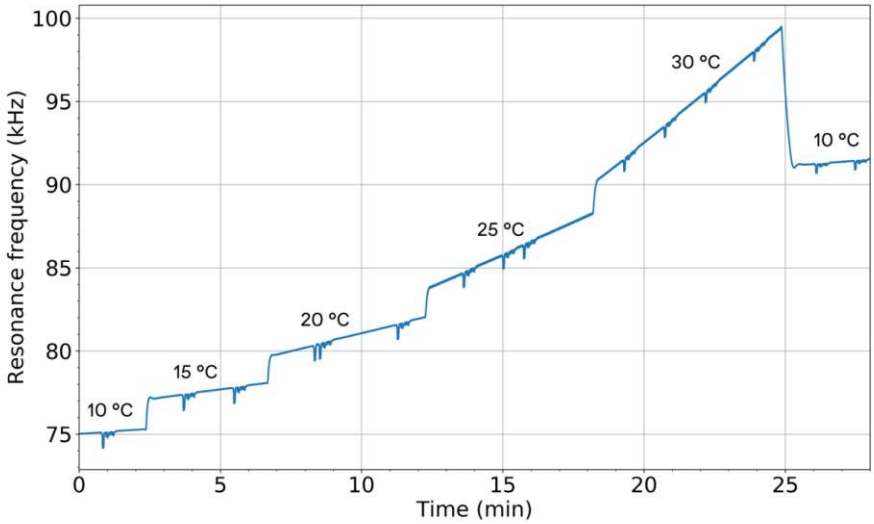

Fig. 5.27: Example of temperature-controlled desorption of caffeine from the resonator. Depending on the set temperature of the resonator, caffeine desorbs at a different rate.

1460 cm^{-1}, 1380 cm^{-1}, and 1278 cm^{-1}. These can be assigned to typical functional groups of carbonyl, alkane, benzene, and ester, known as common residual hydro-carbons in vacuum systems [147, 148]. Those are similar to the organic contaminants observed in solvents, presented in Figure 5.12.

5.4 Conclusion & outlook

The path to a system with fully integrated transduction demonstrated the ability to obtain high-resolution spectra of compounds such as polymers (PVA), pharmaceuticals (IMC), and semi-volatile organic compounds (caffeine) with only a few nanograms. The developed contact bridge enables fast exchange of resonator chips without any chip preparation, such as wire-bonding or gluing to PCB. A homemade graphical interface allows simultaneous communication to the QCL and lock-in amplifier, which enables automated spectra acquisition. In a proof-of-concept experiment, the hyphenation of the NEMS-IR setup to a commercial FTIR could be successfully demonstrated and tested for the detection of hydrolyzed PVA.

Implementing a purge chamber to the NEMS-IR setup significantly reduced the intensity noise of the IR beam by absorption of water vapor bands. The thermo-electric element and thermo-resistor enable the stabilization of the resonator temperature and the precise control of the desorption of semi-volatile compounds such as caffeine.

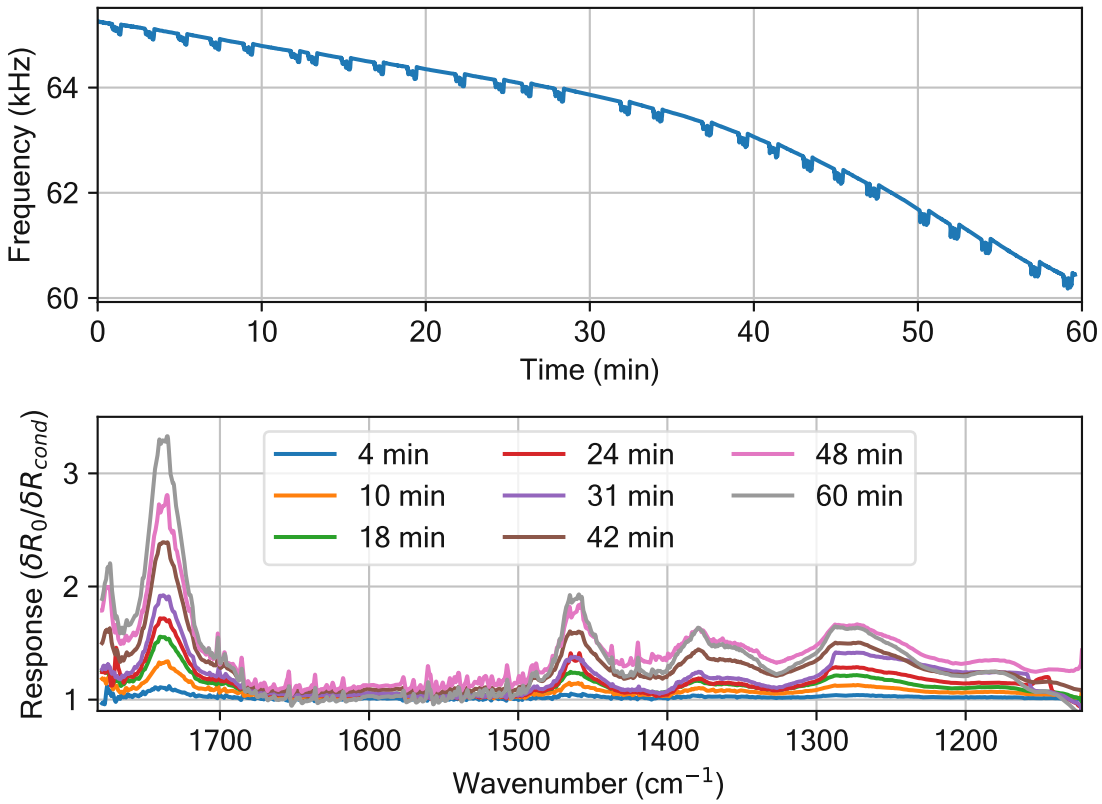

Fig. 5.28: Observation of adsorption on a resonator operated at 5 °C. (a) Rising spectral features appearing at 1730 cm^{-1}, 1460 cm^{-1}, 1380 cm^{-1}, and 1278 cm^{-1} can be assigned to typical carbonyl, alkane, benzene and ester hydrocarbon-groups [147, 148] (b) Dropping resonance frequency due to the additional mass-load of the condensed/adsorbed compounds.

In addition to controlling desorption rates, this feature allows the condensation and analysis of residual contaminants from the vacuum system. In general, this opens the possibility to use the thermo-electric element for the *in situ* study of temperature-controlled desorption in conjunction with NEMS-IR spectroscopy.

6 Demonstration of NEMS-IR-TD spectroscopy

The following chapter's results, formulations, figures, and discussions are based on the publication [7].

Much like traditional IR techniques, analyzing complex samples using NEMS-IR presents a significant challenge. In conventional IR spectroscopy, addressing complex analytes often involves hyphenating the detection technique with a preceding separation step upstream, such as liquid- or gas-chromatography (LC/GC). This approach is widely adopted in mass spectrometry (MS), where LC and GC serve to separate analytes prior to detection. Consequently, GC and LC have been effectively integrated with Fourier-transform IR spectroscopy (FTIR) as well [149, 19]. Alternatively, one can make use of temperature-programmed desorption (TPD). Although TPD is typically used as an analysis tool to study, e.g., adsorbate–surface interactions [28], decomposition [34, 29], and catalytic processes [150], it can also be used as a separation method [151].
With the capability of controlling the resonator temperature, the upgraded setup can be used for *in situ* thermogravimetric analysis and NEMS-IR spectroscopy at the same time.
The following chapter introduces the novel technique of NEMS-IR-TD spectroscopy and its vast capabilities to precisely acquire the detection limit and study the desorption dynamics of single compounds and mixtures. As a demonstration, the semi-volatile compounds caffeine and theobromine were selectively identified and quantified from a mixture. Thereby, the desorption process can be monitored twofold, by continuously recording IR spectra in a defined interval and by measuring the mass loss in real time. The resulting time-resolved IR spectra can readily be decomposed by singular value decomposition (SVD). A more profound decomposition by global analysis adapted from the field of ultrafast spectroscopy further enables the identification and study of the dynamics [152, 153, 154, 155].

6.1 Sample and resonator preparation

All analytes in this chapter were sampled from a liquid solution using the developed aerosol sampling setup and optimized parameters (Section 5.1). The crystalline compounds, caffeine (Sigma Aldrich - 42993-100MG) and theobromine (Sigma Aldrich C0750-5G), were dissolved and diluted in Milli-Q water to a stock solution with a concentration

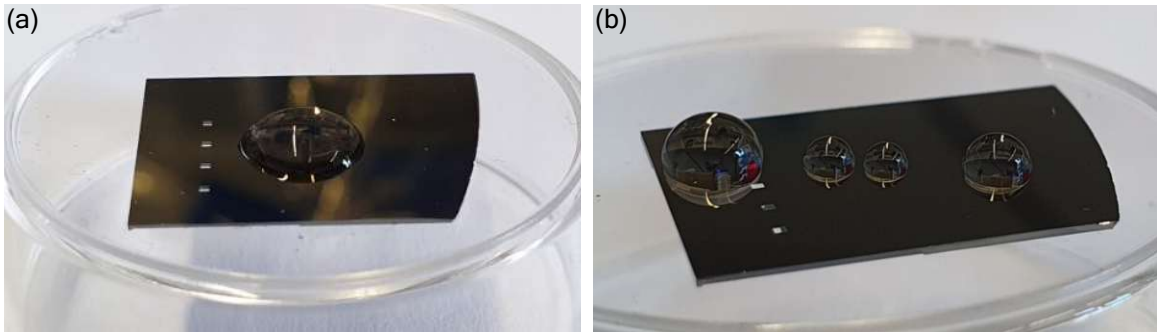

Fig. 6.1: Pictures of a bare wafer piece with 50 nm Si_xN_y with a drop casted water droplets on (a) an untreated substrate and (b) passivated by trimethylchlorsilane.

of 50 µg mL^{-1} to 62 µg mL^{-1}. Due to the higher sensitivity performance obtained during the resonator optimization, only trampoline-shaped resonators of the size 500 µm and 1000 µm were used throughout this study. To achieve consistent surface characteristics and minimize compound adhesion to the resonator, passivation is employed, resulting in a uniformly functional resonator surface for each desorption experiment. The chips were therefore passivated with trimethylchlorosilane (Sigma- Aldrich, cat.no. 386529) following a protocol from M. Szkop et al. [156]. This procedure binds a mono-layer of Si-$(CH_3)_3$ groups to the native SiO_2 layer of the resonator. Figure 6.1 shows pictures of two wafer pieces with a typical Si_xN_y layer and drop-casted water droplets on a regular and passivated surface. Due to the passivation layer, the surface is hydrophobic, which drastically increases the contact angle of the water, as can be seen in Figure 6.1(b). As a side-effect, a passivated wafer or resonator can be pulled out dry after rinsing with Milli-Q, which makes the chips easy to clean and even reuse.

6.2 Spectra acquisition and data post processing

For the spectra acquisition during an isothermal desorption measurement, the home-made GUI was extended by an interval feature. This way, one can define a spectral range, sweep speed, and repetition interval. The result of each sweep containing the 'baseline' frequency f_0 of the resonator prior to emission and relative frequency shift as a function of the wavenumber is automatically saved with the total experiment time and interval number. All IR spectra in the following analysis were acquired by using the continuous sweep mode of the QCL set to a speed of 25 cm^{-1} s^{-1} (26 s per spectrum) and a repetition interval of 2 min to generate spectro-temporal maps (see Figure 6.4).

To compensate for influences on the resonance frequency, such as the continuous rise due to desorption during a sweep, all spectra were post-processed using a dedicated

Python script. In the first step, the script parses all spectral data and performs a linear rising correction factor to each spectrum. This is done by factorization of the spectrum with a linear function with a slope defined by the first and last point of the spectrum. For the short duration of 26 s of a scan, a linear correction was deemed acceptable. In a second step, the drift-corrected spectra are shifted by $-11.68\,\mathrm{cm}^{-1}$ to account for the timing-related error of the QCL sweep, described in the previous chapter (see Figure 5.9). During the post-processing of desorption/adsorption datasets, it turned out that this timing-related error eventually shifts for a limited time, which caused a misalignment of subsequent spectra blocks, as can be seen in Figure 6.2. To correct this effect, a spectra-correlation-loop was programmed to identify and shift misaligned spectra to the 'right' position. The verification of the exact band position was obtained by a step scan mode of the QCL.

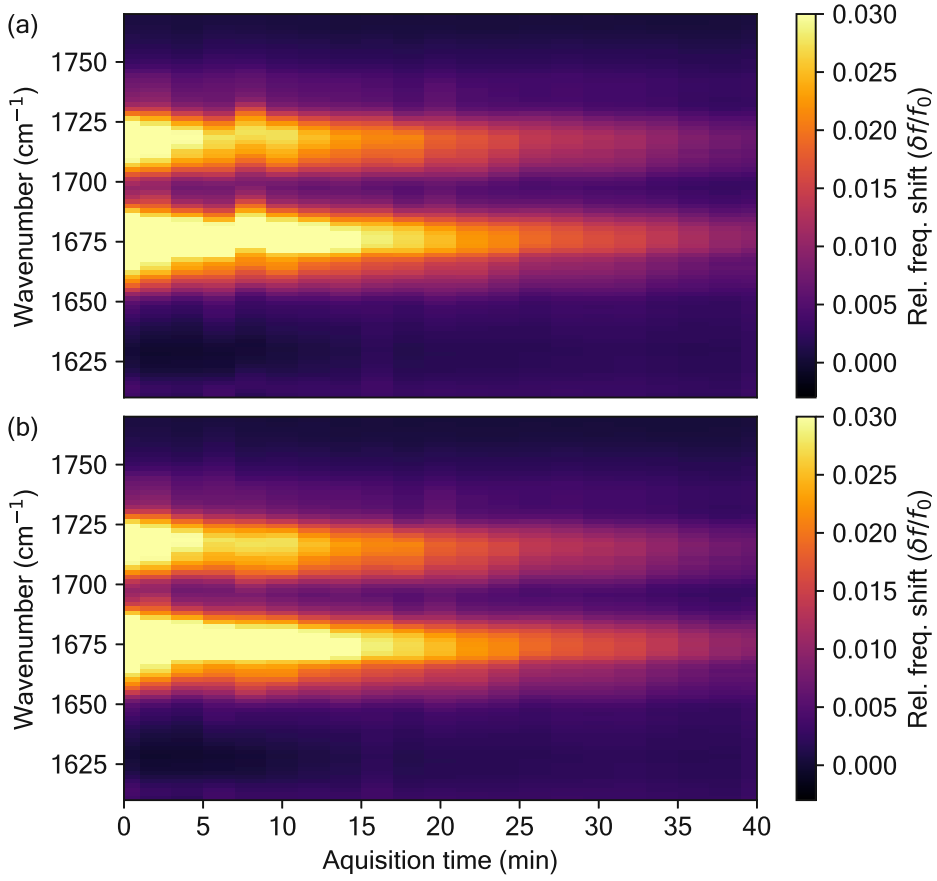

Fig. 6.2: Spectro-temporal heat maps of a caffeine desorption at 20 °C. (a) Raw signal with shifted blocks and (b) after application of the spectra-correlation-loop.

To evaluate the detection limit, the frequency before light emission, which is recorded along with each spectrum, was extracted and converted to a mass-load by a third-order Taylor expansion of Equation 2.21 (see Figure 2.5). The necessary frequency of the unloaded resonator was taken from the average of the last five datasets that showed no change in spectral features or resonance frequency. Likewise, the average response of the same five datasets is used to subtract the background spectrum of residual contaminants that remained on the resonator's surface. Finally, the maximum response of the strongest vibrational mode is plotted as a function of the corresponding mass load and is linearly fitted to obtain a response slope. The detection limit is then calculated by the three-folded standard deviation of the background average divided by the response slope for the specific analyte.

6.3 Analysis of the detection limit for single compounds

The NEMS-IR-TD system was first tested with pure chemical compounds. Figure 6.3 shows the IR spectra obtained for individual sampled caffeine and theobromine. To compensate for the power variations of the QCL, the spectra were corrected by dividing with the blank spectrum of the bare resonator δf_{BL} and further subtracting the background spectrum of residual contaminants that could not be desorbed ($\delta f_{BG}/\delta f_{BL}$). Comparison to reference spectra recorded on a commercial attenuated-total-reflection (ATR)-FTIR shows nearly identical spectra. In the ATR-FTIR spectra, the absorption band for liquid water is visible at $1640\,\mathrm{cm}^{-1}$.

In contrast, this water peak is not present in the NEMS-IR-TD spectra, which are acquired in vacuum. The grey dashed line indicates the switching point of the QCL modules around $1400\,\mathrm{cm}^{-1}$, as described in the previous chapter.

Due to their semi-volatility in vacuum, both caffeine and theobromine undergo sublimation and desorb from the NEMS resonator over time. The NEMS-IR-TD setup allows for the simultaneous monitoring of the process by a combination of photothermal IR spectroscopy, shown in Figure 6.4a&b, and thermogravimetric analysis, shown in Figure 6.4c&d. Assuming an approximately homogeneous mass distribution on the resonator surface, the additional loaded mass of caffeine and theobromine can be calculated from the recorded resonance frequency [157] (see Equation 2.25). Due to the chip being cooled below room temperature for the caffeine measurements, residual contaminants present in the measurement chamber start to adsorb on the resonators' surface while caffeine is desorbing. This process has two effects: a drop in frequency due to additional mass and the appearance of new peaks in the heat map. As a result, the resonance frequency starts to decrease again after reaching a peak as shown in Figure 6.4c. These

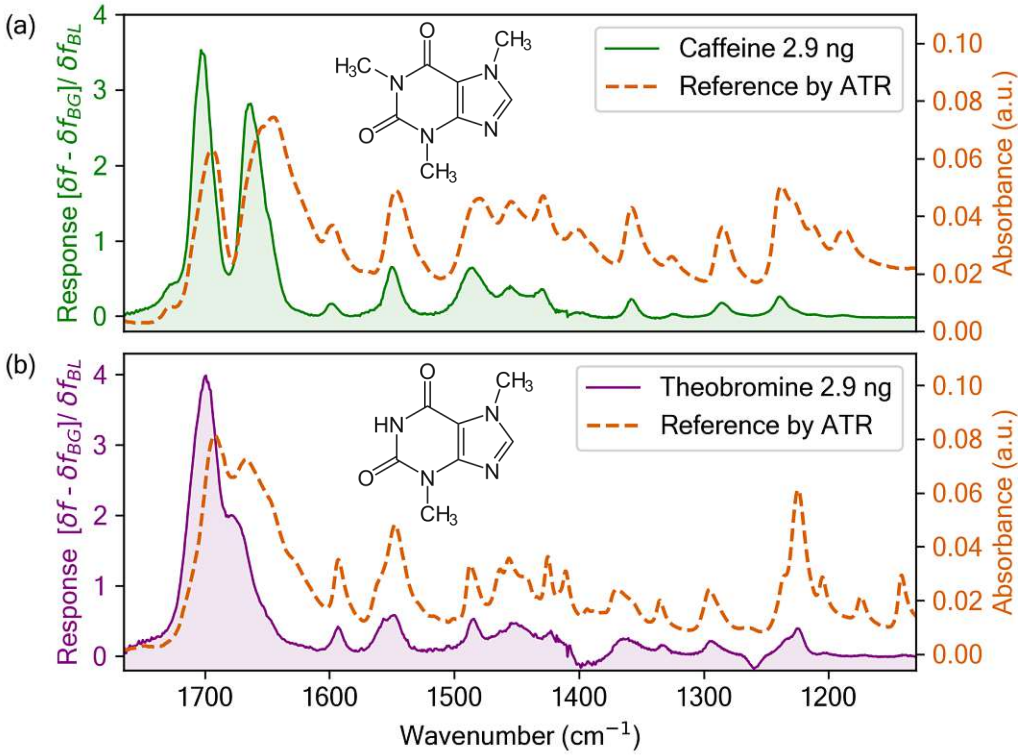

Fig. 6.3: NEMS-IR spectra for (**a**) caffeine and (**b**) theobromine sampled on a 1000 µm sized trampoline resonator and compared to reference spectra obtained from the crystalline powder by ATR-FTIR (PerkinElmer) with 0.5 cm^{-1} resolution. Figure and caption adapted from [7] - Copyright 2023 under a CC BY 4.0 license.

spectral peaks appearing at 1730 cm^{-1}, 1460 cm^{-1}, 1380 cm^{-1}, and 1278 cm^{-1} match with the condensated hydrocarbon-groups observed in the cooling experiment described in the previous chapter.

In contrast to the low temperature and fast desorption of caffeine, theobromine had to be heated to a much higher temperature in order to trigger desorption. At these higher temperatures, no adsorption of residual contaminants could be observed. This can be seen in Figure 6.4d by a constant rise of the resonance frequency up to a plateau where all theobromine has been fully desorbed. From these desorption experiments, the limit of detection (LoD) for caffeine and theobromine can be calculated by combining the spectral- and mass data. The response of the strongest spectral peak for caffeine $\nu(C{=}O)_{caf}$ at 1705 cm^{-1} and theobromine $\nu(C{=}O)_{tb}$ at 1700 cm^{-1} were used for the determination of the LoD as indicated by the blue-dashed lines in Figure 6.4a&b. As seen in Figure 6.4e&f, the system shows a linear response for both analytes over the entire mass range studied, which spans over three orders of magnitude. Combining the noise level from the standard deviation σ obtained from five subsequent sweeps

with the fitted linear response R, one can derive the limit-of-detection LoD $= 3\sigma/R \approx$ 5.7 pg and 4.9 pg ($\approx$ 30 fmol) for caffeine and theobromine, respectively. In terms of the absolute mass collected on the sensor surface, this detection limit is one to two orders of magnitude lower than direct deposition GC-FTIR techniques using cryogenically cooled IR detectors [18, 25].

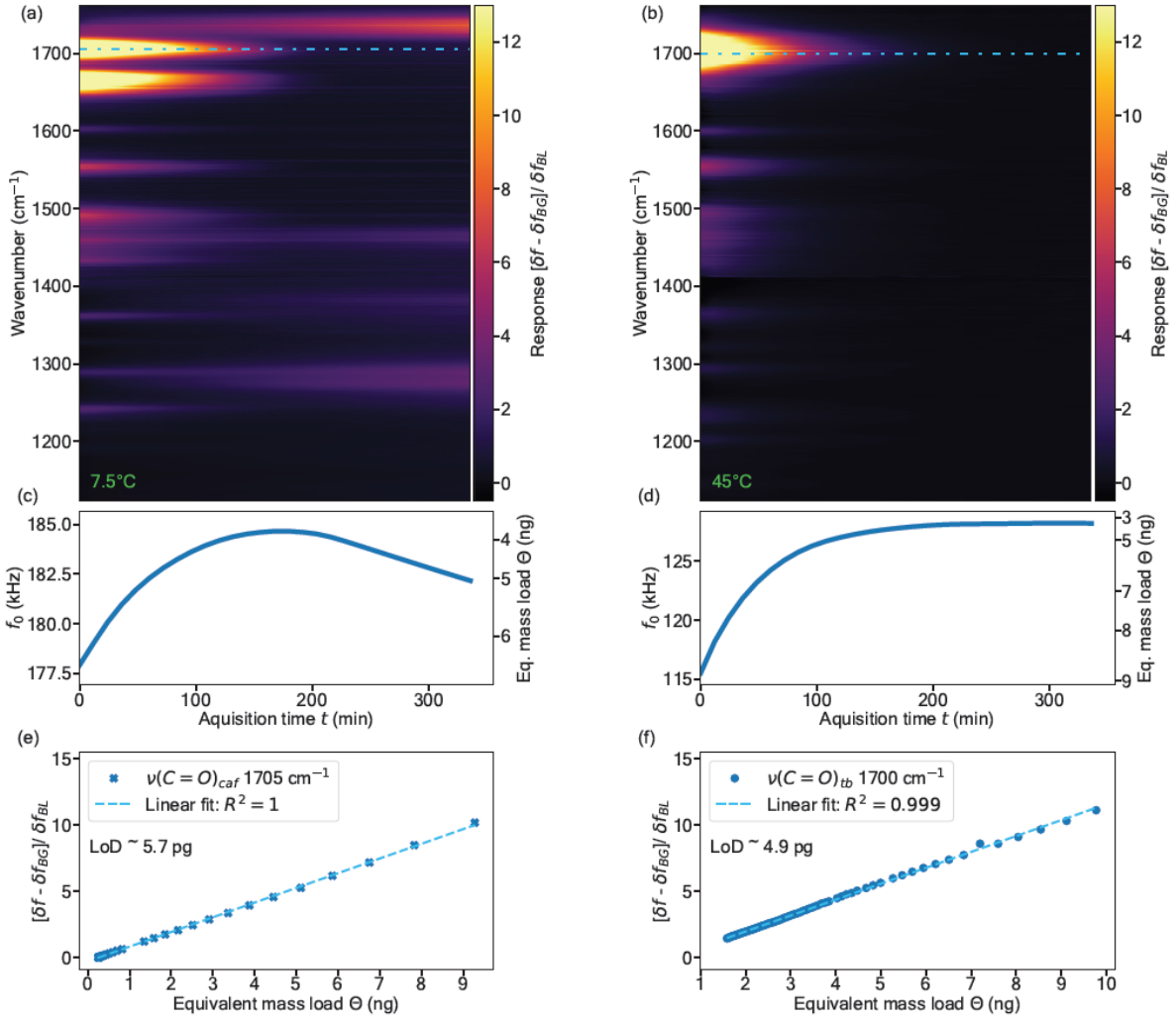

Fig. 6.4: Multidimensional analysis of isothermal desorption in vacuum. Spectro-temporal data for (**a**) caffeine and (**b**) theobromine during isothermal desorption from two similar 500 µm sized trampoline resonators at 7.5 °C and 45 °C, respectively, and the corresponding mass data of (**c**) caffeine and (**d**) theobromine. IR response for (**e**) caffeine and (**f**) theobromine as a function of mass load evaluated at 1705 cm^{-1} and 1700 cm^{-1}, as indicated by the dashed lines in (**a**) & (**b**), respectively. For a direct comparison, the LoD analysis was performed in a different experiment than (**a** – **d**) from a single 1000 µm sized trampoline resonator. Figure adapted from [7] - Copyright 2023 under a CC BY 4.0 license.

6.4 Analysis of the desorption dynamics

The dynamic of the desorption process is studied with NEMS-IR-TD by isothermal and dynamic thermogravimetric analysis (TGA) as presented in Figure 6.5. Assuming a single desorption process, the desorption rate $r(t,T)$ as a function of time t and temperature T can be described by the *Arrhenius* equation, which, for the application of desorption dynamics is referred as *Polanyi–Wigner* equation [158, 145, 159]

$$r(t,T) = -\frac{\partial \Theta}{\partial t} = v_d \exp\left(-\frac{E_d}{RT}\right)\Theta^n = k_d(T)\Theta^n \tag{6.1}$$

with the gas constant R, the activation energy of desorption E_d , the reaction rate constant k_d , and the relative surface coverage Θ^n for a desorption kinetic order n. The pre-factor v_d is often referred to as *frequency factor*, which describes the rate at which reactant molecules collide and have the potential to undergo a chemical reaction [158]. Assuming no dissociation or recombination for the desorption processes observed, the surface coverage/mass loss over time can be described by a first-order kinetic ($n = 1$)

$$\Theta^1(t) = \Theta_0 \exp\left(-k_d(T)/t\right) + \alpha t, \tag{6.2}$$

with assigning the initial mass-load as Θ_0 and a linear condensation correction factor α. In Figure 6.5(a&b), the isothermal desorption at various temperatures is evaluated for both caffeine and theobromine. As seen in Figure 6.5a&b , the first-degree desorption model is a good approximation to describe the desorption process. The corresponding sample mass data is fitted with the third-order Taylor expansion of the mass response to extract the temperature-specific desorption rate constants. Plotting the resulting desorption rate constants k_d versus the temperature according to

$$\ln(k_d(T)) = \ln(v_d) - \frac{E_d}{R}\frac{1}{T} \tag{6.3}$$

allows the extraction of the analyte-specific activation energy of desorption E_d and the pre-exponential frequency factor v_d, as shown in Figure 6.5(c). The values obtained for E_d are comparable to the sublimation enthalpy values for caffeine and other xanthins measured in former studies ranging from 106 kJ mol^{-1} to 132 kJ mol^{-1} [160].

In addition to the isothermal TGA, the desorption process can further be studied with dynamic TGA (also familiar as temperature-programmed desorption TPD), where the temperature is increased at a constant rate. Here, this is achieved by a programmed step-wise increase of the set temperature with a rate of 0.1 °C s^{-1} ranging from 5 °C to

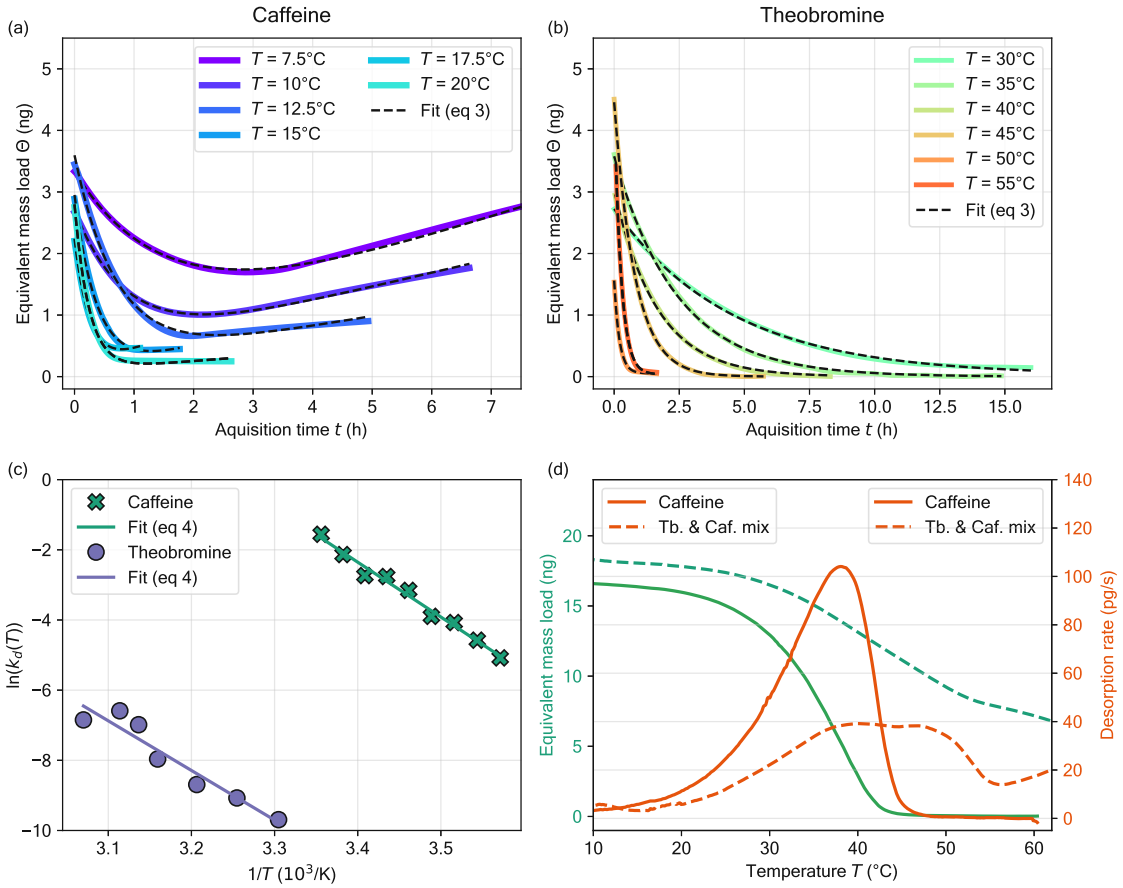

Fig. 6.5: Isothermal and dynamic thermogravimetric analysis (TGA). Isothermal desorption at various temperatures of (**a**) caffeine and (**b**) theobromine with an initial mass-load of ≈ 4.5 ng. The mass load data was fitted with the first-order desorption model using Equation 6.2. (**c**) Corresponding *Arrhenius* plots for caffeine and theobromine fitted by Equation 6.3 with resulting activation energies and frequency factors of $E_d = 130(6)\,\mathrm{kJ\,mol^{-1}}$ & $\nu_d = 1.14 \times 10^{22}\,\mathrm{s^{-1}}$ for caffeine and $E_d = 118(15)\,\mathrm{kJ\,mol^{-1}}$ & $\nu_d = 1.12 \times 10^{16}\,\mathrm{s^{-1}}$ for theobromine. (**d**) Dynamic thermogravimetric spectrum for a temperature ramp of $0.1\,\mathrm{K\,s^{-1}}$ of caffeine and a binary mixture of caffeine and theobromine. Figure adapted from [7] - Copyright 2023 under a CC BY 4.0 license.

70 °C. To compensate for the change of the resonance frequency due to the temperature, a blank temperature ramp of the empty chip was recorded after the analyte was fully desorbed. This was ensured by measuring a NEMS-IR spectrum before and after the temperature ramp. The mass-load was then calculated from a third-order Taylor expansion of Equation 2.21, while using $f_0(T)$ from the blank ramp. In the final step, the desorption rate was calculated from the mass-loss between subsequent temperature steps of 0.1 °C.

Figure 6.5d presents the desorption spectrum of caffeine and a binary mixture of caffeine and theobromine. The shape of the desorption rate peak of caffeine looks as expected

for a desorption process following first-order kinetics [161]. The desorption rate of the mixture shows two peaks, where the second peak is not fully developed at the maximum temperature achievable with the thermo-electric element and just starts to rise. The peak around 40 °C is due to the selective desorption of the more volatile caffeine. Clearly, the peak shape and amplitude are altered by mixing caffeine with theobromine. The desorption process becomes more complex when multiple molecules are involved. Similar alterations of desorption profiles have also been observed for other binary mixtures [162].

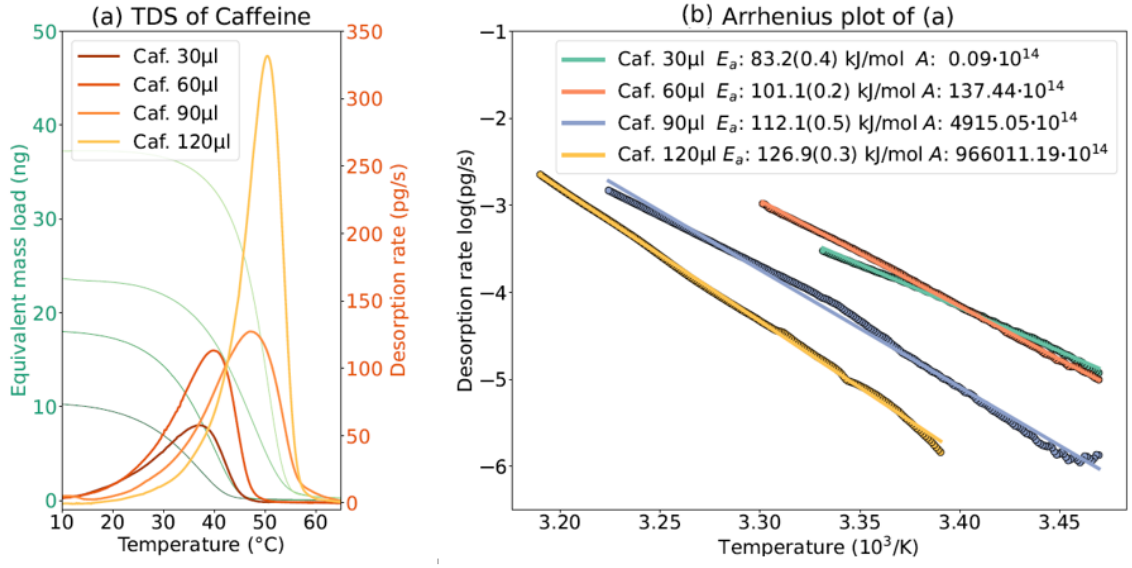

Fig. 6.6: Dynamic TGA for varying initial mass-loads of caffeine. (a) TPD spectra of the desorption rate showing a shift to higher peak temperatures for increased mass-loads and (b) fitted activation energy E_d and frequency factor ν_d extracted from (a).

In addition to the dynamic TGA of single and mixed compounds, the impact of the initial mass load on the desorption process can be analyzed. Figure 6.6a presents the TPD spectra obtained for different initial mass-loads of caffeine. The peak temperature is significantly shifted towards higher values scaling with the initial mass-load, which ranges from approximately 10 ng to 40 ng. This trend can also be seen by the increase in activation energies and frequency factors in Figure 6.6b. Such an increase can be explained by the higher possibility for interaction between adjacent caffeine molecules, which due to the increase of *Van der Waals* forces and hydrogen bonding, lead to an increased activation energy of the desorption process. Likewise, the higher caffeine load on the same sampled spot reduces the initial possible desorption sites for stacked molecules, further contributing to this effect [163]. This matches well with the shift of desorption rate towards higher peak temperatures and significantly increased

frequency factors. The frequency factor reflects the rate of molecular collisions and other microscopic processes that must occur before a chemical reaction can take place [158]. Thus, the frequency factor is expected to increase with rising temperature due to more molecular collisions and greater kinetic energy before desorption occurs, as can be observed in Figure 6.6. In contrast, the lower ν_v for theobromine in Figure 6.5c means that theobromine is less likely to successfully undergo desorption for the same given temperature, even if the activation energy is similar to caffeine.

6.5 NEMS-IR-TD with *in situ* sample separation

Disclaimer. The following formulations, application, interpretation of the singular value decomposition, and global analysis for the deconvolution of spectro-temporal data are attributed to Dr. Robert G. West.

The dynamic TGA data shows the capability of the NEMS-IR-TD system to separate and extract single components out of a mixed sample by thermal desorption. This provides valuable insight into the composition of a complex sample and can help elucidate information such as the number of components in a mixture, as well as the chemical composition of these components when used in conjunction with IR. Due to their similarity in chemical structure, theobromine and caffeine exhibit similar IR spectra (see Figure 6.3). A major difference can be seen at higher wavenumbers, where theobromine contains only a single broad $\nu(\mathrm{C{=}O})_{tb}$ absorption peak at 1700 cm^{-1} compared to the double-peak of caffeine. As a result, there is significant overlap when analyzing the spectrum of a mixture of caffeine and theobromine. However, thanks to their distinct volatility and desorption rates, the two spectrally similar compounds can easily be separated physically for analysis.
In addition to dynamic TGA, with NEMS-IR-TD, the desorption dynamics of complex samples can be studied by combining isothermal desorption and continuous chemical analysis with IR spectroscopy. Figure 6.7a presents the spectro-temporal heat map of a binary mixture of caffeine and theobromine recorded at two fixed temperatures. The corresponding mass data is shown in Figure 6.7b, proportional to the change in resonance frequency of the NEMS resonator. The large frequency step, when the temperature is increased from 10 °C to 50 °C, is due to the temperature responsivity of the resonator. At 10 °C, the IR and the mass data indicate the total desorption of caffeine over time. The remaining theobromine can also be completely desorbed when the temperature is increased to 50 °C.

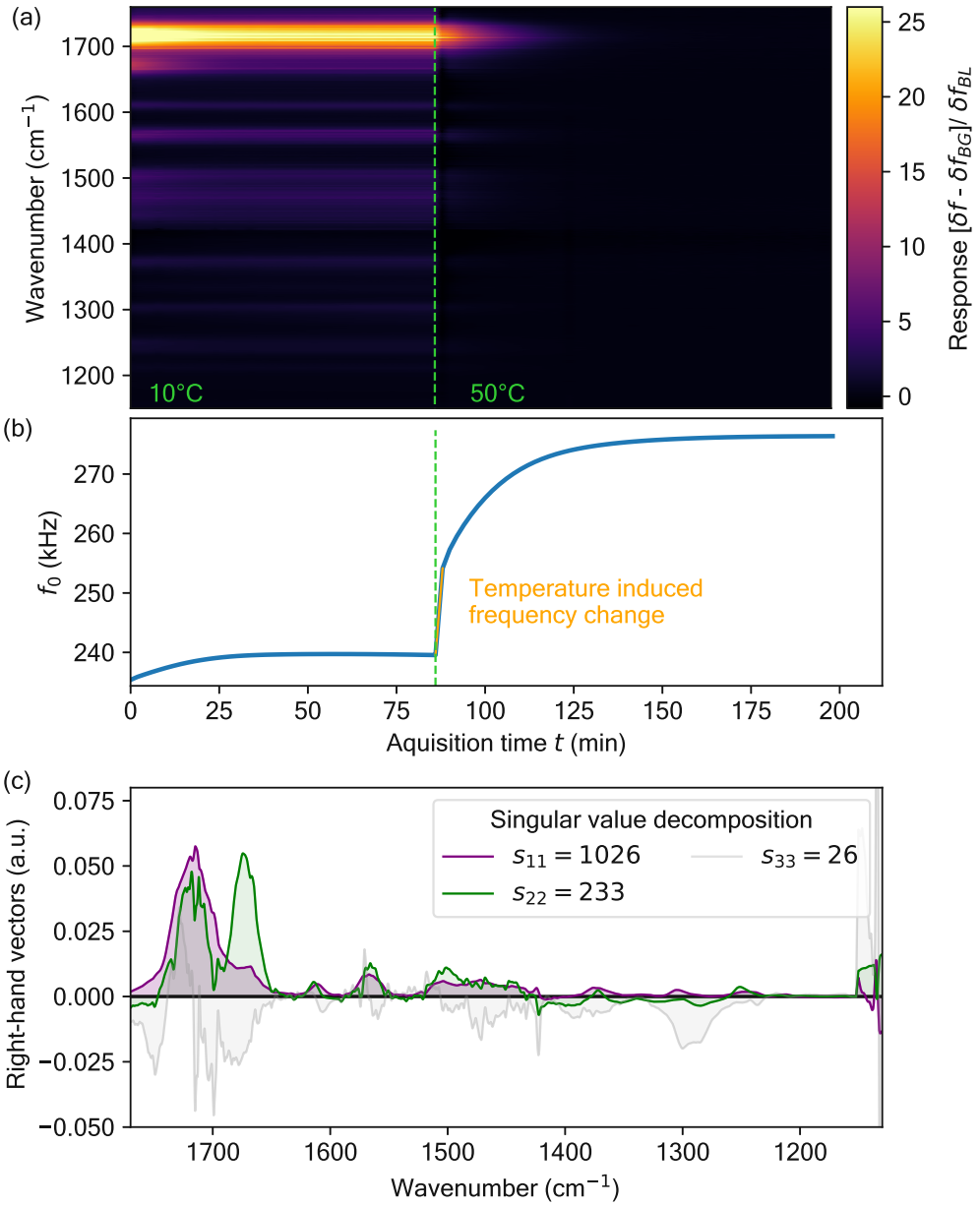

Fig. 6.7: Isothermal separation and single value decomposition. (a) Spectro-temporal NEMS-IR data of a binary mixture of caffeine and theobromine and (b) corresponding NEMS-TGA data. The green dashed line indicates the temperature change from 10 °C and 50 °C. (c) Separated spectra at 10 °C from the first three right-hand singular vectors with singular values from SVD. Figure adapted from [7] - Copyright 2023 under a CC BY 4.0 license.

Unraveling the intrinsic spectral and dynamical features of mixtures requires an analysis that can reduce the dimensionality of the data into a few relevant, distinguishable components associated with each species. Similar to spectral analysis techniques of transient spectroscopy, we proceed with two informative analysis procedures: singular-value decomposition (SVD) and global analysis, which is informed by the SVD.

First, we determine the number of components contributing significantly to the spectra in the data set as a whole by the SVD. The SVD is a non-subjective factorization that can be performed on any data set where the spectra vary with some independent parameter such as time [152, 164, 153, 154] or pH [165]. In this top-down mathematical procedure, the singular values indicate a component's strength in the data set, which sharply declines in further components. Those components with lower values contribute less to the overall response and, likewise, have noisy, unstructured right and left-hand singular vectors. These vectors represent the spectra and their associated dynamical traces, respectively.

Based upon the number of components demonstrating structured singular vectors, SVD allows for choosing a minimum amount of components that sufficiently represent the entire spectro-temporal response. For caffeine and theobromine in a mixture at 10 °C, four components were sufficient. The right-hand singular vectors of the data set for caffeine and theobromine in mixture at 10 °C are shown in Figure 6.7c, with the exception of the fourth, structureless component (see Supporting Figure S8 [7]). SVD separates the theobromine-dominant (s_{11}) and caffeine-dominant (s_{22}) desorption contributions and properly factors an inverted spectral feature (s_{33}), suspected to be condensing contaminants. The singular values, indicated in the legend of Figure 6.7c, show that, for the duration of the experiment, the primary contribution to the total resonance frequency shift was theobromine. Caffeine contributes less due to its short lifetime, as well as the contaminant due to the time limitation of the experiment. The associated left-hand singular vectors (Supporting Figure S8 [7]) can be fitted to estimate the rate of change of each component.

6.6 Application of global analysis for deconvolution of spectro-temporal data

By the SVD, we obtain the number of primary contributing components and their general spectral form, and this informs our second method of analysis, Global analysis, a multi-dimensional fitting procedure. In this bottom-up approach, shown in Figure 6.8, we can distinguish trends in these spectro-temporal maps, where first-order, exponential trends are fitted across the whole spectrum. This method is widely used to identify decaying transient species in ultrafast spectroscopy only after performing the SVD [153, 155]. Whereas, instead of analyzing the transient dynamics of populated electronic excited states, the evolution of transitory resonance frequency shifts during desorption or adsorption of IR-active species is evaluated.

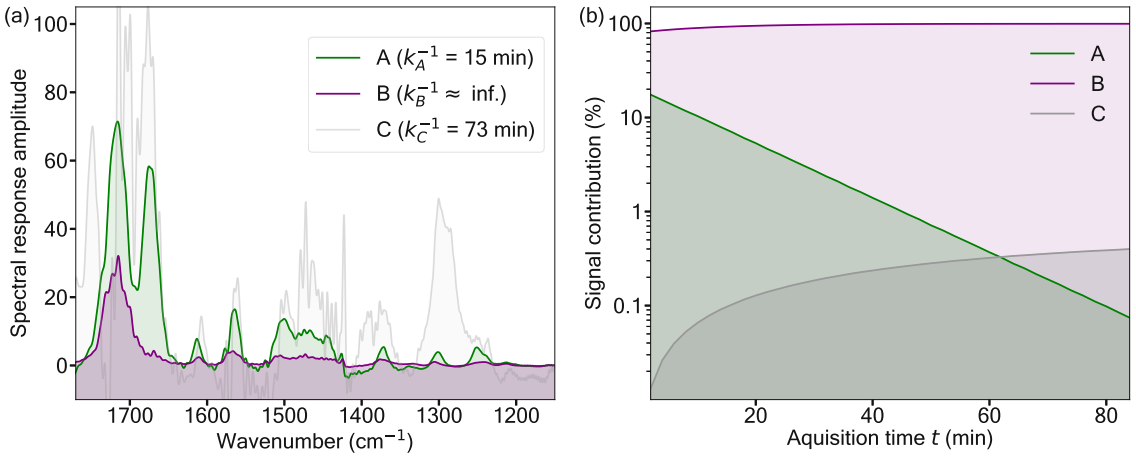

Fig. 6.8: Separation example by global analysis. (a) Spectral response amplitudes (or Evolution-Associated Spectra) from global analysis applying a sequential model on the spectro-temporal data at 10 °C in Figure 6.7 up to the temperature change at 86 min. (b) Corresponding relative contributions of the spectra in (a) to the total response. The superposition of the outer product of each spectrum in (a) and corresponding traces in (b) reproduce a fit to the spectro-temporal data in Figure 6.7. Figure and caption adapted from [7] - Copyright 2023 under a CC BY 4.0 license.

The *Ultrafast Spectroscopy Modeling Toolbox* from von Thor and colleagues [153] was chosen to showcase the potential of NEMS-IR-TD upon fully utilizing the information the method provides. The number of components required for the analysis of the caffeine/theobromine mixture at 10 °C was informed by dynamic TGA and SVD. These so-called evolution-associated spectra reveal three distinct spectral trends arising in succession, beginning with caffeine (residues shown in Supporting Figure S9 [7]). The first two components, decaying with a rate of $k_A^{-1} = 15$ min and $k_B^{-1} = \text{inf.}$ are primarily characteristic spectral features of caffeine (A) and theobromine (B). The final, slowly-rising component, with the same peaks as observed in Figure 6.5a at later times, identifies the spectrum of volatile hydrocarbon condensation (C), which monotonically rises throughout the time of the experiment.

As the SVD reveals distinct components according to their contribution to the NEMS-IR-TD data, Global analysis yields the evolution of distinct and identifiable spectral signatures according to a sequential model. However, the exact spectra of the individual adsorbing species and their rates can be obtained by target analysis if the sorption reaction scheme or model is known. Such an attempt to obtain the so-called species-associated spectra is shown in Supporting Figure S9 ([7]) according to a mix of sequential and parallel processes. Therefore, NEMS-IR-TD data allows for a full range of spectral analyses for species separation on the femtomolar scale.

6.7 Conclusion and outlook

With NEMS-IR-TD, we present a novel method for spectral and thermogravimetric analysis of single and mixed compounds with femtomole sensitivity. Testing this method with two xanthins exhibiting similar IR spectra but distinct vapor pressures showed the capability of *in situ* separation by isothermal desorption as well as by spectral analyses recorded with a single device. Due to the rising capabilities of chemometrics based on dedicated algorithms up to artificial intelligence [166, 167], it is expected that mixtures with similar vapor pressures can still be identified. Besides the spectral deconvolution, one can further adjust the temperature to enlarge the acquisition/desorption time and, thereby, the number of data points in which trends can be picked up by global analysis. However, further studies focusing on the separation limitations still need to be conducted.

Due to the low sampling efficiency of the aerosol setup to the time of the experiments, only a small fraction of the analyte could be used for the analysis. This limit could be overcome by changing the deposition methods to, e.g., low-pressure direct deposition [25], electrospray and molecular beam deposition [168], or selective capturing by surface functionalization, which could allow for trace analysis with single-molecule sensitivity as the ultimate limit [60].

The temperature range of 0 °C to 80 °C provided by the thermo-electric element has been relatively small. Thus, the maximum temperature was not high enough to complete the temperature-programmed desorption of theobromine, which has a relatively low vapor pressure. An enhanced temperature range would increase the range of samples that can be analyzed. Lower temperatures could allow the capturing and retention of volatile compounds, such as volatile organic compounds (VOCs) [169], while the ability to reach higher temperatures could allow the desorption of compounds with lower volatility. The current prototype for commercialization of the NEMS-IR technique by Invisible-Light Labs is therefore equipped with a stronger element enabling a range of −15 °C to 100 °C. Singular value decomposition and global analysis of the time-dependent information provided by NEMS-IR-TD readily yield species-specific information from the isothermal desorption processes (Figure 6.7 & Figure 6.8); whereby, identifiable spectral signatures of individual species are extracted from the convoluted frequency response to IR absorption over time. Their spectral signatures are temporally separated by their interaction with the adsorbent or other adsorbates. This opens the possibility for tailoring the surface of the NEMS resonator for selective species adsorption as well as surface functionalization studies.

Theobromine desorbed at a much slower rate than caffeine, individually and in the mixture, allowing its spectral features to be differentiated from that of caffeines. In view of this, dynamic TGA and SVD alone demonstrate a vast utility. Not only does this combination provide the characteristic spectral signatures and the number of chemical species present, but an inversion of the spectrum distinguishes adsorbing species from the desorbing species. Additionally, the SVD reveals the relative contributions of each component to the total frequency shift. Once a sufficient number of components is determined by SVD, a more intuitive analysis, such as global analysis and target analysis, can be applied. First-order global analysis in Figure 6.8 reveals the evolution of three distinct spectral signatures and their associated dynamic trends. An in-depth global analysis of the desorption data for caffeine under different temperatures indicated, that this technique is even able to distinguish subspecies spectra of caffeine isomers and how their contribution changes with temperature (see Supporting Figure S10 [7]).

To our knowledge, this is the first demonstration of utilizing a powerful and highly versatile tool to analyze disparate, simultaneously desorbing and adsorbing species. This substantiates the potential for future developments using global and target analyses, including higher-order [154] and even deep learning analyses [170], tailored to specific NEMS-IR-TD applications. Therefore, one can expect this technique to find a wide range of applications for the physicochemical characterization of complex samples in various fields, from environmental analysis to life sciences.

7 Advances in NEMS-IR and NEMS-FTIR spectroscopy

This chapter delves into the practical applications of NEMS-IR and NEMS-FTIR spectroscopy. Various sampling methods, including drop-casting and spin-coating, are explored. As part of the ongoing development for the commercial application of NEMS-FTIR spectroscopy, the latest prototype, named 'EMILIE™' by *Invisible-Light Labs GmbH*, is utilized to investigate the impact of FTIR scanning velocities on spectrum acquisition. Furthermore, the detection limits for theobromine in NEMS-FTIR spectroscopy are evaluated and compared with those of NEMS-IR spectroscopy using a QCL light source (see Section 6.3). These investigations employ a novel positive-feedback system for frequency tracking instead of a PLL (see Sec. 3.2). Subsequent to this characterization, the NEMS-FTIR system 'EMILIE™' undergoes testing for various applications, including the analysis of spin-coated polymers compared to conventional transmission spectroscopy and the bulk chemical analysis of environmental airborne particles.

7.1 NEMS-IR spectroscopy of drop-casted proteins

Following one of the initial goals of this project to enable label-free detection of proteins, the NEMS-IR system V3 was tested for the identification and quantitation of bovine serum albumin (BSA). BSA is a common protein extracted from bovine blood serum and is often used as an analytical standard for calibrating laboratory devices. Typically, BSA is sampled and measured for varying concentrations solved in a phosphate-buffered saline solution (PBS).

Sample preparation. This approach was tested for sampling with the aerosol setup, which, however, resulted in a strong load of the crystallized PBS salts on the resonator compared to the low concentration of BSA. Therefore, the sampling of BSA by drop-casting was tested. To remove the PBS salt from the resonator, the surface was treated with a solution of AnteoBind™ (Biosensor A-PLSC010-10). According to the manufacturer, this substance functionalizes oxidic surfaces to enable a strong binding of proteins such as BSA. After incubation of the BSA solution, the salt can be rinsed of the chip by Milli-Q water. For the functionalization, a drop of 10 µL AnteoBind™ was drop-casted on a bare Si_xN_y 1000 µm squared and unperforated resonator, incubated for 45 min, and rinsed of twice by Milli-Q water. After functionalization, the resonators were incubated with a BSA solution by drop-casting 10 µL by several dilutions 8 µg mL^{-1}, 16 µg mL^{-1}, 41 µg mL^{-1}, 83 µg mL^{-1} and 164 µg mL^{-1}.

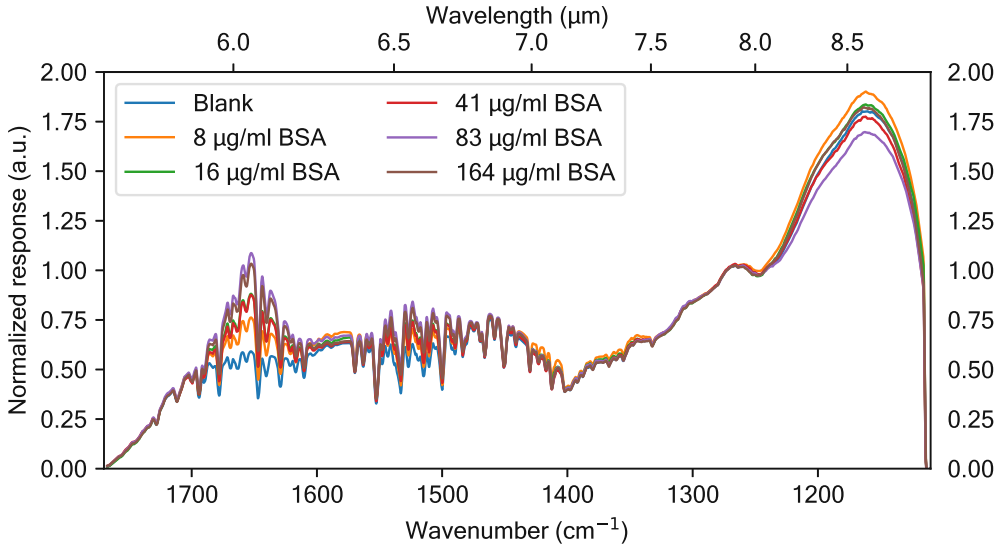

Fig. 7.1: Average response for different BSA concentrations normalized to a spectral feature of the QCL module at 1275 cm^{-1}.

The stock solution was prepared and diluted by a PBS buffer (pH 7.4) and incubated for approximately 30 min. To remove the PBS salt, the resonators are rinsed twice with Milli-Q water. Six replicates were prepared for each BSA concentration. To verify the effect of the AnteoBind™ activation agent, each BSA standard was additionally drop-casted on a separate, untreated resonator and incubated for 30 min. Six blank resonators were prepared by incubating with BSA-free PBS buffer following the same procedure.

Results & discussion. Figure 7.1 presents the average normalized spectra obtained from five different concentrations of BSA. To avoid the suppression of vibrational modes in the range of the Si_xN_y peak, the normalization was done at a power feature of the QCL at 1275 cm^{-1}, which does not inherit a vibrational mode of BSA. With increasing BSA concentration, there is a clear trend towards increased signal in the Amide I&II region, which for BSA, is expected at 1656 cm^{-1} and 1545 cm^{-1} [171]. The signal saturates for the highest two concentrations used.

Figure 7.2 shows the post-processed responses for different concentrations. As applied in previous chapters, the power profile of the QCL is corrected through the division of the bare Si_xN_y spectrum. Since the spectra of the PBS-treated samples were identical to those of a bare Si_xN_y resonator, the subtraction of the blank did not alter the result. The main contributions to the signal are the Amide I&II bands with a maximum response slightly shifted to 1660 cm^{-1} and 1535 cm^{-1}. Due to the dry environment of BSA leading to a partial reformation of the BSA native structure, a shift of the Amide peak positions can be expected [172, 173]. Further, the adsorption of BSA on the resonators' native

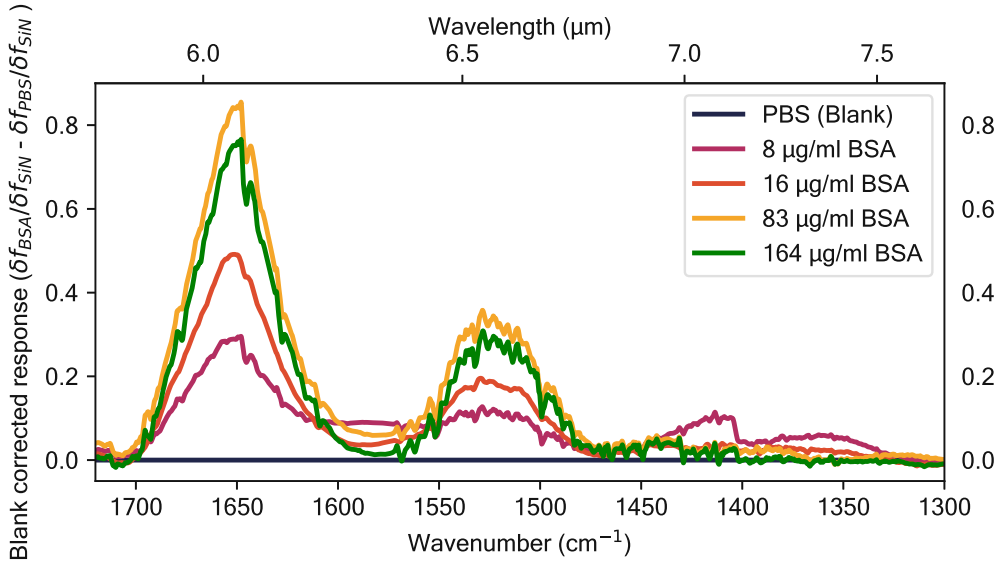

Fig. 7.2: Normalized response for different concentrations of BSA. In addition, the spectra are divided through the spectrum of bare Si_xN_y to account for the power variations of the QCL.

oxide surface can cause the appearance of a small amount of unfolded β-regions in the secondary structure [174]. These effects additionally contribute to the shift and altered peak intensities. For some concentrations, one can observe broad peaks in the range of 1450 cm^{-1} to 1200 cm^{-1}, which could be attributed to BSA. However, due to the arbitrary normalization, a strong deviation down to a negative response in the lower spectral range was obtained.

In Figure 7.3, the performance of NAM-IR spectroscopy for the analysis of BSA was evaluated by plotting the peak response of Amide I&II as a function of the concentration. Clearly, the resonator seems to be saturated by BSA for concentrations above 50 µg mL^{-1}. This raised the question of how much BSA can actually bind to the available surface.

According to the functionality of AnteoBind™, one can expect the formation of a monolayer by BSA. One approach to determining the mass of BSA responsible for the signal involves examining the frequency response to the added mass. However, due to the deviation between different chips, the evaluation of mass load based on the resonance frequency shift was inconclusive. An alternative method for assessing the mass of BSA contributing to the signal is through the relative responsivity of the resonator to absorbed heat.

Including the irradiation from the QCL and the average scattering cross-section of the Amide I&II peak for BSA, we obtained an approximate mass in the range of 1-2 ng. This underlines the hypothesis that the resonators are already fully covered by a monolayer of BSA for small concentrations. This is consistent with the hydrodynamic diameter of

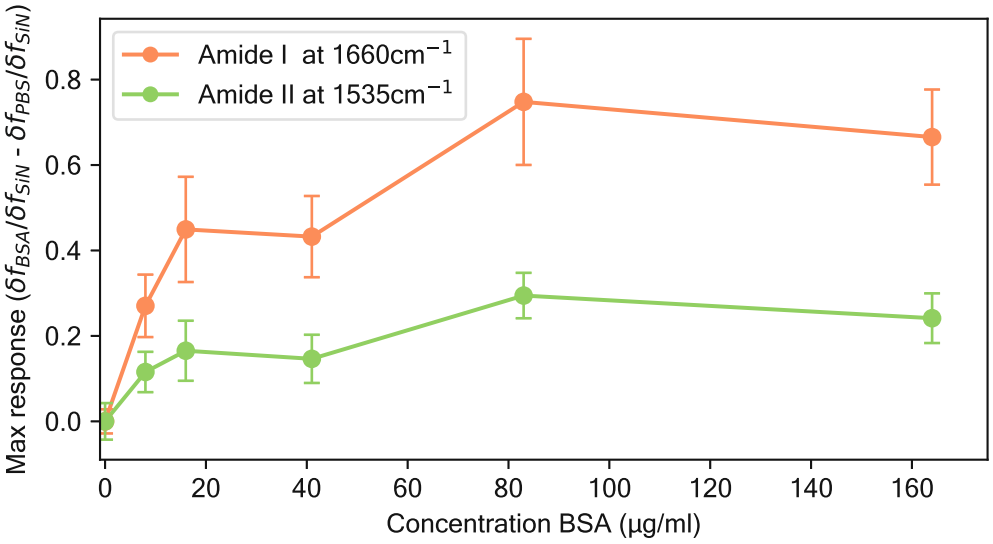

Fig. 7.3: Extracted peak response for the Amide I&II at 1660 cm^{-1} and 1540 cm^{-1} for different sampled concentrations of BSA. The response does not further increase for concentrations above 50 µg mL^{-1}, implying that a monolayer of BSA. saturates the resonator surface.

BSA at 7 nm [175], which limits the number of BSA molecules that can be immobilized on the 1 mm^2 resonator surface.

Conclusion. The study showed the general ability to drop-cast and analyze a few nanograms of proteins by NEMS-IR spectroscopy. A direct comparison of the BSA response on a resonator functionalized by AnteoBind™ to an unfunctionalized control sample revealed an almost identical signal. Hence, one can assume that BSA itself has sufficient unspecific adhesion to the resonators' surface without the necessity of functionalization. Besides this observation, no significant spectral response of the functionalization layer could be observed. This suggests that the silicon nitride surface may not be well-suited for functionalization by AnteoBind™, even with the presence of a native oxide layer. Alternatively, the resonators could be treated with oxygen plasma before the Anteobind-functionalization to ensure a fully oxidized layer.

7.2 Impact of scanning speed on the response in NEMS-FTIR spectroscopy

When combining the NEMS-IR technique to an FTIR, one has to consider the acquisition based on the detection of an interferogram. In commercial FTIR systems, the internal detector commonly relies on a deuterated lanthanum alpha alanine crystal doped with triglycine sulphate (DLATGS). This uncooled pyroelectric detector boasts a rapid re-

sponse time, facilitating the capture of multiple interferograms in seconds.
The acquisition speed is typically defined by the modulation frequency of a helium-neon or diode laser. The sinusoidal signal is used to precisely identify the mirror position and sampling points necessary for digitizing the interferogram. To fulfill the *Nyquist* sampling criteria, the minimum wavelength of the Fourier-transformed spectra is therefore limited by the wavelength of the probing laser. For a conventional HeNe laser with λ : 633 nm, the shortest wavelength of the Fourier-transformed spectrum is therefore limited to 1.26 µm. The scanning speed, often referred as 'scanner velocity', can be expressed as Fourier modulation frequency given by [85]

$$f_{mod} = 2v_{mirror}\tilde{\nu}\,, \tag{7.1}$$

where v_{mirror} is the mirror velocity in the interferometer and $\tilde{\nu}$ is the modulated wavenumber. By incorporating the wavenumber of the diode laser (633 nm $\hat{=}$ 15 797 cm^{-1}) and a typical modulation frequency (scanner velocity) of $f_{\mathrm{mod}} = 10$ kHz, one can compute the mirror velocity $v_{\mathrm{mirror}} \approx 0.3165\,\mathrm{cm\,s^{-1}}$. Conversely, this yields a modulation frequency of the wavenumber at the vibration mode of Si_xN_y around 835 cm^{-1} of approximately 529 Hz. Given the average thermal response time of the nanomechanical resonator, $\tau_{th} = 25$ ms, and related bandwidth of 40 Hz, this modulation is too fast to be detected.

Figure 7.4a presents the modulation frequency as a function of the wavenumber for different scanner velocities of the FTIR. In comparison to the resonator's bandwidth (highlighted by the green-shaded box), a scanner velocity of 200 Hz already induces modulations in the higher spectral regions beyond the thermal response time of the resonator. Consequently, only the slowest scanner velocity provided by the commercial FTIR with $f_{mod} = 100$ Hz can be fully resolved.

This can be observed in Figure 7.4b by the reduced NEMS-FTIR response for polystyrene beads measured with a 1 mm squared resonator. For highlighting the impact of scanner velocities, the spectra are normalized to the Si_xN_y peak. Transitioning from a step scan (brown-dashed line) to the slowest continuous mode already results in a notable decrease in response at higher wavenumbers. Therefore, opting for a lower scanner velocity or, ideally, utilizing the step scan mode is recommended to facilitate NEMS-FTIR spectroscopy.

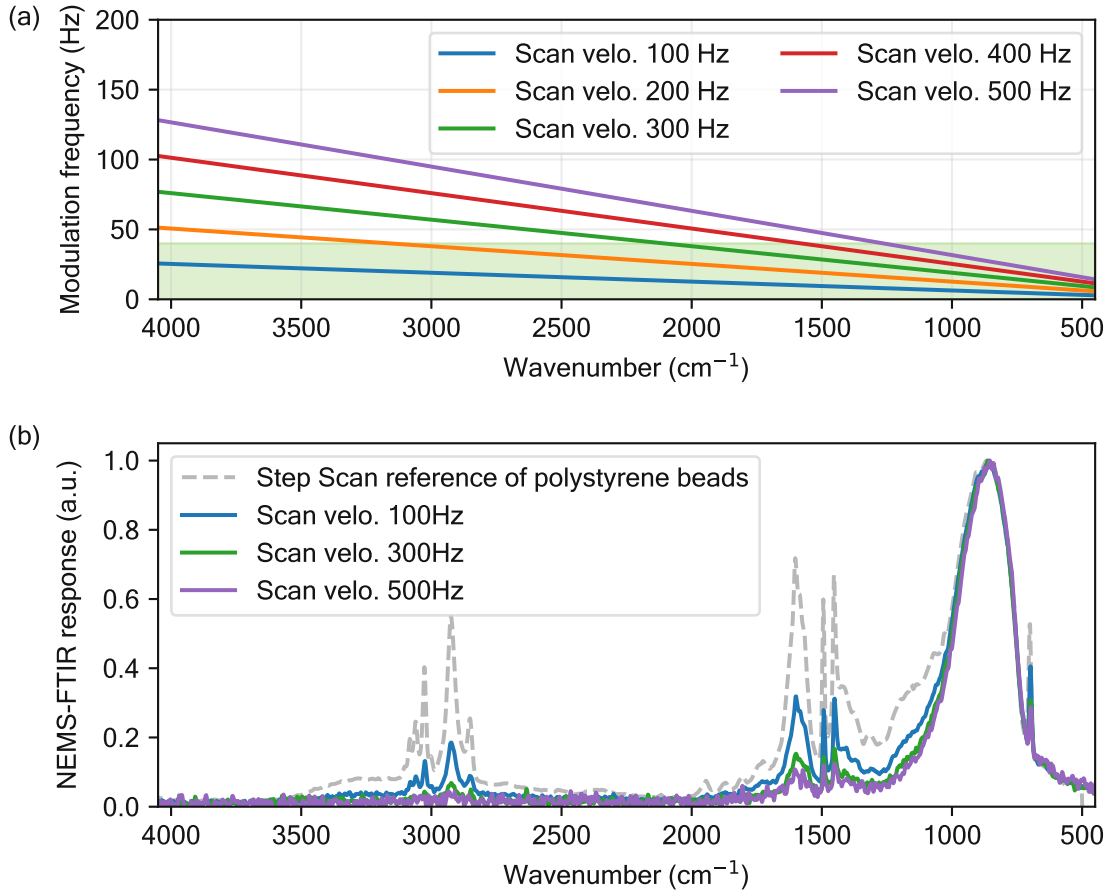

Fig. 7.4: (a) Visualization of modulation frequency as a function of the wavenumber for different scanner velocities. The green-shaded box resembles the accessible acquisition range within the average thermal response time/bandwidth of a 1 mm squared membrane resonator. (b) NEMS-FTIR spectrum of polystyrene beads sampled membrane resonator recorded with different scanner velocities compared to a step scan.

One alternative for achieving higher scanner velocities involves enhancing heat transfer on the resonator, such as through the addition of a metallic layer. Additional studies [6] have demonstrated that resonators equipped with an impedance-matched absorber consisting of 5 nm platinum can achieve a thermal response time of 4 ms (bandwidth of 250 Hz). Increasing the thickness of the layers further can substantially extend the thermal response time; however, this enhancement comes at the cost of reduced sensitivity (see Section 2.5).

7.3 Evaluation of detection limit in NEMS-FTIR spectroscopy

In this section, the detection limit of the NEMS-FTIR prototype EMILIE™ developed at *Invisible-Light Labs GmbH* is evaluated by employing the NEMS-IR-TD technique as demonstrated in the previous chapter. Figure 7.5 shows a picture of the prototype attached to the sample compartment of a commercial spectrometer and connected to the dedicated readout electronics based on a positive feedback scheme. Much like the upgraded setup, the NEMS-FTIR prototype comprises a purge box, a thermo-electric element to control the resonator and analyte temperature, and a molecular pump with an operational pressure of $< 1 \times 10^{-5}$ mbar.

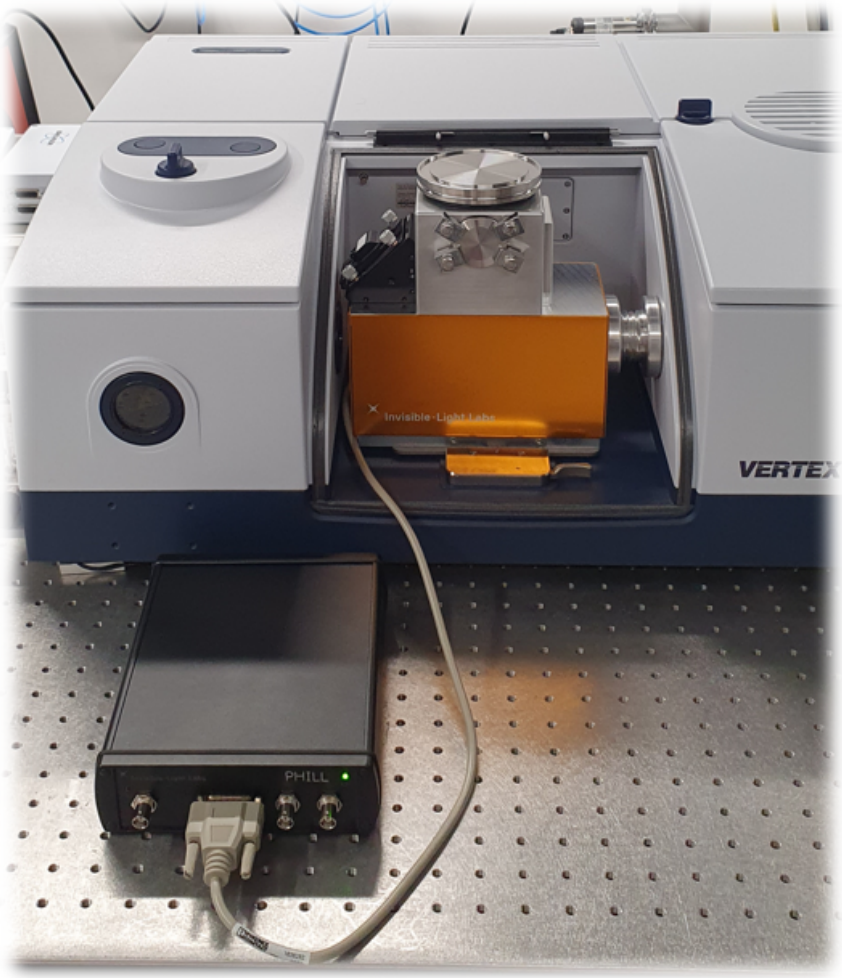

Fig. 7.5: Picture of the NEMS-FTIR prototype 'EMILIE™' and positive-feedback based readout electronics 'PHILL™', developed at *Invisible-Light Labs GmbH*. The system is fully integrated into the sample compartment of the commercial FTIR. It comprises a purge box for nitrogen and a kinetic mirror mount to adjust the focal point of the IR light.

Methods. To evaluate the detection limit, a decent amount of theobromine was sampled to a perforated membrane (M500 D6P3) using the improved aerosol setup. Due to the significantly increased acquisition time of a single spectrum based on a step scan (5 min) compared to the sweep in the QCL-based setup (26 s), the experiment was performed with repeated heating intervals/cycles instead of a continuous desorption mode. The spectra were recorded at a set-point temperature of 10 °C to minimize desorption of theobromine during spectra acquisition, followed by a heating cycle of 60 °C for 10 min for mass reduction by desorption. This way, it is possible to step-wise measure reduced amounts of theobromine from the same chip with consistent settings.

Results & discussion. Figure 7.6 presents the NEMS-FTIR spectra recorded for decreasing amounts of theobromine. The inset highlights the step-wise decreasing response of the strongest vibrational mode $\nu(\mathrm{C{=}O})_{tb}$ at 1700 cm^{-1}, which is used for the evaluation of the detection limit. Compared to the NEMS-IR analysis based on the QCL, which covers only the spectral range plotted in the inset, the NEMS-FTIR system enables a spectral acquisition over the full mid-IR range.

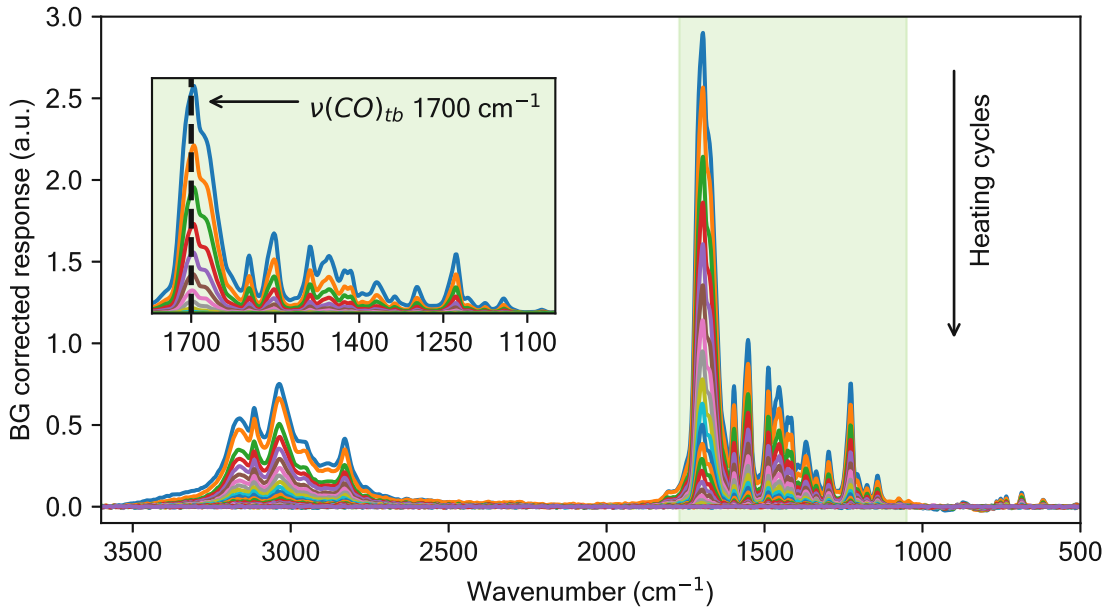

Fig. 7.6: Blank corrected NEMS-FTIR spectra for different mass loads of theobromine. The inset highlights the decreasing response of vibrational modes with increasing heating cycles. For the evaluation of the detection limit, the normalized response of the $\nu(\mathrm{C{=}O})_{tb}$ at 1700 cm^{-1} is used, indicated by the black-dashed lines.

The corresponding mass of theobromine on the resonator can be extracted from the resonance frequency at the time of the measurement, as depicted in Figure 7.7. To monitor the mass loss of theobromine due to desorption during spectra acquisition, the

resonance frequency was recorded before and after each measurement. As shown in Fig. 7.7a, no significant frequency change was measured, indicating that sample loss during the measurement can be excluded. The baseline frequency f_0 for converting to an equivalent mass-load by Equation 2.25 was taken from the average frequency of the last five heating intervals that showed no effect on the spectra or resonance frequency.

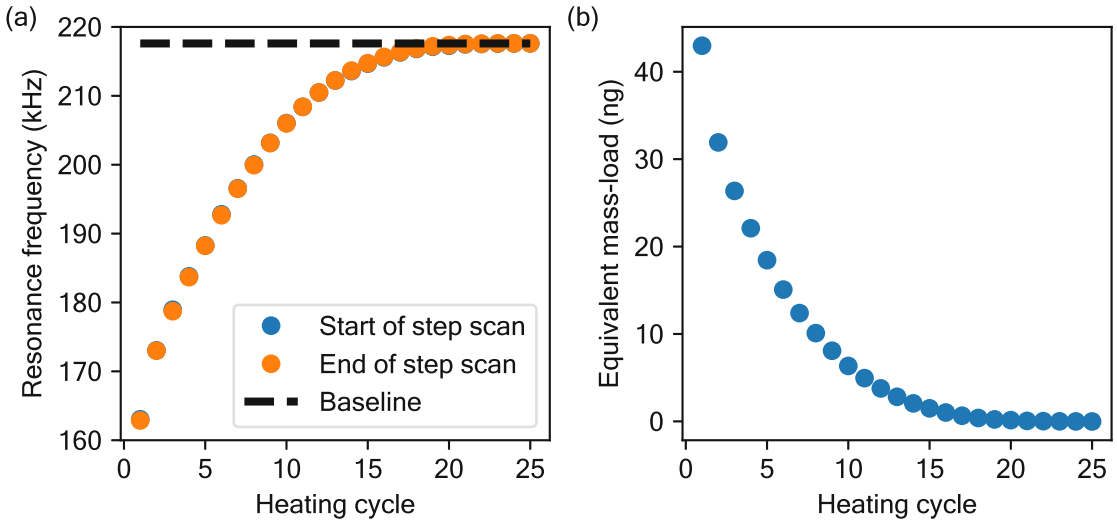

Fig. 7.7: (a) Resonance frequency after each heating cycle and equivalent mass-load of theobromine. The minimal frequency change between the start and end of each spectra acquisition shows, that no significant desorption of theobromine occurred during a measurement.

For the determination of the detection limit, the normalized response at $\nu(\mathrm{C{=}O})_{tb}$ is plotted as a function of the equivalent mass-load in nanogram, as presented in Figure 7.8. A fitting loop was applied to access the linear range of the resonator for theobromine. This loop performs a linear regression for increasing amounts of data points starting from the smallest response and compares the fit quality by the squared residual R^2. In this example, the resonator response diverges from linearity after iteration 15, corresponding to a mass-load of 10 ng. For significantly larger mass loads, the response diverges from linearity and approaches saturation. Similar to the limited response by an inner-filter effect in fluorescent microscopy, a stacked layer of theobromine reduces the light that adjacent lower layers can absorb.

For the final determination of the detection limit, the noise of the system needs to be quantified. Here, the noise is obtained from the standard deviation of individual blank spectra. The blank represents the spectra used for the background correction of the silicon nitride and residual organic compounds that did not desorb during the experiment. Figure 7.9(a) shows the blank spectra of five individual desorption runs of theobromine sampled from the same stock solution and performed on the same

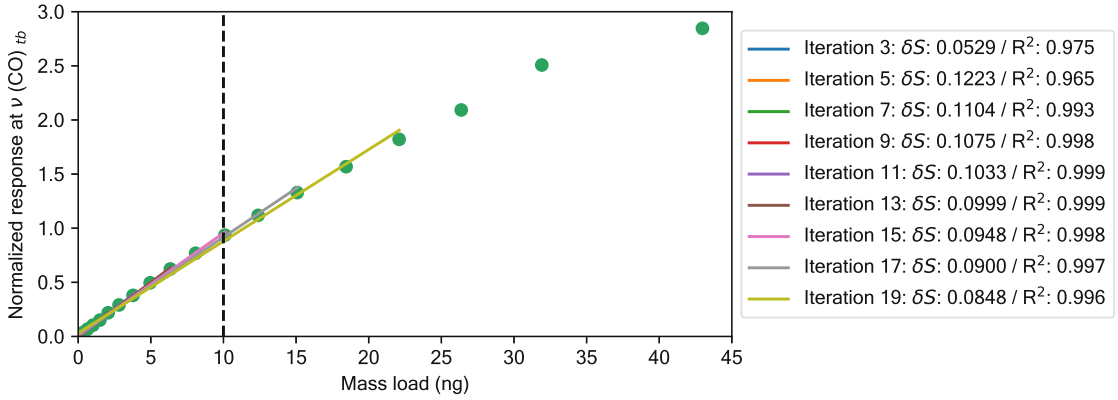

Fig. 7.8: Normalized NEMS-FTIR response for ν(C=O)$_{tb}$ as function of the equivalent mass-load by theobromine. The data points were step-wise linearly fitted to obtain the onset of divergence from a linear response. In this example, the response diverges after iteration 15, corresponding to a mass-load of 10 ng indicated by the black-dashed line. For significantly larger mass-loads, one can observe the approach of a saturation above 40 ng.

resonator design. The standard deviation at the evaluation point of the response is plotted in Figure 7.9(b) with a standard deviation of 0.0039. The limit of detection (LOD) is defined as the signal-to-noise ratio given by the standard deviation of the blank and response slope of the calibration, multiplied by a confidence factor of 3.2:

$$LOD = 3.2 \times \frac{0.0039}{0.0948} = 131\,\text{pg} \tag{7.2}$$

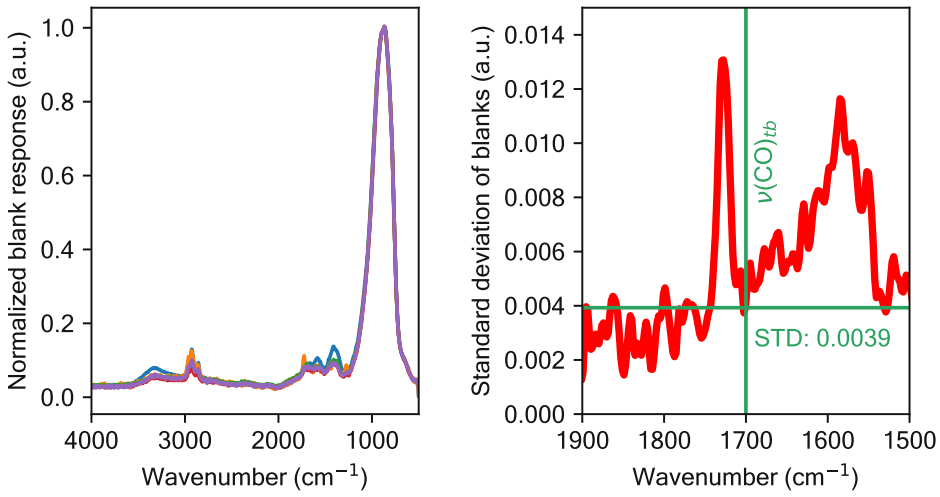

Fig. 7.9: Blank spectra of five individual desorption runs performed on the same resonator type. For the calculation of the detection limit, the standard deviation of five spectra was evaluated at 1700 cm^{-1} ν(C=O)$_{tb}$.

Conclusion. The detection limit obtained for theobromine resembles a 26x smaller LOD than the QCL-based NEMS-IR system evaluated in the previous chapter. This can be attributed to the significantly enhanced light intensity of the QCL over the FTIR. However, compared to conventional transmission FTIR spectroscopy, where often several milligrams of analyte are needed, this represents an improvement of sensitivity on the order of 10^6.

7.4 NEMS-FTIR spectroscopy of a spin-coated thin film

Former NAM-IR studies demonstrated the potential to apply NEMS-IR spectroscopy for spin-coated thin films of a polymer [59]. In the following section, the performance of the NEMS-FTIR prototype 'EMILIE™' is tested to analyze a polymer thin film compared to conventional FTIR spectroscopy.

Methods. In collaboration with the chemical department at TU Wien, a thin layer of approximately 17 nm polystyrene was spin-coated from solution onto a 1 mm squared membrane resonator. The resonator was then measured by NEMS-FTIR spectroscopy using a step scan mode and positive feedback configuration for frequency tracking.

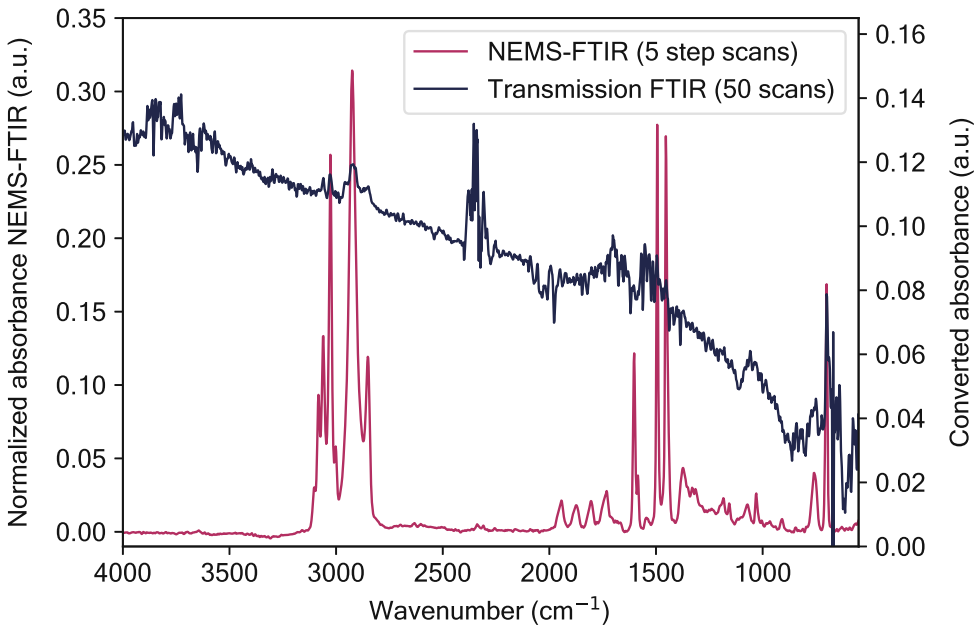

Fig. 7.10: Comparison of a spin-coated polystyrene film measured by NEMS-FTIR and classical transmission FTIR spectroscopy. The transmission is obtained through the same membrane resonator placed behind a 1 mm aperture in an aluminum plate.

Results & discussion. Figure 7.10 shows the spectrum obtained by NEMS-FTIR spectroscopy compared to a conventional transmission spectrum using the same FTIR with the in-built RT-DLaTGS detector. The transmission spectrum was recorded with a standard continuous mode with scanner velocity of 5 kHz. To ensure the transmission is measured through the resonator only, the chip was placed on the back of an aluminum plate with a 1 mm aperture.

The comparison clearly shows the high sensitivity of the NEMS-FTIR technique, where all spectral features of polystyrene can be obtained with a high signal-to-noise ratio. In contrast, despite the averaging of 50 Scans, only the strong spectral features in the region of 3250 cm^{-1} to 2750 cm^{-1} can be identified.

7.5 NEMS-FTIR spectroscopy of airborne particles

Analyzing ultra-fine airborne particles (UFP), characterized by their minute size and mass, presents a significant challenge in chemical analysis. UFPs, defined as particles with a diameter of less than 500 nanometers (referred to as PM0.5), demand specialized techniques for accurate examination. In contemporary methodologies, it is a common approach to gather UFPs on filters over periods ranging from several hours to an entire day. This extended collection time is necessary to collect a sufficient mass of particles for a subsequent analysis. This is typically followed by an intensive sample preparation to enable the identification of compounds by mass spectrometry. In contrast, the optimized resonators provide a convenient platform for the sampling and analysis of UFPs by NEMS-IR spectroscopy.

Methods. To facilitate UFP analysis by NEMS-FTIR spectroscopy, a mobile sampling setup was constructed and tested as part of a supervised bachelor thesis conducted by C. Leuschner [134]. Figure 7.11 shows a schematic illustration and a picture of the mobile setup at the university rooftop for field sampling of airborne particles. The setup mainly comprises a flow meter & pump powered by a battery featuring a 12 V DC output, the improved metal sampling chamber, and a PM0.5 particle filter at the air inlet. To provide a high capturing efficiency, only perforated membrane resonators of the type M500 D6P3 were used in this study.

Regarding the previous studies of sampling efficiency and detection limit for caffeine and theobromine in the NEMS-IR-TD study, one can estimate the sampling time necessary to capture sufficient particles for the analysis by NEMS-IR spectroscopy.

Figure 7.12 shows an estimation of the theoretical sampling time as a function of the ambient particle concentration for different particle sizes. For the estimation, the ac-

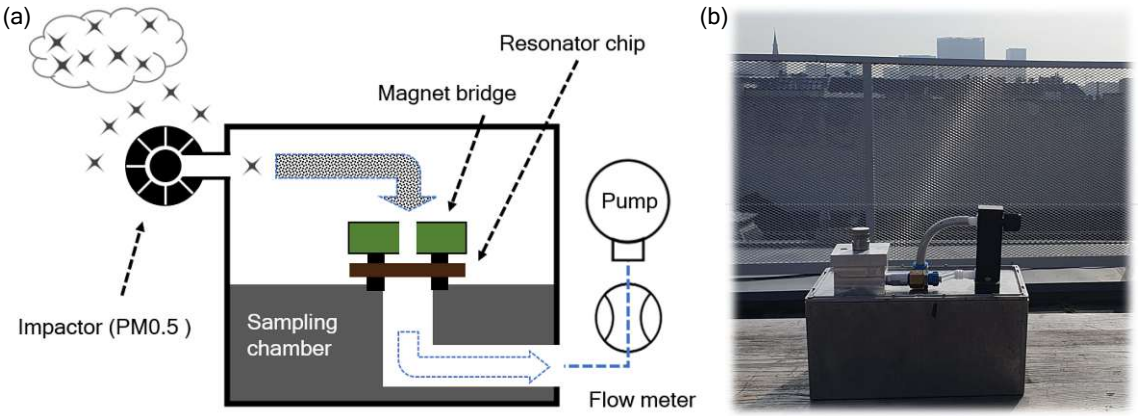

Fig. 7.11: (a) Schematic illustration and (b) picture of the mobile sampling setup comprising the improved metal sampling chamber, a flow meter & pump powered by a commercial power bank. The particle size is reduced to PM0.5 / UFPs by an impactor filter at the suction tube of the system.

cumulation of 1 ng material of spherical particles with a generic density of 1000 kg/m^3 and moderate sampling efficiency of 10 % was assumed. For all environmental aerosol experiments, the flow rate is defined by the PM0.5 particle filter to 1 L min^{-1}. The green-shaded box in Figure 7.2 highlights the sampling time and average particle concentration of 5500 cm^{-3} measured at the sampling site at the university rooftop in Vienna. Thus, the sampling time of 15 min under the given conditions should be enough to accumulate sufficient particles down to the size of 100 nm.

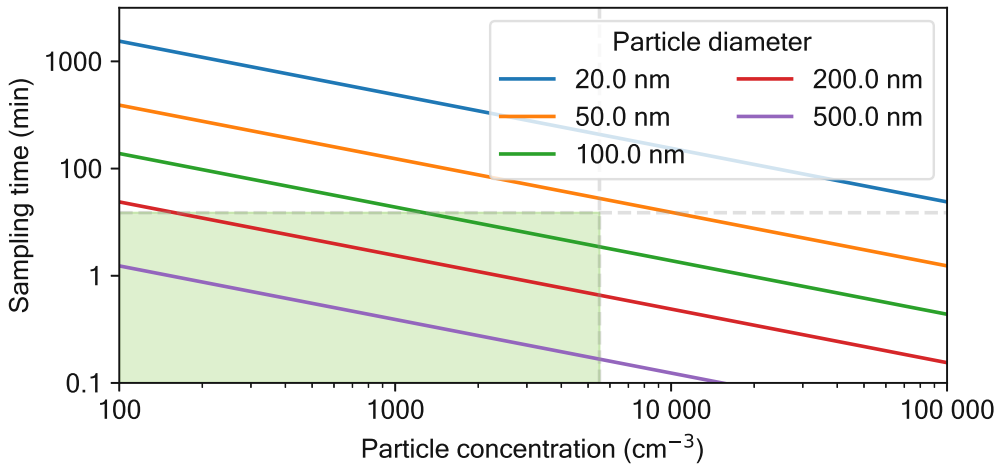

Fig. 7.12: Estimated sampling time on a resonator as a function of the ambient particle concentration and a set flow rate of 1 L min^{-1}. The green-shaded box highlights the expected particle capturing for a sampling time of 15 min and average particle concentration of 5500 cm^{-3} measured on the university rooftop.

Results & discussion. Figure 7.13 shows the average response from three sampling runs performed within one day during the morning, midday, and evening at the rooftop in Vienna. Across all samples, a similar spectrum was obtained for the sampled environmental aerosol. Comparing the spectra to previous studies on urban aerosols analyzed by classical FTIR spectroscopy [176] and AFM-IR spectroscopy [177], the major vibrational modes can be attributed to organic and inorganic-based aerosols, in particular aromatic CH 3040 cm^{-1}, aliphatic CH 2900 cm^{-1}, carbonyl 1712 cm^{-1}, NH^{4+} 1417 cm^{-1} & 3190 cm^{-1}, NH^{2} 1600 cm^{-1} and SO_4^{2-} 1101 cm^{-1}. Moreover, one can observe a change of the spectral features in the fingerprint region between, in particular, 1300 cm^{-1} to 1000 cm^{-1} for different times of the day. The bulk chemical analysis with such a time resolution is not possible with the current state-of-the-art techniques that rely on filter sampling for a minimum of 6 h.

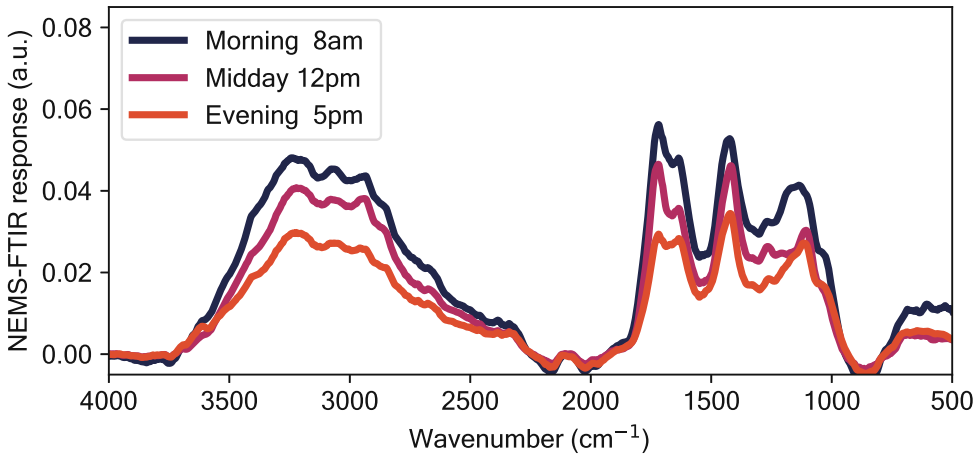

Fig. 7.13: Average NEMS-FTIR spectra of each 3 membrane resonators sampled for 15 min during morning, midday and evening on the rooftop. The spectra show consistent vibrational modes that can be attributed to organic and inorganic-based aerosols, in particular SO_4^{2-} 1101 cm^{-1}, NH^{4+} 1417 cm^{-1} & 3190 cm^{-1}, NH^{2} 1600 cm^{-1}, carbonyl 1712 cm^{-1}, aliphatic CH 2900 cm^{-1}, and aromatic CH 3040 cm^{-1} [176, 177].

To obtain a more detailed insight into the chemical composition, the NEMS-FTIR spectra can be further fitted with the open-source database for aerosols developed by Reggente et al. *AIRspec* [178]. In Figure 7.14, for example, this has been applied to a spectrum of aerosol sampled during the morning on the rooftop in Vienna (urban environment). The result shows that the spectrum can be well fitted assuming the presence of the aforementioned spectral features. From the visual comparison of our aerosol samples with the database, the very high NH2 (light orange around 1600 cm^{-1}) and carbonyl CO peak (dark green around 1700 cm^{-1}) levels show results comparable to other spectra

of samples collected from urban sites [178]. In addition, more carboxylic COH (light green bimodal line in the region between 3500 cm^{-1} to 2300 cm^{-1}) and especially greater abundance of alkane CH bonds (dark blue line around 2900 cm^{-1}) are characterized by urban samples [176, 177].

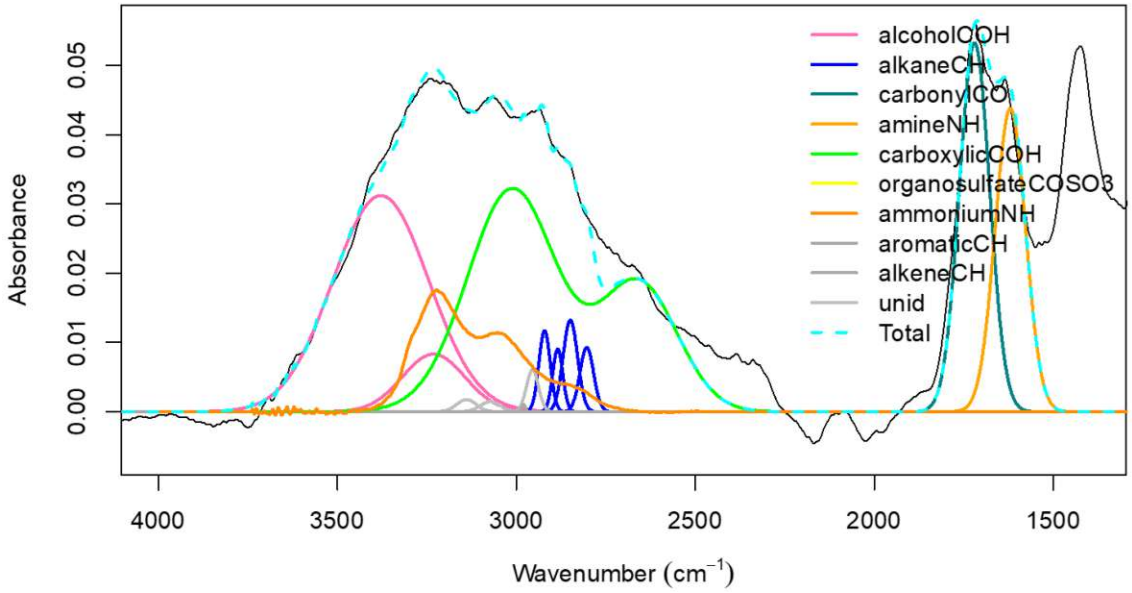

Fig. 7.14: Application example of the AIRspec database [178] on the spectrum of an aerosol sampled chip during the morning. The fit, exported from AIRspec, shows in general a good agreement with spectral features attributed to aerosol from an urban environment.

Conclusion. The study has demonstrated the rapid sampling and analysis of ultrafine airborne particles utilizing NEMS-FTIR spectroscopy. While previous urban aerosol spectra for comparison [176] were generated from several hours of sampling airborne particles onto a filter, this proof-of-concept analysis involved only a 15 min sampling duration using a simplified sampling system. This highlights the immense potential of NEMS-FTIR spectroscopy to assess bulk chemical composition within a significantly shorter time frame, offering promising implications for expedited analysis in environmental monitoring and related fields.

8 Summary & outlook

In the course of this work, the technique of applied NEMS-IR spectroscopy was fundamentally studied. Thereby, several aspects of the technique affecting the applicability and sensitivity were investigated.

Resonator geometry. In terms of sensitivity, the impact of resonator geometry on heat transfer mechanisms presents a trade-off between thermal isolation and sensing area. Minimizing thermal conductance, achieved by opting for a trampoline resonator over a membrane resonator, enhances power responsivity. However, this holds true only for resonator sizes not dominated by radiative heat transfer. Notably, the central area will encounter this limitation sooner in a more thermally isolated geometry like a trampoline compared to a membrane. Consequently, the optimal resonator design depends on the specific application.
For instance, in the case of indirect NAM-IR spectroscopy in the FIR/THz region ($\lambda > 20\,\mu m$), where a larger detection area is imperative, a membrane resonator proves advantageous. This consideration, however, implies the utilization of a metal film as the absorber and may change if a different absorption method is used.
Conversely, for direct NAM-IR spectroscopy, such as analyzing single particles, a trampoline resonator featuring a small central area offers improved sensitivity. These considerations evolve further when incorporating a broad spectral absorber or accounting for sampling efficiency.
Regarding robustness, implementing a round clamping design for trampoline-shaped resonators notably enhances fabrication yield.

Tensile stress. Aside from geometry, the tensile stress of the resonator material impacts various sensitivity-related parameters. Generally, both fractional frequency noise and transduction noise benefit from higher tensile stress. However, this advantage is accompanied by a reduced power responsivity. In practical terms, the theoretically predicted frequency resolution of highly tensile-stressed resonators is unattainable, making lower stress preferable for achieving high sensitivity.
In summarizing the findings of this study, a tensile stress of 100 MPa seems to offer a good balance. Further reduction of tensile stress through oxygen plasma treatments (see [52]) did not yield a significant sensitivity improvement. The optimal balance between these factors, particularly for higher tensile stress levels, remains subject to ongoing investigation.

Sampling methods. The ideal sampling approach for direct NAM-IR spectroscopy varies depending on the application. Regarding aerosol-based sampling, the resonator geometry strongly affects the sampling efficiency. As for the sensitivity, the geometry represents a trade-off between high sensitivity and sampling efficiency. From the study conducted in Section 5.2.2, one can conclude that the higher sampling efficiency of a perforated membrane compensates for its reduced power responsivity. In this context, a perforation pattern with a diameter of 6 µm and 9 µm pitch showed the best efficiency.

When dealing with soluble analytes of low concentrations, aerosol sampling efficiency can be enhanced by introducing an IR-inactive compound into the solution. This augmentation increases particle size, thereby enhancing impaction efficiency. Presently, a focused investigation is underway, exploring the effects of adding sodium chloride to an Indomethacin solution.

Apart from the resonator geometry, aerosol generation plays a crucial role in the sampling efficiency. An optimal sampling system should provide large droplets with a high transport efficiency. However, the droplet size should not exceed a volume that can be dried to a particulate aerosol.

Spin-casting can be a viable sampling alternative for analyzing thin-films or single particles. This was demonstrated in Section 7.4 for a 17 nm polystyrene thin-film. Alternatively, the sample can be drop-casted as demonstrated in Section 7.1 for the NEMS-IR spectroscopy of the protein BSA. To avoid the formation of a 'coffee ring' or loading by salt, a suited surface functionalization should be applied. This would enable the full submersion of a resonator in a solution to bind a target substance specifically.

Transduction and frequency tracking. Implementing an electrodynamic transduction scheme facilitated the fast and simple analysis of resonators. Considering the relatively small impact of the electrodes on theoretical sensitivity (see Section 2.3), this transduction presents a well-suited method for applied NEMS-IR spectroscopy. Furthermore, the impact can be reduced by increasing the tensile stress.

Alternatively, one can reduce transduction noise by implementing a contactless readout of the resonance frequency based on optical interferometry. However, if the resonator features an absorber, the intensity noise of a readout laser translates to additional fractional frequency noise. This challenge could be addressed by a tailored absorber design, which is currently being tested as part of an ongoing PhD project.

This work investigated different frequency tracking schemes. Compared to the commonly used PLL, the SSO scheme, in combination with a frequency counter, showed a more robust and faster response to frequency changes without compromising the

frequency resolution. Thus, the SSO scheme should be employed for the application of NEMS-IR spectroscopy.

Absorptance and heat transfer. A highly efficient absorber was developed and characterized as part of this work. Due to the principle of impedance-matched absorption, the gained absorptance is linear over the entire MIR range. Recent experiments of NAM-IR detection with a similar impedance-matched absorber made of platinum indicate, that this is valid also in the THz range. However, the addition of a metallic layer increases the thermal conductance, which reduces the power responsivity. Additionally, the increased absorptance is accompanied by increased emissivity.
Thus, to fully gain from the increased absorptance, the resonator size and absorber size should be kept below the regime dominated by radiation. Due to the high thermal conductivity of metals (gold $\kappa \approx 320\,\mathrm{W/(mK)}$), this transition point is slightly shifted to a larger resonator size. For applying indirect NAM-IR spectroscopy, the size of the absorber should be reduced to the maximum IR wavelength to be detected. In collaboration with M. Piller, the implementation of an impedance-matched thin film to a trampoline-shaped resonator enabled a sensitivity of $7\,\mathrm{pW}/\sqrt{\mathrm{Hz}}$, approaching the theoretical limit of photothermal detection at room temperature [6].

NEMS-IR-TD. Incorporating a thermo-electric element to the setup enabled the *in situ* desorption, adsorption, and separation of chemical compounds. For the first time, thermal desorption and thermo-gravimetrical analysis were combined with NEMS-IR spectroscopy to form a novel technique called NEMS-IR-TD. Application of this method to both single and mixed compounds allows for precise characterization of detection limits. With the enhanced NEMS-IR-TD setup featuring a QCL light source, an empirical detection limit of 5 pg for caffeine and theobromine was obtained.
Beyond spectral analysis, temperature control enables the characterization of desorption kinetics and extraction of desorption enthalpies on a picogram scale. This capability was validated for caffeine and theobromine through temperature-programmed desorption experiments with varying mass loads, yielding enthalpies consistent with literature values. This capability empowers NEMS-IR-TD to investigate catalysis, trigger chemical reactions, and monitor mass and chemical composition simultaneously within a single measurement. However, determining the technique's resolution regarding vapor pressure surpassed the time and scope of this study.

NEMS-FTIR spectroscopy. In this study, the developed setup for NEMS-IR spectroscopy was successfully integrated into a commercial FTIR system. This integration allowed for the NEMS-FTIR spectroscopy of a diverse range of analytes, from standard compounds like caffeine to complex environmental samples like ultrafine particles. Compared to prior NAM-IR investigations reliant on a QCL light source, this integration significantly broadened the accessible spectral range to the entire MIR region. The characterization of the system with theobromine showed a detection limit of 130 pg. The decreased sensitivity compared to the QCL-based setup can be attributed to the significantly reduced light intensity of the FTIR light source. However, compared to conventional transmission FTIR spectroscopy, where often several milligrams of analyte are needed, this represents an improvement of sensitivity on the order of 10^6.

At the time of this work, the commercial FTIR lacked the necessary light source and optics to assess the performance of NEMS-FTIR spectroscopy in the FIR and THz regions. However, given the wavelength-independent sensitivity and reduced modulation frequency in these regions, one can anticipate the same performance to that demonstrated in the MIR range.

Comparison of NEMS-IR spectroscopy to state-of-the-art. For putting the developed system in perspective, one can compare the sensitivity to other cutting-edge photothermal techniques, such as AFM-IR. Recent studies employing advanced AFM-IR spectroscopy have showcased remarkable sensitivities in discerning liposomes loaded with cytarabine (Wieland et al., 2019). This technique, also known as photothermal induced resonance (PTIR), achieved the detection of approximately 10^3 molecules (equivalent to 1.7 zmol). Notably, this sensitivity stands several orders of magnitude lower than the NEMS-IR detection limit of 5 pg (~30 fmol of caffeine) attained in this work.

In comparison to NEMS-IR spectroscopy, PTIR benefits from the high lateral resolution of an AFM in the sub-nanometer range. This enables the localized detection of the analyte's photothermal expansion directly by the AFM tip. In this approach, the probing light, typically from a QCL, can be focused down to the tip only, thereby increasing the power density. These conditions significantly enhance sensitivity but also confine PTIR to localized analysis of single particles.

In contrast, in NEMS-IR spectroscopy, the photothermal expansion of the entire resonator is measured. However, recent studies have shown that NAM-IR detection with a probing laser allows for photothermal imaging of single molecules [60]. Similar to the aforementioned considerations regarding geometry, transduction scheme, and sampling method, the sensitivity depends on the targeted application and can be improved.

Hence, for a fair comparison of the techniques, evaluating the detection limit for the same analyte per area and impinging power density would be essential, though beyond the scope of this work.

The primary objective of this study was the development of a widely applicable analytical tool for fast chemical analysis of low-abundance analytes. As for the example of environmental aerosols, PTIR analysis of a single filter paper may require up to 9 hours to identify all individual particles. In contrast, the spectral analysis and total mass by NEMS-FTIR spectroscopy can be obtained within a few minutes.

Closing remarks. The developed NEMS-IR and NEMS-FTIR system demonstrated the capability to provide fast analysis of nanomaterials, thin-films and analytes with sensitivities in the single picogram range. Individual studies conducted during this thesis comprised the fabrication of a suitable absorber, exploring resonator geometries and sampling methods, and frequency tracking schemes. The results of the studies are intended to provide guidelines for tailoring the sensitivity of NAM-IR spectroscopy, depending on the desired application. The combination of NEMS-IR (and NEMS-FTIR) spectroscopy with thermogravimetric analysis further enriches the versatility and potential applications of the technique across different research areas.

Bibliography

[1] M. Piller, N. Luhmann, M.-H. Chien, and S. Schmid, "Nanoelectromechanical infrared detector," in *Optical Sensing, Imaging, and Photon Counting: From X-Rays to THz 2019* (O. Mitrofanov, ed.), vol. 11088, (Vienna), pp. 1–7, International Society for Optics and Photonics, SPIE, 2019.

[2] N. Luhmann, D. Høj, M. Piller, H. Kähler, M.-H. Chien, R. G. West, U. L. Andersen, and S. Schmid, "Ultrathin 2 nm gold as ideal impedance-matched absorber for infrared light," *Nature Communications*, no. 2020, pp. 1–7, 2019.

[3] M. Piller, P. Sadeghi, R. G. West, N. Luhmann, P. Martini, O. Hansen, and S. Schmid, "Thermal radiation dominated heat transfer in nanomechanical silicon nitride drum resonators," *Applied Physics Letters*, vol. 117, no. 3, 2020.

[4] P. Sadeghi, M. Tanzer, N. Luhmann, M. Piller, M. H. Chien, and S. Schmid, "Thermal Transport and Frequency Response of Localized Modes on Low-Stress Nanomechanical Silicon Nitride Drums Featuring a Phononic-Band-Gap Structure," *Physical Review Applied*, vol. 14, no. 2, p. 1, 2020.

[5] M. G. Bartmann, M. Sistani, N. Luhmann, S. Schmid, E. Bertagnolli, A. Lugstein, and J. Smoliner, "Germanium nanowire microbolometer," *Nanotechnology*, vol. 33, 6 2022.

[6] M. Piller, J. Hiesberger, E. Wistrela, P. Martini, N. Luhmann, and S. Schmid, "Thermal IR Detection With Nanoelectromechanical Silicon Nitride Trampoline Resonators," *IEEE Sensors Journal*, vol. 23, pp. 1066–1071, 1 2023.

[7] N. Luhmann, R. G. West, J. P. Lafleur, and S. Schmid, "Nanoelectromechanical Infrared Spectroscopy with In Situ Separation by Thermal Desorption: NEMS-IR-TD," *ACS Sensors*, vol. 8, pp. 1462–1470, 4 2023.

[8] H. Bešić, A. Demir, J. Steurer, N. Luhmann, and S. Schmid, "Schemes for Tracking Resonance Frequency for Micro- and Nanomechanical Resonators," *Physical Review Applied*, vol. 20, p. 024023, 8 2023.

[9] P.B. Fellgett, *The theory of infra-red sensitivities and its application to investigations of steller radiations in the ear infra-red.* PhD thesis, University of Cambridge, 1951.

[10] J. W. Cooley and J. W. Tukey, "An Algorithm for the Machine Calculation of Complex Fourier Series," *Mathematics of Computation*, vol. 19, no. 90, p. 297, 1965.

[11] N. J. Harrick, "Study of Physics and Chemistry of Surfaces from Frustrated Total Internal Reflections," *Physical Review Letters*, vol. 4, pp. 224–226, 3 1960.

[12] A. Dazzi, R. Prazeres, F. Glotin, and J. M. Ortega, "Local infrared microspectroscopy with subwavelength spatial resolution with an atomic force microscope tip used as a photothermal sensor," *Optics Letters*, vol. 30, p. 2388, 9 2005.

[13] R. C. C. Leite, R. S. Moore, and J. R. Whinnery, "LOW ABSORPTION MEASUREMENTS BY MEANS OF THE THERMAL LENS EFFECT USING AN He–Ne LASER," *Applied Physics Letters*, vol. 5, pp. 141–143, 10 1964.

[14] F. Lu, M. Jin, and M. A. Belkin, "Tip-enhanced infrared nanospectroscopy via molecular expansion force detection," *Nature Photonics*, vol. 8, pp. 307–312, 4 2014.

[15] K. Wieland, G. Ramer, V. U. Weiss, G. Allmaier, B. Lendl, and A. Centrone, "Nanoscale chemical imaging of individual chemotherapeutic cytarabine-loaded liposomal nanocarriers," *Nano Research*, vol. 12, pp. 197–203, 1 2019.

[16] G. Gachot, S. Grugeon, I. Jimenez-Gordon, G. G. Eshetu, S. Boyanov, A. Lecocq, G. Marlair, S. Pilard, and S. Laruelle, "Gas chromatography/Fourier transform infrared/mass spectrometry coupling: A tool for Li-ion battery safety field investigation," *Analytical Methods*, vol. 6, pp. 6120–6124, 8 2014.

[17] M. J. Low and S. K. Freeman, "Measurement of Infrared Spectra of Gas-Liquid Chromatography Fractions Using Multiple-Scan Interference Spectrometry," *Analytical Chemistry*, vol. 39, pp. 194–198, 2 1967.

[18] P. R. Griffiths, D. A. Heaps, and P. a. R. Brejna, "The Gas Chromatography/Infrared Interface: Past, Present, and Future," *Applied Spectroscopy*, vol. 62, pp. 259A–270A, 10 2008.

[19] J. Kuligowski, G. Quintás, M. La Guardia, and B. Lendl, "Liquid chromatography — Fourier transform infrared spectroscopy," in *Encyclopedia of Analytical Science*, pp. 75–85, Elsevier, 1 2019.

[20] I. Ojanperä, K. Pihlainen, and E. Vuori, "Identification Limits for Volatile Organic Compounds in the Blood by Purge-and-Trap GC-FTIR," *Journal of Analytical Toxicology*, vol. 22, pp. 290–295, 7 1998.

[21] A. Lanzarotta, T. Falconer, H. McCauley, L. Lorenz, D. Albright, J. Crowe, and J. Batson, "Simultaneous Orthogonal Drug Detection Using Fully Integrated Gas Chromatography with Fourier Transform Infrared Detection and Mass Spectrometric Detection," *Applied Spectroscopy*, vol. 71, pp. 1050–1059, 5 2017.

[22] T. M. Salerno, P. Donato, G. Frison, L. Zamengo, and L. Mondello, "Gas Chromatography—Fourier Transform Infrared Spectroscopy for Unambiguous Determination of Illicit Drugs: A Proof of Concept," *Frontiers in Chemistry*, vol. 8, p. 624, 7 2020.

[23] J. S. Zavahir, J. S. Smith, S. Blundell, H. D. Waktola, Y. Nolvachai, B. R. Wood, and P. J. Marriott, "Relationships in Gas Chromatography—Fourier Transform Infrared Spectroscopy—Comprehensive and Multilinear Analysis," *Separations 2020, Vol. 7, Page 27*, vol. 7, p. 27, 5 2020.

[24] L. Andrews, "IR and Raman Spectroscopies, Matrix Isolation Studies," in *Encyclopedia of Spectroscopy and Spectrometry*, pp. 359–364, Elsevier, 1 2017.

[25] C. Schlawis and S. Schulz, "Direct deposition GC/IR techniques in natural product identification," 2020.

[26] C. Klawun, T. A. Sasaki, C. L. Wilkins, D. Carter, G. Dent, P. Jackson, and J. Chalmers, "Improved Chromatographic Resolution for Gas Chromatography/Matrix Isolation Infrared Spectroscopy," *Appl. Spectrosc.*, vol. 47, pp. 957–964, 7 1993.

[27] P. Jackson, G. Dent, D. Carter, D. J. Schofield, J. M. Chalmers, T. Visser, and M. Vredenbregt, "Investigation of high sensitivity GC-FTIR as an analytical tool for structural identification," *Journal of High Resolution Chromatography*, vol. 16, pp. 515–521, 9 1993.

[28] S. Schroeder, M. G. A. P. Chem, and U. 2002, "Temperature-programmed desorption (TPD) thermal desorption spectroscopy (TDS)," *Adv. Phys. Chem. Lab, FU Berlin*, 2002.

[29] A. Benhammada and D. Trache, "Thermal decomposition of energetic materials using TG-FTIR and TG-MS: a state-of-the-art review," *Applied Spectroscopy Reviews*, vol. 55, pp. 724–777, 9 2020.

[30] L. Davydenko, B. Mischanchuk, V. Pokrovskiy, I. Babich, and Y. Plyuto, "TPD-MS and IR Studies of Cr(acac)3 Binding Upon CVD at Silica and Alumina Surfaces," *Chemical Vapor Deposition*, vol. 17, pp. 123–127, 6 2011.

[31] T. Makino, M. Okada, and A. Kokalj, "Adsorption of C 2 H 4 on Stepped Cu(410) Surface: A Combined TPD, FTIR, and DFT Study," *ACS Publications*, vol. 118, pp. 27436–27448, 11 2014.

[32] C. M. Ghimbeu, R. Gadiou, J. Dentzer, L. Vidal, and C. Vix-Guterl, "A TPD-MS study of the adsorption of ethanol/cyclohexane mixture on activated carbons," *Adsorption*, vol. 17, pp. 227–233, 2 2011.

[33] R. A. Ketola, J. T. Kiuru, V. Tarkiainen, J. T. Kokkonen, J. Räsänen, and T. Kotiaho, "Detection of volatile organic compounds by temperature-programmed desorption combined with mass spectrometry and Fourier transform infrared spectroscopy," *Analytica Chimica Acta*, vol. 562, pp. 245–251, 3 2006.

[34] Y. Liu, R. Li, J. Yu, F. Ni, Y. Sheng, A. Scircle, J. V. Cizdziel, and Y. Zhou, "Separation and identification of microplastics in marine organisms by TGA-FTIR-GC/MS: A case study of mussels from coastal China," *Environmental Pollution*, vol. 272, p. 115946, 3 2021.

[35] A. N. Cleland, *Foundations of nanomechanics: from solid-state theory to device applications*. Springer Science \& Business Media, 2013.

[36] J. Tamayo, P. M. Kosaka, J. J. Ruz, Á. S. Paulo, and M. Calleja, "Biosensors based on nanomechanical systems," *Chemical Society Reviews*, vol. 42, pp. 1287–1311, 1 2013.

[37] K. Eom, H. S. Park, D. S. Yoon, T. Kwon, and G. E. W. Bauer, "Nanomechanical resonators and their applications in biological/chemical detection: Nanomechanics principles," *Physics Reports*, vol. 503, pp. 115–163, 2011.

[38] J. Chaste, A. Eichler, J. Moser, G. Ceballos, R. Rurali, and A. Bachtold, "A nanomechanical mass sensor with yoctogram resolution," *Nature Nanotechnology 2012 7:5*, vol. 7, pp. 301–304, 4 2012.

[39] M. S. Hanay, S. Kelber, A. K. Naik, D. Chi, S. Hentz, E. C. Bullard, E. Colinet, L. Duraffourg, and M. L. Roukes, "Single-protein nanomechanical mass spectrometry in real time," *Nature Nanotechnology*, vol. 7, no. 9, pp. 602–608, 2012.

[40] M. S. Hanay, S. I. Kelber, C. D. O'Connell, P. Mulvaney, J. E. Sader, and M. L. Roukes, "Inertial imaging with nanomechanical systems," *Nature Nanotechnology 2015 10:4*, vol. 10, pp. 339–344, 3 2015.

[41] J. E. Sader, M. S. Hanay, A. P. Neumann, and M. L. Roukes, "Mass Spectrometry Using Nanomechanical Systems: Beyond the Point-Mass Approximation," *Nano Letters*, vol. 18, pp. 1608–1614, 3 2018.

[42] J. R. Barnes, R. J. Stephenson, C. N. Woodburn, S. J. O'Shea, M. E. Welland, T. Rayment, J. K. Gimzewski, and C. Gerber, "A femtojoule calorimeter using micromechanical sensors," *Review of Scientific Instruments*, vol. 65, pp. 3793–3798, 12 1994.

[43] M. Li, A. Matyushov, C. Dong, H. Chen, H. Lin, T. Nan, Z. Qian, M. Rinaldi, Y. Lin, and N. X. Sun, "Ultra-sensitive NEMS magnetoelectric sensor for picotesla DC magnetic field detection," *Applied Physics Letters*, vol. 110, p. 143510, 4 2017.

[44] Y. Hui and M. Rinaldi, "High performance NEMS resonant infrared detector based on an aluminum nitride nano-plate resonator," *2013 Transducers and Eurosensors XXVII: The 17th International Conference on Solid-State Sensors, Actuators and Microsystems, TRANSDUCERS and EUROSENSORS 2013*, pp. 968–971, 2013.

[45] X. C. Zhang, E. B. Myers, J. E. Sader, and M. L. Roukes, "Nanomechanical torsional resonators for frequency-shift infrared thermal sensing," *Nano Letters*, vol. 13, no. 4, pp. 1528–1534, 2013.

[46] L. Duraffourg, L. Laurent, J. S. Moulet, J. Arcamone, and J. J. Yon, "Array of resonant electromechanical nanosystems: A technological breakthrough for uncooled infrared imaging," *Micromachines*, vol. 9, no. 8, 2018.

[47] H. H. Cary, "Infrared radiation detector employing tensioned foil to receive radiation," *United States Patent Office*, pp. 250–83, 7 1969.

[48] J. Varesi, J. Lai, T. Perazzo, Z. Shi, and A. Majumdar, "Photothermal measurements at picowatt resolution using uncooled micro-optomechanical sensors," *Applied Physics Letters*, vol. 71, pp. 306–308, 7 1997.

[49] J. Lai, T. Perazzo, Z. Shi, and A. Majumdar, "Optimization and performance of high-resolution micro-optomechanical thermal sensors," *Sensors and Actuators A: Physical*, vol. 58, pp. 113–119, 2 1997.

[50] G. Li, L. W. Burggraf, and W. P. Baker, "Photothermal spectroscopy using multilayer cantilever for chemical detection," *Applied Physics Letters*, vol. 76, pp. 1122–1124, 2 2000.

[51] S. Kim, D. Lee, X. Liu, C. Van Neste, S. Jeon, and T. Thundat, "Molecular recognition using receptor-free nanomechanical infrared spectroscopy based on a quantum cascade laser," *Scientific Reports*, vol. 3, p. 1111, 1 2013.

[52] N. Luhmann, A. Jachimowicz, J. Schalko, P. Sadeghi, M. Sauer, A. Foelske-Schmitz, and S. Schmid, "Effect of oxygen plasma on nanomechanical silicon nitride resonators," *Applied Physics Letters*, vol. 111, no. 6, 2017.

[53] T. S. Biswas, N. Miriyala, C. Doolin, X. Liu, T. Thundat, and J. P. Davis, "Femtogram-scale photothermal spectroscopy of explosive molecules on nanostrings," *Analytical Chemistry*, vol. 86, pp. 11368–11372, 11 2014.

[54] A. Blaikie, D. Miller, and B. J. Alemán, "A fast and sensitive room-temperature graphene nanomechanical bolometer," *Nature Communications 2019 10:1*, vol. 10, pp. 1–8, 10 2019.

[55] S. Yamada, S. Schmid, T. Larsen, O. Hansen, and A. Boisen, "Photothermal infrared spectroscopy of airborne samples with mechanical string resonators," *Analytical Chemistry*, vol. 85, no. 21, pp. 10531–10535, 2013.

[56] A. J. Andersen, S. Yamada, E. K. Pramodkumar, T. L. Andresen, A. Boisen, and S. Schmid, "Nanomechanical IR spectroscopy for fast analysis of liquid-dispersed engineered nanomaterials," *Sensors and Actuators, B: Chemical*, vol. 233, pp. 667–673, 2016.

[57] M. Kurek, M. Carnoy, P. E. Larsen, L. H. Nielsen, O. Hansen, T. Rades, S. Schmid, and A. Boisen, "Nanomechanical Infrared Spectroscopy with Vibrating Filters for Pharmaceutical Analysis," *Angewandte Chemie - International Edition*, vol. 56, no. 14, pp. 3901–3905, 2017.

[58] F. Samaeifar, A. Casci Ceccacci, S. Bose Goswami, L. Hagner Nielsen, A. Afifi, K. Zór, and A. Boisen, "Evaluation of the solid state form of tadalafil in sub-micron thin films using nanomechanical infrared spectroscopy," *International Journal of Pharmaceutics*, vol. 565, pp. 227–232, 6 2019.

[59] A. Casci Ceccacci, A. Cagliani, P. Marizza, S. Schmid, and A. Boisen, "Thin Film Analysis by Nanomechanical Infrared Spectroscopy," *ACS Omega*, vol. 4, pp. 7628–7635, 4 2019.

[60] M. H. Chien, M. Brameshuber, B. K. Rossboth, G. J. Schütz, and S. Schmid, "Single-molecule optical absorption imaging by nanomechanical photothermal sensing," *Proceedings of the National Academy of Sciences of the United States of America*, vol. 115, no. 44, pp. 11150–11155, 2018.

[61] R. G. West, K. Kanellopulos, and S. Schmid, "Photothermal Microscopy and Spectroscopy with Nanomechanical Resonators," *The Journal of Physical Chemistry C*, 11 2023.

[62] S. Schmid, L. G. Villanueva, and M. L. Roukes, *Fundamentals of Nanomechanical Resonators*, vol. 2. Cham: Springer International Publishing, 2023.

[63] J. R. Vig and Y. Kim, "Noise in microelectromechanical system resonators," *IEEE Transactions on Ultrasonics, Ferroelectrics, and Frequency Control*, vol. 46, no. 6, pp. 1558–1565, 1999.

[64] A. N. Cleland and M. L. Roukes, "Noise processes in nanomechanical resonators," *Journal of Applied Physics*, vol. 92, pp. 2758–2769, 9 2002.

[65] A. Demir, "Understanding fundamental trade-offs in nanomechanical resonant sensors," *Journal of Applied Physics*, vol. 129, p. 44503, 1 2021.

[66] J. Vlassak and W. Nix, "A new bulge test technique for the determination of young's modulus and poisson's ratio of thin films," *Journal of Materials Research*, vol. 7, no. 12, p. 3242–3249, 1992.

[67] T. Larsen, S. Schmid, L. Grönberg, A. O. Niskanen, J. Hassel, S. Dohn, and A. Boisen, "Ultrasensitive string-based temperature sensors," *Applied Physics Letters*, vol. 98, p. 121901, 3 2011.

[68] H. F. et al., "Thermal conductivity of silicon nitride membranes is not sensitive to stress," *Phys. Rev. B*, vol. 92, p. 125439, Sep 2015.

[69] A. K. Naik, M. S. Hanay, W. K. Hiebert, X. L. Feng, and M. L. Roukes, "Towards single-molecule nanomechanical mass spectrometry," *Nature Nanotechnology*, vol. 4, no. 7, pp. 445–450, 2009.

[70] B. Lassagne, D. Garcia-Sanchez, A. Aguasca, and A. Bachtold, "Ultrasensitive mass sensing with a nanotube electromechanical resonator," *Nano Letters*, vol. 8, pp. 3735–3738, 11 2008.

[71] Y. T. Yang, C. Callegari, X. L. Feng, K. L. Ekinci, and M. L. Roukes, "Zeptogram-scale nanomechanical mass sensing," *Nano Letters*, vol. 6, pp. 583–586, 4 2006.

[72] H. Nyquist, "Thermal agitation of electric charge in conductors," *Physical Review*, vol. 32, no. 1, pp. 110–113, 1928.

[73] H. B. Callen and T. A. Welton, "Irreversibility and generalized noise," *Physical Review*, vol. 83, no. 1, pp. 34–40, 1951.

[74] J. B. Johnson, "Thermal Agitation of Electricity in Conductors," *Nature 1927 119:2984*, vol. 119, no. 2984, pp. 50–51, 1927.

[75] M. H. Chien, J. Steurer, P. Sadeghi, N. Cazier, and S. Schmid, "Nanoelectromechanical Position-Sensitive Detector with Picometer Resolution," *ACS Photonics*, vol. 7, pp. 2197–2203, 8 2020.

[76] S. Schmid, M. Kurek, J. Q. Adolphsen, and A. Boisen, "Real-time single airborne nanoparticle detection with nanomechanical resonant filter-fiber," *Scientific Reports*, vol. 3, p. 1288, 2 2013.

[77] Q. L. Nguyen, P. E. Larsen, S. Bishnoi, A. Boisen, and S. S. Keller, "Nanomechanical Infrared Spectroscopy with completely free-standing pyrolytic carbon string resonators for paracetamol detection," 2018.

[78] H. C. Yeh and B. Y. Liu, "Aerosol filtration by fibrous filters—I. theoretical," *Journal of Aerosol Science*, vol. 5, pp. 191–204, 3 1974.

[79] W. C. Hinds, "Aerosol technology: properties, behaviour, and measurement of airborne particles.," *Wiley*, vol. 2, pp. 190–205, 1999.

[80] R. Raiteri, M. Grattarola, H. J. Butt, and P. Skládal, "Micromechanical cantilever-based biosensors," *Sensors and Actuators B: Chemical*, vol. 79, pp. 115–126, 10 2001.

[81] M. Bagheri, I. Chae, D. Lee, S. Kim, and T. Thundat, "Selective detection of physisorbed hydrocarbons using photothermal cantilever deflection spectroscopy," *Sensors and Actuators B: Chemical*, vol. 191, pp. 765–769, 2 2014.

[82] K. Kanellopulos, R. G. West, and S. Schmid, "Nanomechanical Photothermal Near Infrared Spectromicroscopy of Individual Nanorods," *ACS Photonics*, vol. 10, pp. 3730–3739, 10 2023.

[83] A. Demir and M. S. Hanay, "Fundamental Sensitivity Limitations of Nanomechanical Resonant Sensors due to Thermomechanical Noise," *IEEE Sensors Journal*, pp. 1–1, 2019.

[84] B. Lendl, "Infrared and Raman Spectroscopy," in *Analytical Chemistry. A Modern Approach to Analytical Science* (R. Kellner and J.-M. Mermet and M. Otto and M. Valcarcel and M. Widmer (Eds.), ed.), no. 11, pp. 750–779, Copyright Wiley-VCH GmbH, 2 ed., 2004.

[85] P. R. Griffiths and J. A. De Haseth, *Fourier transform infrared spectrometry*, vol. 10. WILEY, 2007.

[86] A. Rogalski, "Graphene-based materials in the infrared and terahertz detector families: a tutorial," *Advances in Optics and Photonics*, vol. 11, p. 314, jun 2019.

[87] Y. Hui, J. S. Gomez-Diaz, Z. Qian, A. Alù, and M. Rinaldi, "Plasmonic piezoelectric nanomechanical resonator for spectrally selective infrared sensing," *Nature Communications*, vol. 7, pp. 1–9, 2016.

[88] W. Ma, Y. Wen, and X. Yu, "Broadband metamaterial absorber at mid-infrared using multiplexed cross resonators," *Optics Express*, vol. 21, no. 25, p. 30724, 2013.

[89] J. Gou, Q. Niu, K. Liang, J. Wang, and Y. Jiang, "Frequency modulation and absorption improvement of THz micro-bolometer with micro-bridge structure by spiral-type antennas," *Nanoscale Research Letters*, vol. 13, mar 2018.

[90] S. Yin, J. Zhu, W. Xu, W. Jiang, J. Yuan, G. Yin, L. Xie, Y. Ying, and Y. Ma, "High-performance terahertz wave absorbers made of silicon-based metamaterials," *Applied Physics Letters*, vol. 107, no. 7, 2015.

[91] Y. Takagawa, S. Ogawa, and M. Kimata, "Detection wavelength control of uncooled infrared sensors using two-dimensional lattice plasmonic absorbers," *Sensors*, vol. 15, pp. 13660–13669, jun 2015.

[92] Y. Jin, J. Xu, S. He, H. Ma, Y. Cui, N. X. Fang, and K. H. Fung, "Ultrabroadband Light Absorption by a Sawtooth Anisotropic Metamaterial Slab," *Nano Letters*, vol. 12, no. 3, pp. 1443–1447, 2012.

[93] S. Liu, H. Chen, and T. J. Cui, "A broadband terahertz absorber using multi-layer stacked bars," *Applied Physics Letters*, vol. 106, no. 15, pp. 1–6, 2015.

[94] H. Yan, F. Xia, W. Zhu, M. Freitag, C. Dimitrakopoulos, A. A. Bol, G. Tulevski, and P. Avouris, "Infrared Spectroscopy of Wafer-Scale Graphene," *ACS Nano*, vol. 5, pp. 9854–9860, 12 2011.

[95] S. Zanotto, F. Bianco, V. Miseikis, D. Convertino, C. Coletti, and A. Tredicucci, "Coherent absorption of light by graphene and other optically conducting surfaces in realistic on-substrate configurations," *APL Photonics*, vol. 2, no. 1, 2017.

[96] E. Hagen and H. Rubens, "Die absorption ultravioletter, sichtbarer und ultraroter strahlen in dünnen metallschichten," *Annalen der Physik*, vol. 313, no. 6, pp. 432–454, 1902.

[97] E. Hagen and H. Rubens, "Über beziehungen des reflexions- und emissionsvermögens der metalle zu ihrem elektrischen leitvermögen," *Annalen der Physik*, vol. 316, no. 8, pp. 873–901, 1903.

[98] W. Woltersdorff, "Über die optischen konstanten dünner metallschichten im langwelligen ultrarot," *Zeitschrift für Physik*, vol. 91, pp. 230–252, mar 1934.

[99] L. N. Hadley and D. M. Dennison, "Reflection and transmission interference filters.," *Journal of the Optical Society of America*, vol. 37, no. 6, 1947.

[100] C. Hilsum, "Infrared Absorption of Thin Metal Films at Non-Normal Incidence," *Journal of the Optical Society of America*, vol. 45, no. 2, p. 135, 1955.

[101] P. W. Kruse, *Uncooled Thermal Imaging Arrays, Systems, and Applications*. SPIE, 7 2001.

[102] O. Ajakaiye, J. Grade, C. Shin, and T. Kenny, "Wafer-scale fabrication of infrared detectors based on tunneling displaceAjakaiye, O., Grade, J., Shin, C., & Kenny, T. (2007). Wafer-scale fabrication of infrared detectors based on tunneling displacement transducers. Sensors and Actuators A: Physical, 1," *Sensors and Actuators A: Physical*, vol. 134, pp. 575–581, 3 2007.

[103] S. Bauer, S. Bauer-Gogonea, W. Becker, R. Fettig, B. Ploss, W. Ruppel, and W. von Münch, "Thin metal films as absorbers for infrared sensors," *Sensors and Actuators: A. Physical*, vol. 37-38, no. C, pp. 497–501, 1993.

[104] W. Lang, K. Kühl, and H. Sandmaier, "Absorbing layers for thermal infrared detectors," *Sensors and Actuators: A. Physical*, vol. 34, no. 3, pp. 243–248, 1992.

[105] G. D. Mahan and D. T. F. Marple, "Infrared absorption of thin metal films: Pt on Si," *Applied Physics Letters*, vol. 42, pp. 219–221, 2 1983.

[106] S. K. V., M. ElKabbash, V. Caligiuri, R. Singh, A. D. Luca, and G. Strangi, "Perfect light absorption in thin and ultra-thin films and its applications," in *Progress in Optical Science and Photonics*, pp. 3–27, Springer Singapore, 2019.

[107] S. J. Kim, J. Park, M. Esfandyarpour, E. F. Pecora, P. G. Kik, and M. L. Brongersma, "Superabsorbing, artificial metal films constructed from semiconductor nanoantennas," *Nano Letters*, vol. 16, pp. 3801–3808, may 2016.

[108] L. Laurent, J. J. Yon, J. S. Moulet, M. Roukes, and L. Duraffourg, "12-μ m -Pitch Electromechanical Resonator for Thermal Sensing," *Physical Review Applied*, vol. 9, no. 2, pp. 1–11, 2018.

[109] E. R. Brown, W. D. Zhang, H. Chen, and G. T. Mearini, "THz behavior of indium-tin-oxide films on p-Si substrates," *Applied Physics Letters*, vol. 107, no. 9, 2015.

[110] M. Hövel, B. Gompf, and M. Dressel, "Dielectric properties of ultrathin metal films around the percolation threshold," *Physical Review B*, vol. 81, p. 035402, 1 2010.

[111] N. Formica, D. S. Ghosh, A. Carrilero, T. L. Chen, R. E. Simpson, and V. Pruneri, "Ultrastable and atomically smooth ultrathin silver films grown on a copper seed layer," *ACS Applied Materials & Interfaces*, vol. 5, pp. 3048–3053, apr 2013.

[112] R. A. Maniyara, D. Rodrigo, R. Yu, J. Canet-Ferrer, D. S. Ghosh, R. Yongsunthon, D. E. Baker, A. Rezikyan, F. J. García de Abajo, and V. Pruneri, "Tunable plasmons in ultrathin metal films," *Nature Photonics*, vol. 13, no. 5, pp. 328–333, 2019.

[113] E. Schmiedl, P. Wissmann, and H. U. Finzel, "The electrical resistivity of ultra-thin copper films," *Zeitschrift fur Naturforschung - Section A Journal of Physical Sciences*, vol. 63, no. 10-11, pp. 739–744, 2008.

[114] W. Wu, S. H. Brongersma, M. Van Hove, and K. Maex, "Influence of surface and grain-boundary scattering on the resistivity of copper in reduced dimensions," *Applied Physics Letters*, vol. 84, no. 15, pp. 2838–2840, 2004.

[115] J. R. Sambles, K. C. Elsom, and D. J. Jarvis, "The Electrical Resistivity of Gold Films," *Philosophical Transactions of the Royal Society A: Mathematical, Physical and Engineering Sciences*, vol. 304, pp. 365–396, 3 1982.

[116] H.-U. Wissmann, Peter; Finzel, *Electrical Resistivity of Thin Metal Films*, vol. 223. Heidelberg: Springer Verlag, 223 ed., 2007.

[117] H.-U. Finzel and P. Wißmann, "Monte-Carlo Calculations of the Electrical Resistance of Ultra-Thin Metal Films," *Zeitschrift für Naturforschung A*, vol. 40, pp. 161–163, 1 1985.

[118] J. C. Phillips, "Anomalous hopping exponents of ultrathin metal films," *Physical Review B*, vol. 64, p. 035411, 6 2001.

[119] W. M. Haynes, *CRC Handbook of Chemistry and Physics*. Boca Raton: CRC Press, 91 ed., 2010.

[120] R. Henriquez, R. Roco, S. Bravo, V. Del Campo, C. Gonzalez-Fuentes, S. Donoso, and P. Häberle, "Effect of a metallic surfactant on the electrical percolation of gold films," *Applied Surface Science*, vol. 489, pp. 403–408, 9 2019.

[121] A. Ioffe and A. Regel, "Non-crystalline, amorphous and liquid electronic semiconductors," *Prog. Semicond*, vol. 4, pp. 237–291, 1960.

[122] D. V. Gruznev, D. A. Olyanich, D. N. Chubenko, D. A. Tsukanov, E. A. Borisenko, L. V. Bondarenko, M. V. Ivanchenko, A. V. Zotov, and A. A. Saranin, "Growth of Au thin film on Cu-modified Si(1 1 1) surface," *Surface Science*, vol. 603, no. 24, pp. 3400–3403, 2009.

[123] Z. Korczak and T. Kwapiński, "Electrical conductance at initial stage in epitaxial growth of Pb, Ag, Au and In on modified Si(1 1 1) surface," *Surface Science*, vol. 601, no. 16, pp. 3324–3334, 2007.

[124] V. Drobny and L. Pulfrey, "Properties of reactively-sputtered copper oxide thin films," *Thin Solid Films*, vol. 61, pp. 89–98, jul 1979.

[125] E. Centurioni, "Generalized matrix method for calculation of internal light energy flux in mixed coherent and incoherent multilayers," *Applied Optics*, 2005.

[126] R. de L. Kronig, "On the Theory of Dispersion of X-Rays," *Journal of the Optical Society of America*, vol. 12, p. 547, 6 1926.

[127] B. Gompf, J. Beister, T. Brandt, J. Pflaum, and M. Dressel, "Nanometer-thick Au-films as antireflection coating for infrared light," *Optics Letters*, vol. 32, p. 1578, 6 2007.

[128] D. A. Tsukanov, L. V. Bondarenko, and E. A. Borisenko, "Stability of Electric Characteristics of Au Films on Si(111)5.55 × 5.55-Cu Surface Exposed to Oxygen," *Technical Physics Letters*, vol. 36, no. 10, pp. 875–877, 2010.

[129] P. H. Pham, W. Zhang, N. V. Quach, J. Li, W. Zhou, D. Scarmardo, E. R. Brown, and P. J. Burke, "Broadband impedance match to two-dimensional materials in the terahertz domain," *Nature Communications*, vol. 8, no. 1, pp. 1–8, 2017.

[130] K. Waltenberger, *Construction and Characterization of an Aerosol Sampling Setup for Nanomechanical Infrared Spectroscopy*. PhD thesis, TU Wien, Vienna, 11 2020.

[131] J. W. Novak and R. F. Browner, "Characterization of Droplet Sprays Produced by Pneumatic Nebulizers," *Analytical Chemistry*, vol. 52, pp. 792–796, 5 1980.

[132] D. Stadlmann, *Implementation of 'Cyto Spray Chamber' for environmental analytes.* PhD thesis, TU Wien, Vienna, 2023.

[133] K. Kahen, K. Jorabchi, C. Gray, A. M. A. chemistry, and u. 2004, "Spatial mapping of droplet velocity and size for direct and indirect nebulization in plasma spectrometry," *ACS Publications*, vol. 76, pp. 7194–7201, 12 2004.

[134] Chiara Leuschner, *Construction and characterisation of a mobile setup for sampling airborne nanoparticles.* PhD thesis, TU Wien, Vienna, 3 2023.

[135] Raphael Pliesnig, *Development of a graphical unit interface for automated NEMS-IR spectroscopy (in progress).* PhD thesis, Institute for Sensor and Actuator Systems, Vienna, 2024.

[136] L. Smirnov, N. Kulikova, and N. Platonova, "Infrared spectra of polyvinylalcohol," *Polymer Science U.S.S.R.*, vol. 9, pp. 2849–2856, 1 1967.

[137] W. D. Bowers, M. L. Parsons, R. E. Clement, G. A. Eiceman, and F. W. Karasek, "Trace impurities in solvents commonly used for gas chromatographic analysis of environment samples," *Journal of Chromatography A*, vol. 206, pp. 279–288, 2 1981.

[138] P. Jacobs, W. Dewé, A. Flament, M. Gibella, and A. Ceccato, "A new validation approach applied to the GC determination of impurities in organic solvents," *Journal of Pharmaceutical and Biomedical Analysis*, vol. 40, pp. 294–304, 2 2006.

[139] M. Yun, S. Kim, D. Lee, N. Jung, I. Chae, S. Jeon, and T. Thundat, "Photothermal cantilever deflection spectroscopy of a photosensitive polymer," *Applied Physics Letters*, vol. 100, 5 2012.

[140] C. Willert, *Characterization of resonator design for nanoelectromechanical infrared spectroscopy*. PhD thesis, TU Wien, Vienna, 3 2022.

[141] P. Sadeghi, M. Tanzer, S. L. Christensen, and S. Schmid, "Influence of clamp-widening on the quality factor of nanomechanical silicon nitride resonators," *Journal of Applied Physics*, vol. 126, p. 165108, 10 2019.

[142] D. Y. Kim, H. Park, Y. I. Park, and J. H. Lee, "Polyvinyl alcohol hydrogel-supported forward osmosis membranes with high performance and excellent pH stability," *Journal of Industrial and Engineering Chemistry*, vol. 99, pp. 246–255, 7 2021.

[143] P. S. Thomas, J. P. Guerbois, G. F. Russell, and B. J. Briscoe, "FTIR study of the thermal degradation of poly(vinyl alcohol)," *Journal of Thermal Analysis and Calorimetry*, vol. 64, no. 2, pp. 501–508, 2001.

[144] C. J. Manning, R. M. Dittmar, R. A. Palmer, and J. L. Chao, "Use of step-scan FT-IR to obtain the photoacoustic/photothermal response phase," *Infrared Physics*, vol. 33, pp. 53–62, 1 1992.

[145] P. Redhead, "Thermal desorption of gases," *vacuum*, vol. 12, no. 4, pp. 203–211, 1962.

[146] F. Ucun, A. Sağlam, and V. Güçlü, "Molecular structures and vibrational frequencies of xanthine and its methyl derivatives (caffeine and theobromine) by ab initio Hartree–Fock and density functional theory calculations," *Spectrochimica Acta Part A: Molecular and Biomolecular Spectroscopy*, vol. 67, pp. 342–349, 6 2007.

[147] H. D. Wanzenboeck, P. Roediger, G. Hochleitner, E. Bertagnolli, and W. Buehler, "Novel method for cleaning a vacuum chamber from hydrocarbon contamination," *Journal of Vacuum Science \& Technology A: Vacuum, Surfaces, and Films*, vol. 28, pp. 1413–1420, 11 2010.

[148] M. Héritier, R. Pachlatko, Y. Tao, J. M. Abendroth, C. L. Degen, and A. Eichler, "Spatial Correlation between Fluctuating and Static Fields over Metal and Dielectric Substrates," *Physical Review Letters*, vol. 127, p. 216101, 11 2021.

[149] T. Visser, "Ft-ir detection in gas chromatography," *TrAC Trends in Analytical Chemistry*, vol. 21, no. 9-10, pp. 627–636, 2002.

[150] J. Pavelec, J. Hulva, D. Halwidl, R. Bliem, O. Gamba, Z. Jakub, F. Brunbauer, M. Schmid, U. Diebold, and G. S. Parkinson, "A multi-technique study of CO2 adsorption on Fe3O4 magnetite," *Journal of Chemical Physics*, vol. 146, no. 1, 2017.

[151] S. A. Fitzgerald, K. Shinbrough, K. H. Rigdon, J. L. C. Rowsell, M. T. Kapelewski, S. H. Pang, K. V. Lawler, and P. M. Forster, "Temperature-programmed desorption for isotope separation in nanoporous materials," *The Journal of Physical Chemistry C*, vol. 122, no. 4, pp. 1995–2001, 2018.

[152] I. H. M. van Stokkum, D. S. Larsen, and R. van Grondelle, "Global and target analysis of time-resolved spectra.," *Biochimica et biophysica acta*, vol. 1657, pp. 82–104, jul 2004.

[153] L. J. G. W. van Wilderen, C. N. Lincoln, and J. J. van Thor, "Modelling multi-pulse population dynamics from ultrafast spectroscopy," *PLoS ONE*, vol. 6, no. 3, 2011.

[154] C. Müller, T. Pascher, A. Eriksson, P. Chabera, and J. Uhlig, "KiMoPack: A python Package for Kinetic Modeling of the Chemical Mechanism," *The Journal of Physical Chemistry A*, vol. 126, pp. 4087–4099, 6 2022.

[155] R. G. West, M. Fuciman, H. Staleva-Musto, V. Sebelik, D. Bina, M. Durchan, V. Kuznetsova, and T. Polívka, "Equilibration dependence of fucoxanthin S1 and ICT signatures on polarity, proticity, and temperature by multi-pulse femtosecond absorption spectroscopy," *The Journal of Physical Chemistry B*, p. acs.jpcb.8b04217, jul 2018.

[156] M. Szkop, B. Kliszcz, and A. A. Kasprzak, "A simple and reproducible protocol of glass surface silanization for TIRF microscopy imaging," *Analytical Biochemistry*, vol. 549, no. March, pp. 119–123, 2018.

[157] S. Schmid, L. G. Villanueva, and M. L. Roukes, *Fundamentals of nanomechanical resonators*, vol. 1. Springer, 2016.

[158] M. Polanyi and E. Wigner, "Über die Interferenz von Eigenschwingungen als Ursache von Energieschwankungen und chemischer Umsetzungen," *Zeitschrift für Physikalische Chemie*, vol. 139A, pp. 439–452, 12 1928.

[159] A. De Jong and J. Niemantsverdriet, "Thermal desorption analysis: Comparative test of ten commonly applied procedures," *Surface Science*, vol. 233, no. 3, pp. 355–365, 1990.

[160] A. Abdelaziz, D. H. Zaitsau, A. Buzyurov, A. A. Minakov, S. P. Verevkin, and C. Schick, "Fast scanning calorimetry: Sublimation thermodynamics of low volatile and thermally unstable compounds," *Thermochimica Acta*, vol. 676, pp. 249–262, 6 2019.

[161] K. Oura, V.G. Lifshits, A.A. Saranin, A.V. Zotov, and M. Katayama, "Surface Science: An Introduction," 2013.

[162] C. M. Ghimbeu, R. Gadiou, J. Dentzer, L. Vidal, and C. Vix-Guterl, "A tpd-ms study of the adsorption of ethanol/cyclohexane mixture on activated carbons," *Adsorption*, vol. 17, no. 1, pp. 227–233, 2011.

[163] T. Dickbreder, R. Bechstein, and A. Kühnle, "Crucial impact of exchange between layers on temperature programmed desorption," *Physical Chemistry Chemical Physics*, vol. 23, pp. 18314–18321, 9 2021.

[164] E. R. Henry, "The use of matrix methods in the modeling of spectroscopic data sets," *Biophysical Journal*, vol. 72, no. 2 I, pp. 652–673, 1997.

[165] R. W. Hendler and R. I. Shrager, "Deconvolutions based on singular value decomposition and the pseudoinverse: a guide for beginners," *Journal of Biochemical and Biophysical Methods*, vol. 28, no. 1, pp. 1–33, 1994.

[166] M. Molnar, K. P. Reardon, C. Osborne, and I. Milić, "Spectral deconvolution with deep learning: Removing the effects of spectral psf broadening," *Frontiers in Astronomy and Space Sciences*, vol. 7, 2020.

[167] D. An, L. Zhang, Z. Liu, J. Liu, and Y. Wei, "Advances in infrared spectroscopy and hyperspectral imaging combined with artificial intelligence for the detection of cereals quality," *Critical Reviews in Food Science and Nutrition*, vol. 0, no. 0, pp. 1–31, 2022. PMID: 35442834.

[168] M. S. Hanay, S. Kelber, A. Naik, D. Chi, S. Hentz, E. Bullard, E. Colinet, L. Duraffourg, and M. Roukes, "Single-protein nanomechanical mass spectrometry in real time," *Nature nanotechnology*, vol. 7, no. 9, pp. 602–608, 2012.

[169] M.-K. Oh, R. De, and S.-Y. Yim, "Highly sensitive voc gas sensor employing deep cooling of sers film," *Journal of Raman Spectroscopy*, vol. 49, no. 5, pp. 800–809, 2018.

[170] P. Kollenz, D. P. Herten, and T. Buckup, "Unravelling the Kinetic Model of Photochemical Reactions via Deep Learning," *Journal of Physical Chemistry B*, vol. 124, no. 29, pp. 6358–6368, 2020.

[171] A. Schwaighofer, C. K. Akhgar, and B. Lendl, "Broadband laser-based mid-IR spectroscopy for analysis of proteins and monitoring of enzyme activity," *Spectrochimica Acta - Part A: Molecular and Biomolecular Spectroscopy*, vol. 253, p. 119563, 2021.

[172] S. Luthra, D. S. Kalonia, and M. J. Pikal, "Effect of hydration on the secondary structure of lyophilized proteins as measured by fourier transform infrared (FTIR) spectroscopy," *Journal of Pharmaceutical Sciences*, vol. 96, pp. 2910–2921, 11 2007.

[173] A. Sachdeva and S. Cai, "Structural Differences of Proteins between Solution State and Solid State Probed by Attenuated Total Reflection Fourier Transform Infrared Spectroscopy," *Applied Spectroscopy*, vol. 63, pp. 458–464, 4 2009.

[174] Y. I. Tarasevich and L. I. Monakhova, "Interaction between globular proteins and silica surfaces," *Colloid Journal*, vol. 64, no. 4, pp. 482–487, 2002.

[175] I. Axelsson, "Characterization of proteins and other macromolecules by agarose gel chromatography," *Journal of Chromatography A*, vol. 152, pp. 21–32, 5 1978.

[176] S. Takahama, G. Ruggeri, and A. M. Dillner, "Analysis of functional groups in atmospheric aerosols by infrared spectroscopy: Sparse methods for statistical selection of relevant absorption bands," *Atmospheric Measurement Techniques*, vol. 9, pp. 3429–3454, 7 2016.

[177] A. L. Bondy, R. M. Kirpes, R. L. Merzel, K. A. Pratt, M. M. Banaszak Holl, and A. P. Ault, "Atomic Force Microscopy-Infrared Spectroscopy of Individual Atmospheric Aerosol Particles: Subdiffraction Limit Vibrational Spectroscopy and Morphological Analysis," *Analytical chemistry*, vol. 89, pp. 8594–8598, 9 2017.

[178] M. Reggente, R. Höhn, and S. Takahama, "An open platform for Aerosol InfraRed Spectroscopy analysis – AIRSpec," *Atmospheric Measurement Techniques*, vol. 12, pp. 2313–2329, 4 2019.

List of Figures

List of Tables